AD-A227 721

REPORT DOCUMENTATION PAGE

Form Approved
OMB No. 0704-0188

1. AGENCY USE ONLY (Leave blank)	2. REPORT DATE	3. REPORT TYPE AND DATES COVERED
	1990	Thesis/Dissertation

4. TITLE AND SUBTITLE
Derivation of Exospheric Temperature at High Latitudes from Incoherent-Scatter Radar Data

5. FUNDING NUMBERS

6. AUTHOR(S)
Willow Cliffswallow

7. PERFORMING ORGANIZATION NAME(S) AND ADDRESS(ES)
AFIT Student at: Utah State University

8. PERFORMING ORGANIZATION REPORT NUMBER
AFIT/CI/CIA - 90-110

9. SPONSORING/MONITORING AGENCY NAME(S) AND ADDRESS(ES)
AFIT/CI
Wright-Patterson AFB OH 45433

10. SPONSORING/MONITORING AGENCY REPORT NUMBER

11. SUPPLEMENTARY NOTES

12a. DISTRIBUTION/AVAILABILITY STATEMENT
Approved for Public Release IAW AFR 190-1
Distribution Unlimited
ERNEST A. HAYGOOD, 1st Lt, USAF
Executive Officer, Civilian Institution Programs

12b. DISTRIBUTION CODE

13. ABSTRACT (Maximum 200 words)

14. SUBJECT TERMS	15. NUMBER OF PAGES
	100
	16. PRICE CODE

17. SECURITY CLASSIFICATION OF REPORT	18. SECURITY CLASSIFICATION OF THIS PAGE	19. SECURITY CLASSIFICATION OF ABSTRACT	20. LIMITATION OF ABSTRACT
UNCLASSIFIED			

DERIVATION OF EXOSPHERIC TEMPERATURE AT HIGH LATITUDES FROM INCOHERENT-SCATTER RADAR DATA

by

Willow Cliffswallow, Maj, USAF

A thesis submitted in partial fulfillment
of the requirements for the degree

of

MASTER OF SCIENCE

in

Physics
(Upper Atmospheric Physics)

Approved:

Major Professor

Committee Member

Committee Member

Dean of Graduate Studies

UTAH STATE UNIVERSITY
Logan, Utah

1990

ABSTRACT

Derivation of Exospheric Temperature at High Latitudes

from Incoherent-Scatter Radar Data

by

Willow Cliffswallow, Master of Science (Maj, USAF)

Utah State University, 1990

Major Professor: Dr. Vincent B. Wickwar
Department: Physics

This thesis investigates the feasibility of using statistical methods to derive representative exospheric temperatures in the high-latitude ionosphere despite Joule heating effects. The study was based on two main premises: that Joule heating is spatially and temporally localized in the radar's field of view and that a "contaminated" neutral temperature population representing Joule heating can be separated from the non-enhanced temperature population by statistical means. Exospheric temperatures were derived from Sondrestrom incoherent-scatter radar data using the ion energy balance equation. The effect of the O^+-O collision cross section was tested by increasing it in the ion energy equation by a factor of 1.7. Since exospheric temperatures increased only an average of 10° K, the original cross section was used in the calculations. Tests also showed the calculations to be fairly insensitive to variations in the s parameter and the neutral temperature at 120 km, used in the Bates neutral temperature profile, as long as the s value was .02 or greater. Input parameters were drawn from the MSIS86 model atmosphere, and the

s values used were always greater than .02. Three tests were used to delimit the lower (non-Joule-heated) population in each cycle of radar observations: the Student *t* test, the normal distribution test, and the chi-squared test. A mean exospheric temperature was computed for each temperature population determined by the tests. Comparisons were made for 10 days of data between running averages of statistically derived exospheric temperatures and one-hour averages of Fabry-Perot optically derived temperatures. Exospheric temperatures were also extrapolated to 225 km for direct comparison to Fabry-Perot temperatures. Bivariate scatterplot analysis showed high correlations between the two data sets for all tests and for both the exospheric and extrapolated temperatures. The statistical technique appears to produce realistic and reasonably unbiased exospheric temperatures from high-latitude radar data. (100 pages)

ACKNOWLEDGEMENTS

I'd like to thank the U.S. Air Force and the Air Force Institute of Technology (AFIT) for having the faith in me to give me the opportunity to pursue my interest in this field of study and for supporting my needs during my academic assignment.

I wish to thank Dr. Vincent B. Wickwar for patiently guiding me through this research project. Our debates on points of analysis cleared away many clouds of confusion and kept the project on track. I also thank Dr. John W. Meriwether, Jr. for spending time explaining details of the Fabry-Perot data and responding to questions throughout the project. I wish to thank the National Center for Atmospheric Research (NCAR) and the SRI International for their prompt response in providing data.

I'm indebted to my officemates, Capt Michael Christie and Capt Michael Johnson, for their continuous support, encouragement, and patient help when I got stuck, both in the classroom and during the research. I also thank all the AFIT students on campus and their families, who provided camaraderie and a sense of humor when they were most needed.

This research was supported in part by contract F49620-87-K-0007 from the Air Force Office of Scientific Research. The incoherent-scatter radar and Fabry-Perot data were acquired under cooperative agreements and grants from the National Science Foundation, Division of Atmospheric Sciences, to SRI International and the University of Michigan. The data base at NCAR is also supported by the National Science Foundation, Division of Atmospheric Sciences.

Willow Cliffswallow

TABLE OF CONTENTS

Chapter Page

LIST OF TABLES

LIST OF FIGURES

ABSTRACT

Derivation of Exospheric Temperature at High Latitudes

from Incoherent-Scatter Radar Data

by

Willow Cliffswallow, Master of Science

Utah State University, 1990

Major Professor: Dr. Vincent B. Wickwar
Department: Physics

This thesis investigates the feasibility of using statistical methods to derive representative exospheric temperatures in the high-latitude ionosphere despite Joule heating effects. The study was based on two main premises: that Joule heating is spatially and temporally localized in the radar's field of view and that a "contaminated" neutral temperature population representing Joule heating can be separated from the non-enhanced temperature population by statistical means. Exospheric temperatures were derived from Sondrestrom incoherent-scatter radar data using the ion energy balance equation. The effect of the O^+-O collision cross section was tested by increasing it in the ion energy equation by a factor of 1.7. Since exospheric temperatures increased only an average of 10° K, the original cross section was used in the calculations. Tests also showed the calculations to be fairly insensitive to variations in the s parameter and the neutral temperature at 120 km, used in the Bates neutral temperature profile, as long as the s value was .02 or greater. Input parameters were drawn from the MSIS86 model atmosphere, and the

s values used were always greater than .02. Three tests were used to delimit the lower (non-Joule-heated) population in each cycle of radar observations: the Student *t* test, the normal distribution test, and the chi-squared test. A mean exospheric temperature was computed for each temperature population determined by the tests. Comparisons were made for 10 days of data between running averages of statistically derived exospheric temperatures and one-hour averages of Fabry-Perot optically derived temperatures. Exospheric temperatures were also extrapolated to 225 km for direct comparison to Fabry-Perot temperatures. Bivariate scatterplot analysis showed high correlations between the two data sets for all tests and for both the exospheric and extrapolated temperatures. The statistical technique appears to produce realistic and reasonably unbiased exospheric temperatures from high-latitude radar data. (100 pages)

CHAPTER I

INTRODUCTION

1.1 Energy Processes

Energy flow in the ionosphere has been discussed and reviewed in several articles and books. Sections 1.1-1.3 are derived mostly from Banks [1966a,b], Banks and Kockarts [1973], Schunk and Walker [1973], and Schunk and Nagy [1978]. Other references will be cited as appropriate. This summary emphasizes F-region processes.

The primary ionospheric energy source is solar XUV radiation, which produces both energetic photoelectrons through photoionization and energetic neutrals through photodissociation. The energetic photoelectrons lose energy through elastic collisions with ambient electrons and inelastic collisions with neutrals. The heated ambient electrons lose energy via Coulomb collisions with ambient ions.

Energy is transferred to the neutrals by elastic ion-neutral interactions and resonant charge exchange between ions and their parent neutrals. The original excited neutrals lose energy through superelastic collisions with other neutrals or by radiation. The process, then, is a cascade of energy through several mechanisms initiated by photons that carry energy in excess of that required for ionization and photodissociation. At F-region altitudes, the process normally results in electron temperatures that are higher than ion temperatures, which in turn exceed neutral temperatures. Typical temperature profiles [from Schunk and Nagy, 1978] are shown in Figure 1.1.

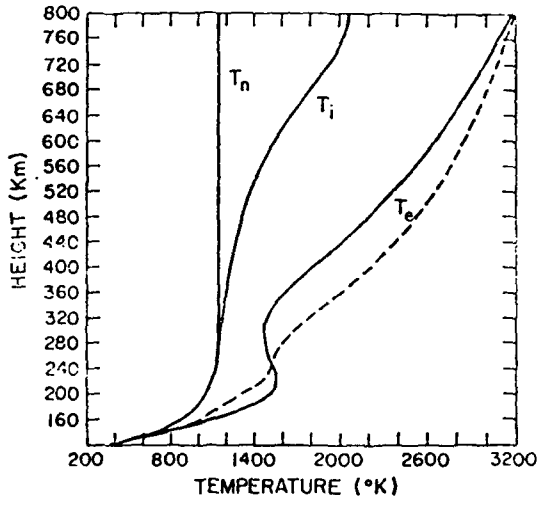

(a)

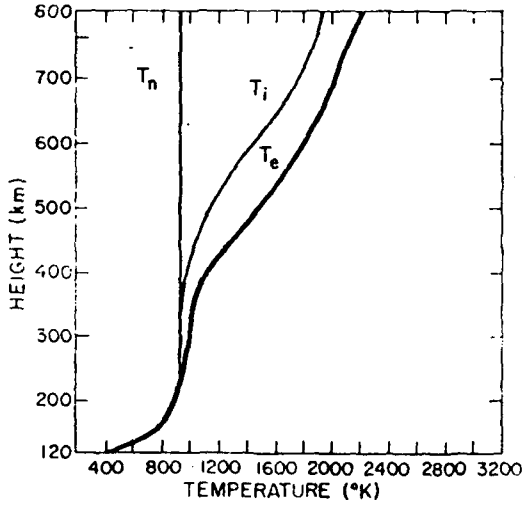

(b)

Fig. 1.1. (a) Calculated electron, ion, and neutral gas temperature profiles at 1422 LT over Millstone Hill, March 23-24, 1970, (b) Temperature profiles at 0222 LT over Millstone Hill, same day [Schunk and Nagy, 1978, from Roble, 1975]

Without solar radiation (and other heat sources), the three temperatures quickly reach equilibrium and can be considered equal. Additional heat sources at high latitudes can produce very different results, which will be discussed in a later section.

1.2 Electron Temperature

Photoelectrons lose energy at low altitudes primarily through interactions with the abundant neutrals. Cooling processes include rotational and vibrational excitation of N_2 and O_2, electronic excitation of O and O_2, and excitation of fine structure levels of O. The latter is the dominant process below 300 km, the loss rate being [Schunk and Walker, 1973]

$$\frac{dU_e}{dt} = -3.4\times10^{-12} n_e[O]\frac{(Te-Tn)}{Tn}(1-7\times10^{-5}Te) \quad eVcm^{-3}s^{-1}, \tag{1.2.1}$$

at least an order of magnitude larger than loss rates due to rotational excitation given similar neutral densities and several orders of magnitude larger than loss by vibrational excitation of N_2. Vibrational excitation of O_2 can be a significant loss mechanism in the E-region, and electronic excitation of O provides an important sink for electron temperatures greater than 3000° K.

The dominant electron cooling mechanism above 300 km is Coulomb collisions between thermal electrons and positive ions. Using a Maxwellian-averaged electron-ion collision frequency, the electron-ion cooling rate can be expressed as [Schunk and Walker, 1973]

$$\frac{dU_e}{dt} = \frac{-4(2\pi m_e)^{1/2} n_e n_i (z_i e^2)^2 k(Te-Ti)\ln\Lambda}{m_i\,(kTe)^{3/2}} \quad eVcm^{-3}s^{-1}\ , \tag{1.2.2}$$

where z_i = ion charge number, k = Boltzmann's constant, and ln Λ = the Coulomb logarithm, usually set to 15 for ionospheric temperatures and densities. For the principal ionospheric ions and assuming a common ion temperature, Eqn. (1.2.2) reduces to [Schunk and Walker, 1973]

$$\frac{dU_e}{dt} = \frac{-4.8\times10^{-7}(Te-Ti)n_e\{[O^+]+4[He^+]+16[H^+]+.5[O_2^+]+.53[NO^+]\}}{Te^{3/2}} \quad eVcm^{-3}s^{-1} . \qquad (1.2.3)$$

Mathematically, this loss rate has a maximum when Te=3Ti:

$$(dUe/dt)_{max} = \frac{-3.0\times10^{-6}n_e n_i}{A_i Ti^{1/2}} \quad eVcm^{-3}s^{-1} , \qquad (1.2.4)$$

where A_i is the ion mass in atomic mass units. For electron temperatures higher than 3Ti, for example, in a stable red auroral arc, vibrational excitation of N_2 and excitation of O to the ^1D state become important. Elastic electron-neutral cooling rates are on the order of 10^4 less than Eqn. (1.2.3) and are usually considered negligible.

Thermal conduction is a significant factor in determining electron temperature profiles but does not determine flow of energy to the ions, and so will not be considered in this study.

1.3 Ion Temperature

Ions are heated mainly by collisions with thermalized electrons. Photoelectrons do not efficiently transfer energy to the ambient ions because the collision cross section varies as the inverse 4th power of their relative velocity. The ion heating rate due to collisions with thermal electrons is equivalent to the

electron loss rate given by Eqn. (1.2.2), which for singly charged ions reduces to

$$Q_i = \frac{7.7\times10^{-6} n_e n_i (Te-Ti)}{A_i Te^{3/2}} \qquad eVcm^{-3}s^{-1} \ . \tag{1.3.1}$$

Barring other heat sources, the ion temperature is usually equal to or less than the electron temperature. Different ions may attain different temperatures, but ion-ion energy transfer, which is very efficient, keeps the temperature difference minimal, and common temperatures can usually be assumed.

The ions are cooled through elastic ion-neutral interactions and resonant charge exchange between ions and their parent neutrals. An induced dipole attraction results in elastic ion-neutral interactions at low temperatures (< 300° K) at rates that depend on the polarizability of the neutral but are independent of relative velocity. At higher temperatures, calculated transfer rates depend on polarizability and the ion-neutral temperature difference. The dominant cooling mechanism for ions at high temperatures is resonant charge exchange. Each particle involved tends to retain its own kinetic energy, producing a hot neutral and cool ion pair from a cool neutral and a hot ion. The collision cross section for this interaction is about twice the elastic interaction cross section [Banks, 1966b]. The charge exchange cross section is velocity dependent, but average cross sections and collision frequencies, assuming Maxwellian velocity distributions, have been calculated for applicable ion-neutral pairs [Banks, 1966b; Banks and Kockarts, 1973]. The energy transfer rate is then reduced to

$$\frac{dU_i}{dt} = -\gamma_{in} n_i n_n (Ti+Tn)^{1/2}(Ti-Tn) \qquad eVcm^{-3}s^{-1} \ , \tag{1.3.2}$$

where γ_{in} for O^+-O interactions is 2.1×10^{-15} $eVcm^{-3}s^{-1}{}^oK^{-3/2}$.

Thermal conduction is important for ions above 600 km, which is above the altitude of interest for this study.

1.4 Joule Heating at High Latitudes

The high-latitude energy systems are complicated by electrodynamic coupling between the magnetosphere, the ionosphere, and the thermosphere. Closure of magnetospheric current systems within the ionosphere through field-aligned Birkeland currents and horizontal currents interact with the ionosphere and affect composition, winds, and temperatures [e.g., Roble et al., 1982; Straus and Schulz, 1976; Kelly and Wickwar, 1981; Killeen, 1987]. Temperatures are affected by large-scale DC electric fields, which result in Joule heating, and by energetic particle precipitation, which produces large amounts of local ionization. The effects are highly variable, changing quickly with substorms and other magnetospheric disturbances.

The local energy input to the neutral atmosphere near the auroral oval is comparable for both particle and Joule heating [Banks, 1977]. However, precipitating electrons penetrate to low altitudes, creating an enhanced electron density peak in the E-region between 90 and 130 km [Wickwar, 1975; Banks, 1977]. Since Joule heating rates peak at higher altitudes, the energy input per neutral particle is greater, and the Joule heating effect is several times that of particle precipitation [Foster et al., 1983; Banks, 1977].

Joule heating of the ions results from perpendicular electric fields driving the

plasma through the neutrals, enhancing the ion-neutral collision rate, changing directed motion into random motion, and dissipating kinetic energy as thermal energy. The process can be approached through the time-dependent ion energy equation, as used by Baron and Wand [1983] and St.-Maurice and Hanson [1982]:

$$\frac{dTi}{dt} = \frac{\nu_{in}[Tn-Ti+m_n(\mathbf{u}_i-\mathbf{u}_n)^2]}{3k} \quad . \tag{1.4.1}$$

The time constant for dTi/dt is approximately $1/\nu_{in}$, a few tens of seconds in the F-region, showing the rapid response of Ti to changes in relative velocity. St.-Maurice and Hanson [1982] attempted to extract Tn and $\mathbf{u}_n$ from Ti and $\mathbf{u}_i$ data, but often found several solutions which fit the data set. Watkins and Banks [1974] included both electron energy transfer and Joule heating to calculate Tn, setting $\mathbf{u}_n$=0. Their calculated neutral temperatures showed inconsistent variations from expected behavior, emphasizing the importance of $\mathbf{u}_n$.

The other approach is by calculating Joule heating rates directly [Banks et al., 1981; Foster et al., 1983], by

$$q_j = \sigma_p E^{*2} \tag{1.4.2}$$

where $\mathbf{E}^* = \mathbf{E} + \mathbf{u}_n \times \mathbf{B}$, σ_p = Pedersen conductivity, and q_j = Joule heating rate. In the ionosphere, $\mathbf{E} = -\mathbf{u}_i \times \mathbf{B}$, and can be derived from ion convection velocities. But $\mathbf{u}_n \times \mathbf{B}$ can be significant, and $\mathbf{u}_n$ is not known. Foster et al. [1983] set $\mathbf{u}_n$ to zero and integrated the Pedersen conductivity over height. Banks et al. [1981] used model $\mathbf{u}_n$ and conductivities, also integrated over height. Uncertainties in this method result from nonuniform Pedersen conductivities (as in winter), enhanced

conductivities during intense precipitation, which can increase q_j four to five times, and an unknown neutral wind, which can either reduce or enhance the heating.

Because crucial data cannot presently be measured on a real time basis, Joule heating effects cannot be accurately determined on realistic time and space scales. However, several studies by the authors mentioned in this section [plus Alcaydé et al., 1984] found similar features: a highly structured, highly variable Joule heating pattern, usually with heating areas in the dawn and dusk sunward convection channels, with intense heating events seldom lasting more than a few hours (the time constant for transfer of momentum to the neutrals), and with pronounced seasonal variations. Plots of calculated Joule heating from Banks et al. [1981] are shown in Figure 1.2.

An example of Joule heating as seen in Sondrestrom incoherent-scatter radar data is shown in Figure 1.3, provided by V. B. Wickwar [Utah State University, unpublished data, 1990]. The ion convection pattern demonstrates the relationship of high ion velocities to high ion temperatures. The location of intense Joule heating in the dawn sunward convection channel is consistent with model results. Figure 1.4 [V. B. Wickwar, Utah State University, unpublished data, 1990] shows a progression of Joule heating events over time and invariant latitude, from Sondrestrom radar data. Ion temperature enhancements appear in the 1546 to 1552 UT block, seem to move back and forth in latitude over time, and virtually disappear by the 1749-1756 UT block. The entire sequence spans about two and a half hours, and the Joule heating areas vary in latitude, altitude, and time. At no time in this sequence does a single Joule heating area cover more than three degrees of latitude.

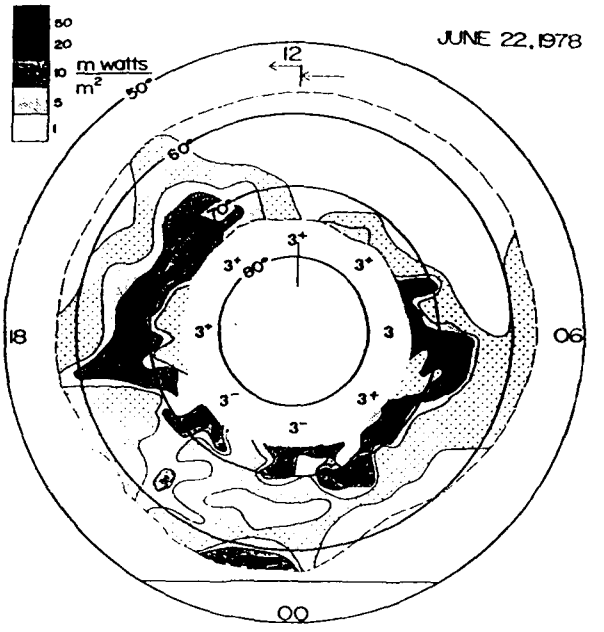

(a)

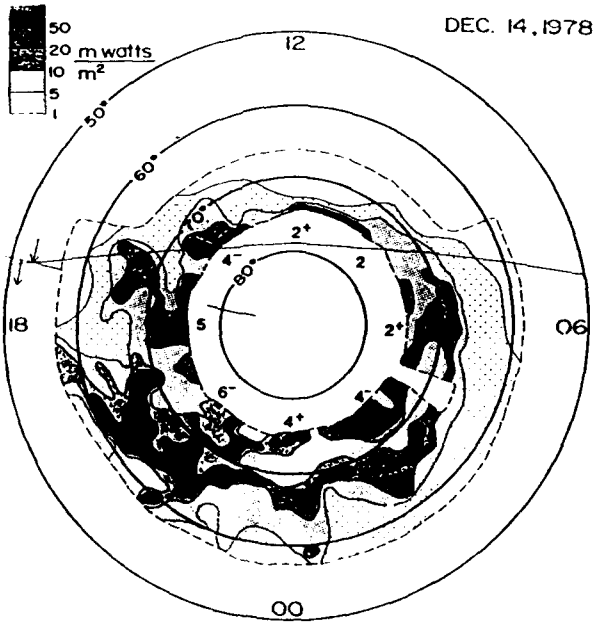

(b)

Fig. 1.2. (a) Calculated Joule heating results for June 22, 1978, plotted in local time and invariant latitude. Kp values are in center circle. (b) Joule heating rates for December 14, 1978 [Banks et al., 1981].

Fig. 1.3. Ion temperatures and convection velocities, from the Sondrestrom radar.

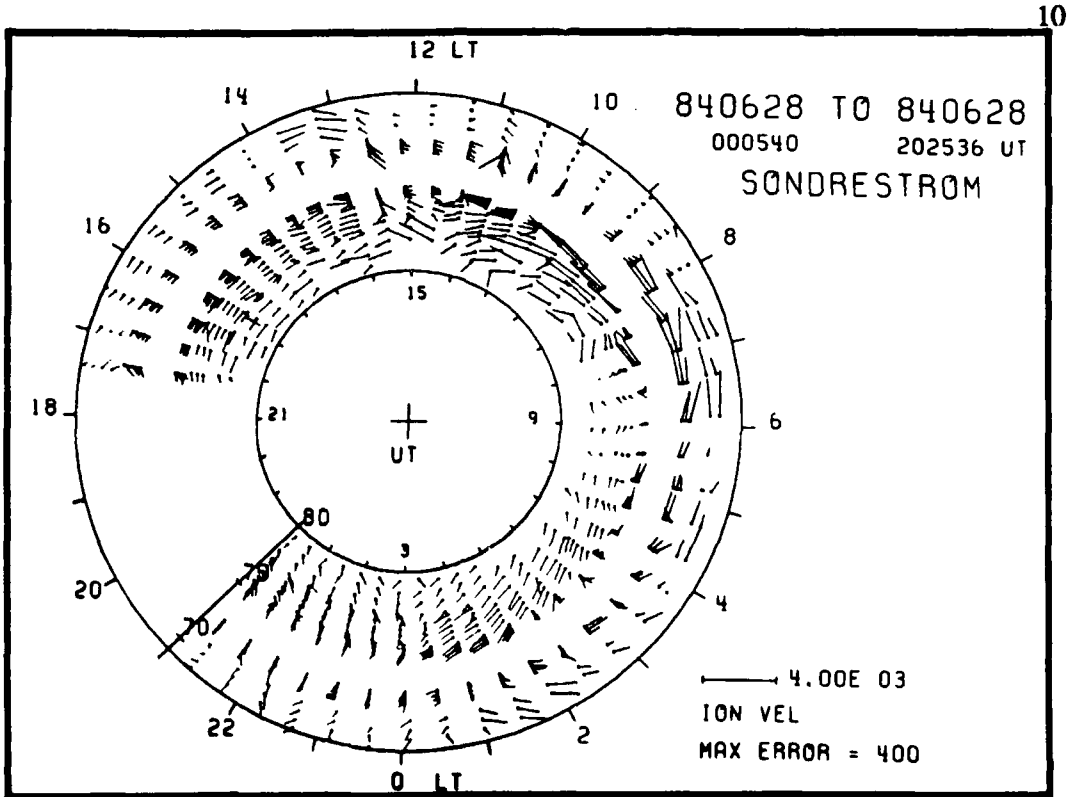
12 LT
14
10
16
8
18
6
20
4
22
2
0 LT
15
21
9
3
UT
80
70
840628 TO 840628
000540
202536 UT
SONDRESTROM
4.00E 03
ION VEL
MAX ERROR = 400

Fig. 1.4. Evidence of Joule heating in ion temperatures measured by the Sondrestrom radar.

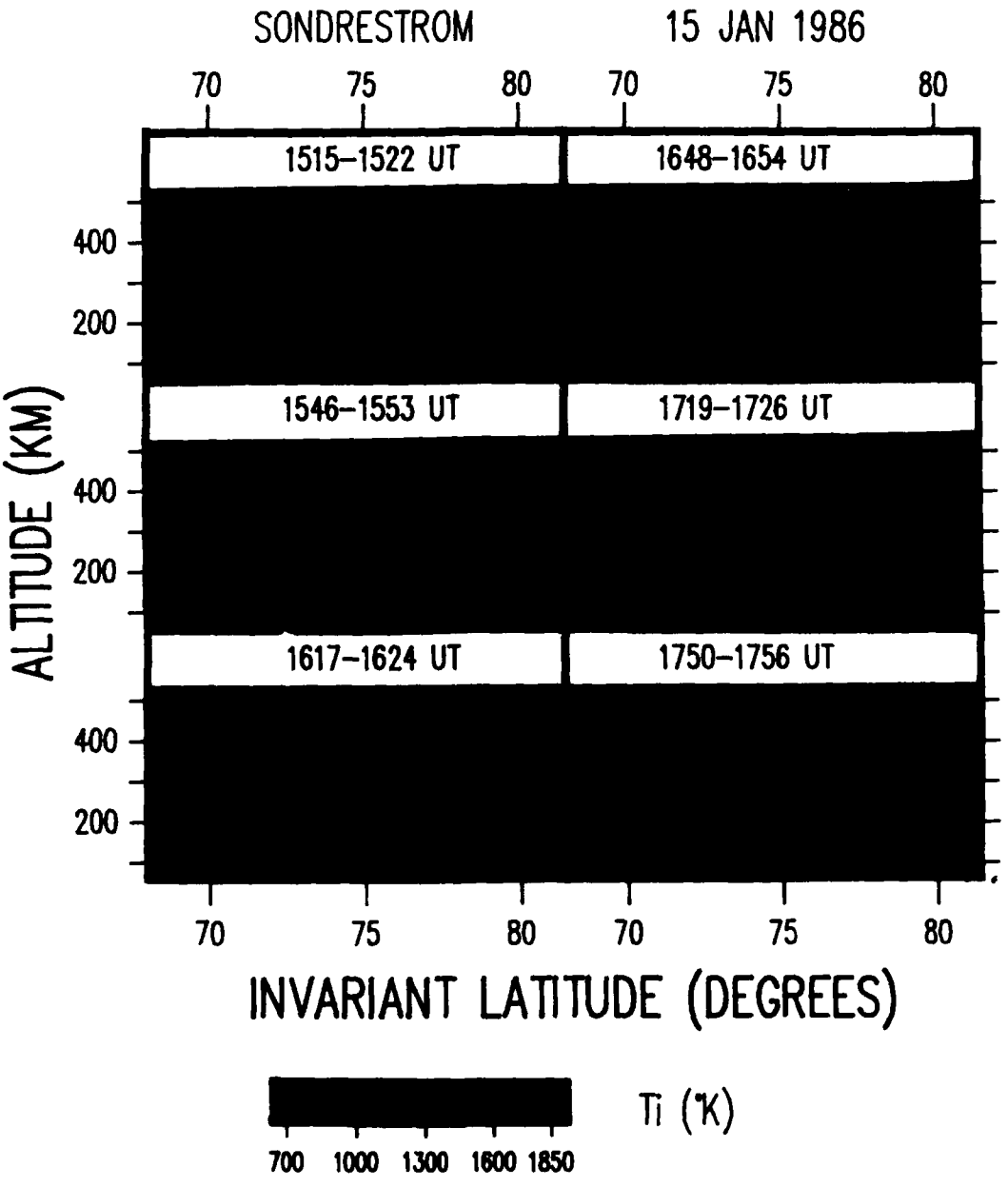
SONDRESTROM
15 JAN 1986
70
75
80
70
75
80
1515–1522 UT
1648–1654 UT
1546–1553 UT
1719–1726 UT
1617–1624 UT
1750–1756 UT
400
200
400
200
400
200
ALTITUDE (KM)
70
75
80
70
75
80
INVARIANT LATITUDE (DEGREES)
Ti (°K)
700
1000
1300
1600
1850

The effect on the neutral atmosphere is also variable. Killeen et al. [1984] analyzed direct measurement data from six polar passes of the Dynamics Explorer 2 satellite. They found clear examples of ion temperature enhancements of more than 1000° K, associated with high relative ion velocities and low electron densities (due to enhanced dissociative recombination). But the neutral temperature increases were much smaller (tens of degrees), and spread over a broader region, because of the higher heat capacity of the neutral atmosphere. The horizontal scale length for the neutral temperature field is approximately $(\lambda Tn/Q)^{1/2}$, where λ is the thermal conductivity and Q is the heating rate. 200 km is considered the minimum horizontal scale length of large scale fluctuations around the 350 km altitude, although 500 km may be considered reasonable [St.-Maurice and Hanson, 1982]. So, the neutral temperature is not expected to vary much over 10 degrees of latitude, despite localized Joule heating events. It takes a long-duration, large-intensity Joule heating event to significantly alter thermospheric temperatures.

The structured, usually localized nature of Joule heating and the large spatial scale of F-region neutral temperatures form the basic assumption for this thesis - that high-latitude exospheric temperatures can be derived by "working around" the Joule heating rather than trying to calculate its contribution.

1.5 Previous Research

The ion energy equation is commonly used to derive exospheric temperatures from incoherent-scatter radar data. The basic method consists of equating the ion heating rate (Eqn. (1.3.1)) to the ion cooling rate (Eqn. (1.3.2)), assuming an O^+-O regime:

$$4.8\times10^{-7}n_e^2\frac{(Te-Ti)}{Te^{3/2}} = 2.1\times10^{-15}n_e[O](Ti+Tn)^{1/2}(Ti-Tn) \quad eVcm^{-3}s^{-1} \qquad (1.5.1)$$

or

$$Ti-Tn = \frac{2.29\times10^{8}n_e(Te-Ti)}{[O]Te^{3/2}(Ti+Tn)^{1/2}} \quad eVcm^{-3}s^{-1} \; . \qquad (1.5.2)$$

With Te, Ti, and n_e known from radar measurements and [O] estimated from models, the exospheric temperature T_{ex} can be regressed on assuming a Bates [1959] profile:

$$Tn = T_{ex}-(T_{ex}-T_{120})\exp[-s(z-120)] \; , \qquad (1.5.3)$$

either assuming a temperature at 120 km (T_{120}) and an s parameter, or estimating them from models.

Waldteufel and Cogger [1971] derived T_{ex} in this manner from low-latitude Arecibo radar data. Burnside et al. [1988] used this method (also for Arecibo data) to derive T_{ex} by regressing the equation on T_{ex} to fit the observed electron density profiles. Evans et al. [1979] reviewed the use of a similar equation to derive T_{ex} from radar data and noted that exospheric temperatures at high latitudes would be extremely useful to have, but the ion energy equation is invalid when ion temperatures are enhanced by frictional heating. Bauer et al. [1970] and Alcaydé et al. [1972] made similar studies using the ion energy equation and mid-latitude St. Santin radar data.

Alcaydé et al. [1983] attempted to estimate the contribution of Joule heating in the equation

$$L_{in} = [O]n_e[\frac{3}{2}k(Tn-Ti)+\frac{1}{2}m(O)(v_i-v_n)^2] \qquad (1.5.4)$$

by assuming the relative velocity is constant in the F-region and the neutral temperature can be estimated from a derived pseudo-temperature and a constant:

$$T^*(z) = Tn(z) + K \quad , \qquad (1.5.5)$$

where $K = [m(O)/3k](v_i - v_n)^2$. Their method of determining K was invalidated by the presence of soft particle precipitation, which they tried to identify. The technique lowered the inferred exospheric temperatures, but no comparison was made to temperature measurements from other sources, so it's hard to determine the accuracy of the results.

Oliver [1984] derived exospheric temperatures over 25 to 60 degrees latitude from Millstone Hill incoherent-scatter radar data using the basic ion energy equation. He makes no attempt to compensate for Joule heating, but notes that very high neutral temperatures are contaminated by its effects.

Watkins and Banks [1974] derived exospheric temperatures from Chatanika radar data (65°N latitude). To include the Joule heating term, they assumed that when the ion velocity is large, it approximates the relative velocity between the ions and the neutrals (i.e., $\mathbf{u}_n$=0). Their derived neutral temperatures sometimes showed abrupt decreases or increases as the method overestimated or underestimated the Joule heating.

Obviously, this is not an easy problem to deal with. This thesis attempts an entirely new approach to dealing with the derivation of exospheric temperatures at high latitudes - a statistical approach.

CHAPTER II

THE INSTRUMENTS

2.1 The Sondrestrom Incoherent-Scatter Radar

The Sondrestrom incoherent-scatter radar, located in Sondre Stromfjord, Greenland, at 74 degrees invariant latitude, is the northernmost of a meridional chain of four radars. Its field of view includes, at different times, the cusp, the polar cap, and the poleward portion of the auroral oval. Midnight local solar time is 0324 UT, and midnight magnetic local time is 0157 UT at equinox.

The "world-day" observation mode pattern initially consisted of three parts [Wickwar et al., 1984]. First is a pattern of eleven fixed positions. Five pairs of observing directions are symmetrically placed in two planes 20° off the vertical. The planes intersect at -27° azimuth, approximately the invariant magnetic meridian. The elevation angles of the pairs are 30, 50, and 65° looking toward the north, and 30 and 50° looking toward the south. The eleventh direction is parallel to the local magnetic field. The second part of the pattern is an elevation scan from 30° elevation in the south to 30° elevation in the north in the magnetic meridian plane, and the third part is a similar elevation scan perpendicular to the previous one.

The observing period is 15 min for the fixed position cycle and 5 min for each scan. Data are collected between 80 and 550 km in altitude, and cover 68 to 81° invariant latitude at 500 km in the first two parts of the pattern. Most observations are made with a 320-μs pulse to minimize the uncertainty in the F-region.

This pattern had several later variations: the second elevation scan was

dropped; the number of fixed points was occasionally reduced to nine; two extra observations parallel to the magnetic field were occasionally added; and the elevation angles and ranges were adjusted.

2.2 Derivation of Physical Parameters from Radar Data

Radio waves transmitted by an ionosonde (1-20 MHz) are reflected back when the frequency matches the plasma frequency, about 1-10 MHz in the high-latitude ionosphere. Incoherent-scatter radars operate in the 50 to 1290 MHz range, and the transmitted waves pass through the ionosphere except for a small amount of energy scattered by ionospheric electrons [Kelley, 1989]. The scattering cross section of electrons is independent of incident wavelength [Evans, 1969], and the oscillating electrons reradiate energy at almost the same wavelength [Kelley, 1989]. The total power of the return is directly related to electron density.

The spectrum of the reflected signals was initially expected to have a half-power width proportional to the Doppler shift, or mean thermal motion, of the electrons. It is, in fact, dependent on the mean ion thermal motion because of the influence of the ions when the transmitted wavelength (λ) is much larger than the Debye length (D) [Evans, 1969]. So, the scattering is actually not from individual electrons but from density fluctuations arising from longitudinal oscillations in the plasma.

The power spectrum of reflected signals has an electronic component and an ionic component. As the factor $\alpha = 4\pi D/\lambda$ decreases, the largest part of the energy appears in the ionic component. This is the situation for the existing radars. The ionic component will change shape in a way that depends on the ratio Te/Ti. This

dependence has been very well determined by several independent theoretical calculations [c.f., Evans, 1969]. Measurement of the spectral shape can be made using a filter bank as a spectrum analyzer or by digital sampling and computer analysis - the usual method today. The width of the spectrum can be used to infer Ti and more information about the shape to also infer Te/Ti. A more complete analysis involves the full shape of the spectrum. But the width, as well as the shape, depends on ion mass and composition [Evans, 1969]. If the ion mass is not known, Ti cannot be determined uniquely. If ion composition is known, both Ti and Te can be derived. For this study the data came from an altitude region (250 to 500 km) where it was reasonable, most of the time, to assume almost entirely O^+ ions.

If the plasma is drifting as a whole, the entire spectrum shows a Doppler shift without change in shape and is used to derive the line-of-sight velocity of the ions. In the E-region, ions can be driven across the magnetic field, and plasma motion serves as a tracer for the neutral wind [Evans et al., 1979].

2.3 The Fabry-Perot Interferometer

The Fabry-Perot interferometer consists of two flat parallel semi-transparent mirrors separated by a fixed distance. Incident light undergoes multiple reflections, producing a pattern of bright concentric rings (or fringes) on a dark background. Wavelength is transformed into a radial displacement on the detector, broadened by effects of the instrument [Hernandez, 1980]. Azimuthal integration as a function of radius transforms the fringe pattern into a spectrum. The analysis procedure fits theoretical spectra, modified for instrumental effects, to the observed spectrum. The

fit yields the relative emission rate, the line-of-sight neutral wind, and the neutral gas temperature.

Winds are determined from the Doppler shift of the emission line relative to a zenith measurement reference line, which assumes vertical winds to be zero on average. Temperature is deduced from the Doppler width of the line profile, assuming a Maxwellian velocity distribution. The emissions usually studied in the F-region come from metastable atomic states, which implies that the emitting particles have had time to reach representative temperatures and velocities through collisions. For example, the life of $O(^1D)$ is about 110s, much greater than the typical time between collisions.

The emission line used most in nighttime thermospheric studies is the 630.0 nm line of atomic oxygen in the metastable ^1D state. Outside of auroral zones, the main source for $O(^1D)$ is ion-atom interchange followed by dissociative recombination [Wickwar et al., 1974]:

$$O^+ + O_2 \rightarrow O_2^+ + O \qquad (2.3.1)$$

$$O_2^+ + e \rightarrow O + O(^1D) \quad . \qquad (2.3.2)$$

$O(^1D)$ returns to its ground state predominantly by emission of radiation at 630.0 or 636.4 nm or by quenching collisions with molecular nitrogen:

$$O(^1D) \rightarrow O(^3P) + h\nu \qquad (2.3.3)$$

$$O(^1D) + N_2 \rightarrow O(^3P) + N_2 \quad . \qquad (2.3.4)$$

Using the dissociative recombination model, Wickwar et al. [1974] found the peak of the volume emission rate to vary between 250 and 300 km, temporally following

the variation in the height of maximum electron density. Descent of the emission layer is limited by enhanced quenching from increased N_2 densities.

Cogger et al. [1980] also produced theoretical calculations based on dissociative recombination, but allowed for some destruction of O_2^+ by the reaction

$$O_2^+ + N \rightarrow NO^+ + O \quad . \tag{2.3.5}$$

Their theoretical volume emission rate profiles had peaks at about 280 km for minimum surface brightness values and about 240 km for maximum brightness.

Rees and Roble [1986] looked at six processes capable of producing $O(^1D)$ atoms in the aurora. Based on their auroral model, they concluded the principal sources of $O(^1D)$ are the reaction

$$N(^2D) + O_2 \rightarrow NO + O(^1D) \tag{2.3.6}$$

and dissociative recombination of O_2^+, the latter dominating below 280 km. Their model total emission rate for an electron spectrum with 0.4 KeV characteristic energy peaks at about 200 km. For 0.1 KeV and 2.0 KeV energies, model emission altitude peaks are about 240 and 180 km respectively.

Meier et al. [1989] support electron impact excitation of atomic oxygen as the main source of $O(^1D)$ in auroras:

$$O + e \rightarrow O(^1D) + e \quad , \tag{2.3.7}$$

with dissociative recombination as second most important. Their calculated emission peaks appear to fall at about 250 and 225 km for characteristic electron energies of 0.25 KeV and 2.0 KeV respectively. Thus, their peak altitudes are significantly

above those of Rees and Roble [1986], and close to the 225 km altitude assumed for this study.

Yee [1988] questioned the assumed Gaussian shape of the 630.0 nm emission line profile. His calculations of the velocity distribution of $O(^1D)$ show a non-thermal profile, which becomes more non-thermal with height. The non-thermal signature may be hard to detect, but would result in higher deduced temperatures because of the broadened wings, and may account for Doppler temperatures sometimes being consistently higher than other temperature observations.

Although 225 km will be assumed for the average emission height of the Fabry-Perot temperatures for the sake of comparison to radar-derived temperatures, consideration of possible variations in the emission layer will be used when significant discrepancies exist.

Fabry-Perot observations are naturally limited to dark, clear nights, which at high latitudes also implies winter instead of summer. Because they provide direct measurements of neutral temperatures, they are extremely useful for comparison to observations made by other measurement techniques, despite the uncertainty in the emission height.

CHAPTER III

REDUCTION OF THE DATA

3.1 The Computer Program

The program used to process the radar data is called TOSS4, developed primarily by P. Bauer and D. Alcaydé, and reflects the research approach used by Bauer et al. [1970]. TOSS4 uses the ion energy balance equation to produce predicted ion temperatures (Ti*), which by iterations it fits to the measured ion temperature altitude profile via a nonlinear regression fitting routine. The equation for Ti* is derived from the equation for heating of O^+ by thermal electrons (see Eqn. 1.3.1):

$$Q_i = \frac{4.8\times10^{-7}\,(Te-Ti)\,n_e^2}{Te^{3/2}} \qquad eVcm^{-3}s^{-1} \tag{3.1.1}$$

and from the equation for ion cooling by energy transfer from O^+ to both O and N_2 (see Eqn. 1.3.2 and Banks [1966b]):

$$L_{in} = \{2.1\times10^{-15}[O](Ti+Tn)^{1/2} + 6.6\times10^{-14}[N_2]\}(Ti-Tn)n_e \qquad eVcm^{-3}s^{-1} \tag{3.1.2}$$

Heating and cooling rates are assumed to be equal to each other. The equation used for the predicted ion temperature Ti*, then, is

$$Ti^* = Tn + \frac{(Te-Tn)2.29\times10^{8}\,n_e}{Te^{3/2}\{[O](Ti+Tn)^{1/2}+31.4[N_2]\}+2.29\times10^{8}n_e} \tag{3.1.3}$$

Ti on the right side of the equation is the measured Ti. Other inputs needed are:

N_2 density at 120 km (N2120)

O density at 200 km (O200)

measured electron density (n_e)

measured electron temperature (Te)

estimated neutral temperature (Tn).

The N_2 and O densities are calculated for the required altitudes assuming diffusive equilibrium. N2120 and O200 can be set in the program or drawn from a model atmosphere. The neutral temperature is calculated from a modified Bates profile, basically,

$$Tn = T_{ex} - (T_{ex} - T120)\exp[-s(z-120)] \qquad (3.1.4)$$

modified by geopotential height factors. T_{ex} is the estimated exospheric temperature.

The s parameter is a factor related to the slope of the neutral temperature altitude profile, or how fast the neutral temperature is changing with altitude. Starting from the same T120 (the neutral temperature at 120 km), a lower s value would result in a shallower profile, more rapid temperature changes with height, and a higher T_{ex}.

The s parameter and T120, can be set in the program or drawn from a model atmosphere. A value for the exospheric temperature is initially assumed and then changed by iterations until the best fit for the Ti* values to the measured ion temperature values is obtained. The output of the program is the final T_{ex} with an error bar.

The program is also capable of regressing on T_{ex} and s simultaneously, starting with the T_{ex} obtained in the first regression, and on T_{ex} and [O], using the s

parameter obtained in the second regression. However, because of the variability of results and seeming difficulties involved in the higher regressions, it was decided to use only the regression on T_{ex}. This first-order regression was stabilized considerably by using MSIS86 model data as input for N2120, O200, s, and T120. The s parameter is not an MSIS output, but was calculated for each data record by using the MSIS calculated T120, T_{ex}, and Tn at each input altitude from the data record, and then averaging these s parameters. In other words,

$$s_i = \frac{\ln[(T_{ex}-T120)/(T_{ex}-Tn_i)]}{z_i-120} \qquad (3.1.5)$$

$$s = \frac{\Sigma s_i}{n} \quad . \qquad (3.1.6)$$

TOSS4 also includes a correction factor for estimated Joule heating, but this option was turned off. Based on the arguments in Chapter I, Joule heating cannot be estimated accurately enough to determine its specific contribution.

3.2 The Effect of the s Parameter

The effect of the s parameter on the calculation of exospheric temperature was examined using a similar, but simpler, program written by Wlodek Kofman. The program was run with s changing progressively from .01 to .035 in increments of .005. There was a marked effect on temperatures when s was less than .02, with differences of 100 to 200 degrees between those calculated with an s of .01 and those calculated with an s of .02 or higher. But the variation in the temperatures with an s of .02 to .035 was generally 50 degrees or less. The effect of varying T120 was checked simultaneously. T120 had its biggest impact when s was less

than .02, but made very little difference with larger s values. The direction of the variation is to decrease T_{ex} when either s or T120 is increased.

Tables 3.1 and 3.2 summarize the results of these manipulations for two data records. The s values calculated from MSIS were usually .02 or greater, so their possible impact on the accuracy of exospheric temperatures was considered small.

3.3 The Effect of the O^+-O Collision Cross Section

Burnside et al. [1987] found that the O^+-O collision cross section recommended by Banks [1966b] should be increased by $1.7_{-0.3}^{+0.7}$. To test the effect of the O^+-O collision cross section on the exospheric temperatures produced by TOSS4, the program was run on two days of data using the increased cross section. Although some exospheric temperatures increased by as much as 25 degrees, the average increase was 10 degrees. The possible effect on the results of the research was not considered significant enough to redo all the calculations.

3.4 The Radar Data

All radar data were obtained from either NCAR or SRI on magnetic tape in NCAR Incoherent Scatter format. Several criteria were used for selecting data from the records:

(1) Only altitudes between 250 km and 500 km were used.

(2) Only data quality-coded as "good" were used.

(3) If Ti was greater than Te at a specific altitude, all the data for that altitude were rejected. This was necessary because the energy balance equation mathematically assumes Ti to be between Te and Tn.

Table 3.1. The Effect of s and T120 on T_{ex} (from Jan. 27, 1987 data)

s	T_{ex}	T120
.100E-01	1014	326.16
.150E-01	934	326.16
.200E-01	904	326.16
.250E-01	894	326.16
.300E-01	884	326.16
.350E-01	884	326.16

s	T_{ex}	T120
.100E-01	1024	300.00
.100E-01	1014	350.00
.100E-01	994	400.00
.100E-01	984	450.00
.100E-01	974	500.00
.150E-01	934	300.00
.150E-01	934	350.00
.150E-01	924	400.00
.150E-01	924	450.00
.150E-01	914	500.00
.200E-01	904	300.00
.200E-01	904	350.00
.200E-01	904	400.00
.200E-01	904	450.00
.200E-01	894	500.00
.250E-01	894	300.00
.250E-01	894	350.00
.250E-01	894	400.00
.250E-01	894	450.00
.250E-01	894	500.00
.300E-01	884	300.00
.300E-01	884	350.00
.300E-01	884	400.00
.300E-01	884	450.00
.300E-01	884	500.00
.350E-01	884	300.00
.350E-01	884	350.00
.350E-01	884	400.00
.350E-01	884	450.00
.350E-01	884	500.00

Table 3.2. The Effect of s and T120 on T_{ex} (from Jan. 27, 1987 data)

s	T_{ex}	T120
.100E-01	1301	348.76
.150E-01	1201	348.76
.200E-01	1161	348.76
.250E-01	1141	348.76
.300E-01	1131	348.76
.350E-01	1131	348.76

s	T_{ex}	T120
.100E-01	1311	300.00
.100E-01	1301	350.00
.100E-01	1291	400.00
.100E-01	1281	450.00
.100E-01	1271	500.00
.150E-01	1201	300.00
.150E-01	1191	350.00
.150E-01	1191	400.00
.150E-01	1191	450.00
.150E-01	1181	500.00
.200E-01	1161	300.00
.200E-01	1161	350.00
.200E-01	1161	400.00
.200E-01	1151	450.00
.200E-01	1151	500.00
.250E-01	1141	300.00
.250E-01	1141	350.00
.250E-01	1141	400.00
.250E-01	1141	450.00
.250E-01	1141	500.00
.300E-01	1141	300.00
.300E-01	1131	350.00
.300E-01	1131	400.00
.300E-01	1131	450.00
.300E-01	1131	500.00
.350E-01	1131	300.00
.350E-01	1131	350.00
.350E-01	1131	400.00
.350E-01	1131	450.00
.350E-01	1131	500.00

(4) Data for at least two altitudes were needed to perform the regression. The criteria resulted in a general pattern of accepting most records during the daytime and rejecting many of them at night, when the signal is weakest.

Printouts of observing positions for all available data records were used to determine start and stop times for observing cycles. All observing positions in fixed position cycles were used. For elevation scans, only the scan along the magnetic meridian was used.

Temperatures in each observing cycle were manipulated by statistical routines to produce a weighted mean exospheric temperature and an error of the mean for each cycle. These temperatures were plotted, along with an average MSIS temperature for each cycle, against the mean time of the cycle. The mean temperatures were then used to calculate three-point running averages, again weighted. For comparison to the Fabry-Perot temperatures, the running averages were linearly interpolated to the Fabry-Perot times. Scatter plots were made with the two temperature sets, and weighted correlation coefficients and lines of least-squares fit were computed. The interpolated radar temperature sets were also used to compute temperatures at 225 km (average emission height for the Fabry-Perot observations), using s parameters and T120s from the appropriate times in the radar data, and the comparison process repeated. Weighted mean differences were computed for each bivariate data set, using the equation:

$$\langle T_r - T_{fp} \rangle = \frac{\Sigma (T_r - T_{fp})_i w_i}{\Sigma w_i} \qquad (3.4.1)$$

where $w_i = 1/(\sigma_r^2 + \sigma_{fp}^2)_i$.

3.5 The Fabry-Perot Data

The processed Fabry-Perot interferometer data were obtained directly from Dr. John W. Meriwether, Jr. at Geophysics Laboratory, Hanscom AFB, MA for 1983 and 1987. Data for 1988 were obtained from NCAR on magnetic tape, and had been provided and reduced by Dr. Rick Niciejewski, University of Michigan. Pre-1988 data had been screened by Dr. Meriwether and were considered good data. 1988 data included cloud cover information, and only data with cloud cover codes of three or less were used. Weighted means of the temperatures were computed for one hour periods, centered on the hour. This time period included slightly more than one observation cycle, but was chosen for ease of comparison. No temperatures with uncertainties of more than 150 degrees were used (on advice of Dr. Meriwether). Solar zenith angles for each day were checked for possible contamination of the temperatures. A solar zenith angle of 95 degrees or less resulted in rejection of the temperature, and generally temperatures located between solar zenith angles of 95 to 100 degrees were rejected as being unrealistically high and therefore probably contaminated. Lunar data were also checked for moonlight contamination, but no problems were found. Some Fabry-Perot temperatures were not used for comparison to radar temperatures because of large data gaps (2 hours or more) in the radar temperatures. No other manipulation was done with the optically derived temperatures.

CHAPTER IV

STATISTICAL TESTS

4.1 Introduction

As noted in Chapter I, researchers who have struggled to compensate for Joule heating effects in the high-latitude thermosphere suffer from a lack of data. Although Joule heating can be quite significant to global temperature and circulation patterns, the immediate impact on exospheric neutral temperatures is probably and usually not great. The highly structured and typically localized morphology of Joule heating suggests that a statistical approach to the observed data might result in identification and isolation of Joule heating areas, not in a physical sense but statistically in the temperature distribution pattern.

The observation cycles of the incoherent-scatter radar considered for this study consisted of 9, 11, or 13 fixed position observations, or of 15 observations in an elevation scan along the magnetic meridian. Both scan types cover about 10 degrees of latitude. If indeed 10 degrees of latitude contains both Joule-heated areas and non-heated areas, the distribution of the ion temperatures should somehow reveal two disparate populations. Neutral temperatures calculated via the ion energy balance equation closely follow the ion temperatures, and exospheric temperatures will be high if determined from a high ion temperature profile. Figure 4.1 shows the tremendous variability in calculated exospheric temperatures over a 20 hour period in September, 1983. All calculated temperatures are shown, with each observation cycle covering about 15 min. Temperatures in the group centered around 1430 UT range from 900° to almost 2000° K.

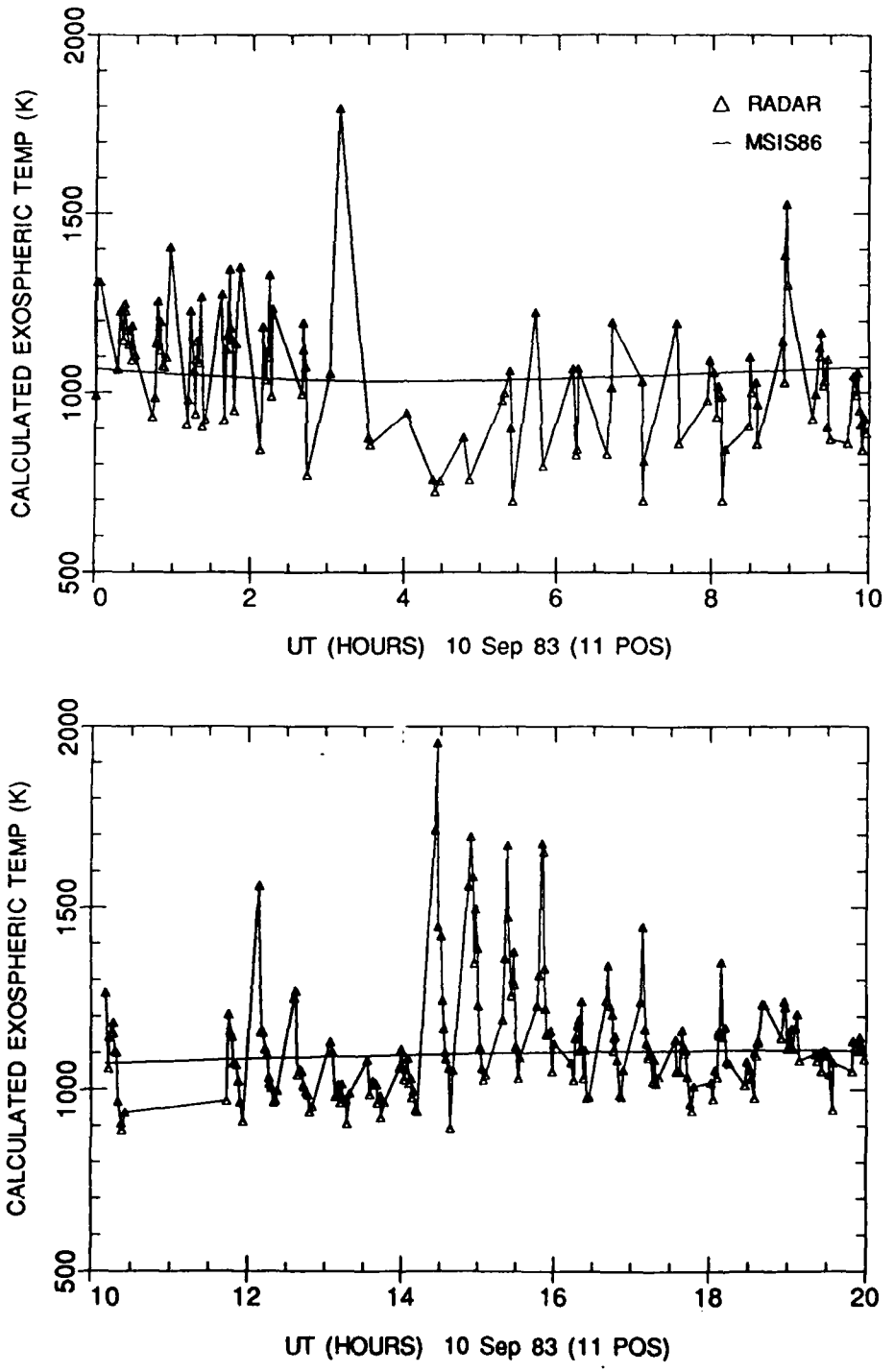

Fig. 4.1. Calculated exospheric temperatures (output of TOSS4).

Neutral temperatures in a non-Joule-heated regime are expected to exhibit a normal distribution over a limited latitude range. If the temperature populations can be separated, the neutral exospheric temperature can then be calculated as the weighted mean of the temperatures in the "normal" (non-heated) distribution, as might be done directly at mid- or low-latitudes.

In an early effort, the minimum temperature was extracted from each cycle and the mean was estimated based on where that temperature was expected to fall in a sample of size N, for example, the lowest 10% of the area of a normal curve, the lowest 20%, etc. The results were not totally unreasonable but were fairly unsupportable. A sounder foundation would require a method based on looking at the total temperature distribution. Unfortunately, a frequency distribution could not be used, because each cycle of 15 or fewer observations had to be considered separately. Another way of representing the distribution was needed.

The first step toward understanding the temperature distributions consisted of rank ordering the derived exospheric temperatures in a cycle. Each temperature was assigned a position, by standard deviation, in a normal distribution. The assigned standard deviation depended on the number of observations, or processed data records, in the cycle. For example, if there were ten data records the lowest temperature would be placed in the middle of the lower ten percent of the normal curve, at -1.645 standard deviations. The data were then plotted on a graph where the X-axis was plus or minus standard deviation, with zero in the middle, and the Y-axis was temperature. The premise was that if the temperatures were from a normal distribution, they would fall in a straight line on the graph. Often the curves assumed an S-shape (Figure 4.2a), clearly indicating two or three different

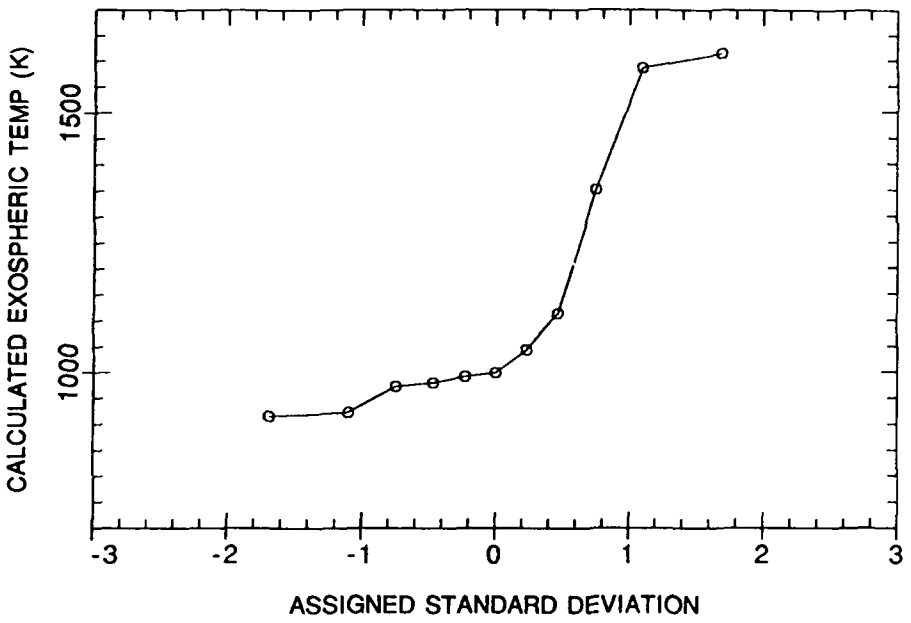

(a)

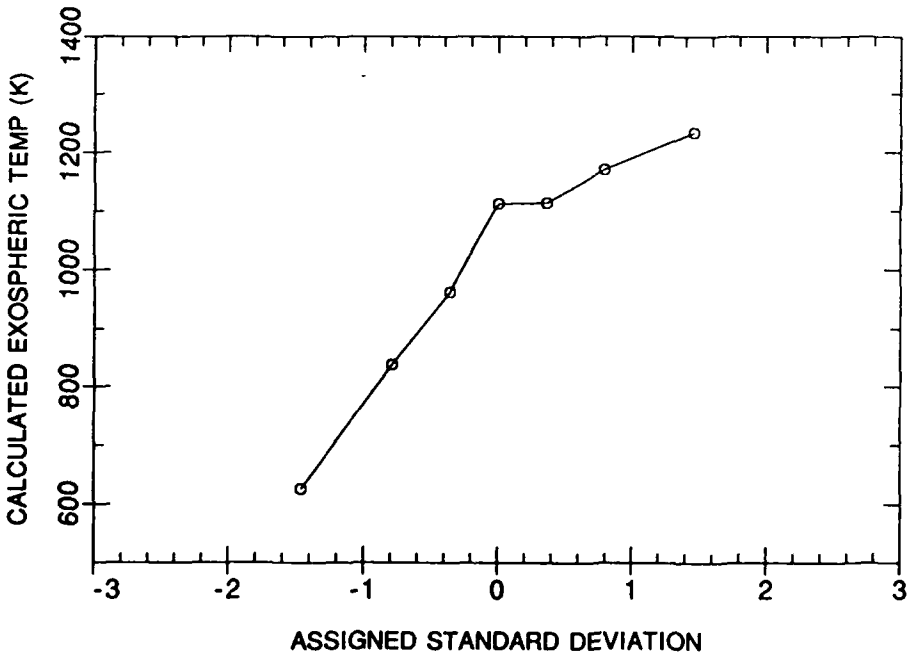

(b)

Fig. 4.2. Temperatures in one observation cycle vs assigned standard deviation.

populations (high, low, and a gradient area). But sometimes the distinction was unclear, and occasionally the temperatures would fall in almost a straight line (indicating a normal distribution), but with a range of several hundreds of degrees, an unreasonable range to expect (Figure 4.2b). Instrumental error alone would produce temperature differences of less than 100° K (usually less than 50° K), and result in a much flatter line. Clearly, a simple test of normality was not enough without considering other parameters by which to assign temperatures to specific populations.

The information available from a cycle of data were the calculated temperatures, the uncertainties (standard deviations) of each temperature, weighted means, and weighted errors of the means. Weighted means and errors were calculated using the equations [c.f., for example, Bevington, 1969]

$$\mu = \frac{\Sigma(x_i/\sigma_i^2)}{\Sigma(1/\sigma_i^2)} \qquad (4.1.1)$$

$$\sigma_\mu = \frac{1}{[\Sigma(1/\sigma_i^2)]^{1/2}} \; . \qquad (4.1.2)$$

Because the uncertainties on the radar measurements were fairly accurately known and consistent, and those uncertainties were reflected in the uncertainties on the calculated neutral temperatures, it was decided to represent the population standard deviation by

$$\sigma = \frac{N^{1/2}}{[\Sigma(1/\sigma_i^2)]^{1/2}} \; . \qquad (4.1.3)$$

which is biased somewhat toward the lower uncertainty values, but allowed for uncertainty added to the derived neutral temperatures by TOSS4 in its fitting routine.

Three statistical approaches were used: the Student *t* test, to examine the distribution of means and using the errors of the means; a test for normal distribution, using the population standard deviation; and the chi-squared test, also using the population standard deviation. All three tests were worked from the bottom up, to include the lowest temperature and decide when the next higher temperature no longer belonged to the same population. The tests were performed at the 90% confidence level, that is, with α=10% for a two-tail test. α is the probability of making a Type I error, that is, excluding a point that should be included. As α increases, β, the probability of including a point that should be excluded, decreases and the power of the test increases. Since it was decided early on that it was better to err on the side of underestimating the temperatures rather than overestimating them, α was chosen at a reasonably high level.

A fourth test, the range test, was explored and will be briefly described.

4.2 The Student *t* Test for Distribution of Means

The Central Limit Theorem states that if a population is normal, the sampling distribution of means is also normal for samples of all sizes. If the population standard deviation σ is known, the error of the mean is equal to $\sigma/(N)^{1/2}$. If the population standard deviation is not known, it can be estimated from the sample provided the sample size is large. However, if the population σ is unknown and the sample size is small, the appropriate distribution of sample means

is the *t* distribution, which approaches a normal distribution for large sample sizes. This test, then, used a sample-oriented approach to the distribution problem.

The *t* statistic is $$t = \frac{\bar{x} - \mu}{\frac{s}{(N)^{1/2}}} \quad . \tag{4.2.1}$$

In the calculations with the radar data, the denominator was replaced by the weighted error of the mean and the population mean by the weighted mean, given by Eqns. (4.1.1) and (4.1.2). So the actual equation used was

$$t = \frac{\bar{x} - \frac{\Sigma(x_i/\sigma_i^2)}{\Sigma(1/\sigma_i^2)}}{1/\Sigma(1/\sigma_i^2)} \quad . \tag{4.2.2}$$

The test was performed at the 90% confidence level for a two-tail test, that is, the extreme 5% of the area in each tail of the distribution was excluded. However, the method actually only considered the lower 5%, since it proceeded from the bottom up. Degrees of freedom used were the ones related to the error of the mean, that is, the number of samples that went into estimating the population variance. In the *t*-test, the number of degrees of freedom is N-1.

The method proceeded as follows:

(1) The temperatures in a cycle were sorted into a data array from low to high.

(2) The weighted mean of the two lowest temperatures was calculated. This first mean was assumed to be a valid mean in the distribution of sample means, and replaced $\bar{x}$ in Eqn. (4.2.2) for all comparisons.

(3) The weighted mean of the three lowest temperatures was calculated

along with the error of the mean. The question was then asked, "Could this mean be a valid population mean?" The *t* statistic was computed comparing this mean to the first mean, with 2 degrees of freedom in this case. If the first sample mean fell within the *t* distribution using this population mean, the test went on to the next candidate for a population mean, the mean of the first four temperatures, and so on. Degrees of freedom increased each time and the corresponding limiting *t* values decreased.

(4) When a population mean was reached that no longer included the first sample mean in its *t* distribution, the previous population mean was tentatively accepted. Note: this was not a comparison of two sample means. The cumulative mean decided on would be considered the mean of that population.

It was at this point that the question of range became significant. What temperature range in the distribution would be acceptable? A number value would be hard to pin down, but perhaps the spread by standard deviations would be appropriate. The expected separation in a normal distribution of 10 data points is about 3.3 standard deviations (s) from high to low, and about 2.6 s with five data points. Without knowing the population standard deviation, the range problem was handled by summing the standardized distances from each point to the point above it, using each point's own standard deviation (error bar) as the yardstick. For example, $d_1=(x_2-x_1)/s_1$. A criterion was set at 3 standard deviations for total separation. The method then proceeded.

(5) Once a mean was established that satisfied the *t* test, the summed standardized distances were checked. If the sum was greater than 3, the population mean dropped to the one previous, until the separation criterion was met. If this

process backtracked to the first mean and the separation between the first two points was greater than 3 s, the first mean was kept but flagged with a cautionary message. The matter was then decided subjectively but conservatively.

(6) If only one data point was available, it was used as a mean temperature. This decision may seem rather intemperate, but an effort was made to throw out as little data as possible, and it did provide some interesting results.

(7) If only two data points were available, their mean was used as the mean temperature provided their separation was not too great (usually the subjective criteria were about 3.5 s or less and a range of 300 degrees or less). If so, the first temperature was used as the mean. Again, such an inclusionary policy would probably not be suited to selection of temperatures as input to a data base, since there is no way to determine just where in the assumed normal distribution these two values came from. But for examination of overall trends, the "ones and twos" did provide some useful information.

In summary, the *t* test compared the lowest sample mean temperature to proposed population means and stopped at the highest population mean possible, within a certain range limit. Since, in reality, the population mean was estimated from a very small sample size, the *t* distribution was assumed for the distribution of the means. The test was often more conservative than a straight test for normal distribution, probably because the error of the mean is much less than the population standard deviation would be. But sometimes it was less conservative, especially if the first mean was weighted far above the lowest temperature.

4.3 The Normal Distribution Test

A normal distribution test assumes you know what the population mean and standard deviation are, and are trying to determine if a certain sample is from that distribution. We can accept our calculated weighted mean as the population mean, since that is how it will be used. The question of debate was what to use for the population standard deviation. As mentioned earlier, the standard deviations on the quantities measured by the radar are well known and usually very consistent with each other (i.e., at least for a given cycle or time period). So it seemed reasonable that the population standard deviation should be fairly represented by some average of the standard deviations of all the data points in a cycle, regardless of which population we later decided they belonged to. That is, since the radar uncertainties are basically instrumental in nature, all data points could be used to arrive at a population uncertainty, regardless of the actual values of those data points. The effect of the fitting routine on the data standard deviations, if any, would be to increase the uncertainty. However, this effect was somewhat compensated for by the weighting involved in the calculation.

In calculating the variance of the mean of values that in turn have variances the equation is

$$\sigma_\mu^2 = \frac{1}{\Sigma(1/\sigma_i^2)} \quad . \tag{4.3.1}$$

If all data points have the same variance, then Eqn. (4.3.1) reduces to

$$\sigma_\mu^2 = \frac{\sigma^2}{N} \qquad \text{or} \qquad N\sigma_\mu^2 = \sigma^2 \quad . \tag{4.3.2}$$

So the population variance is related to the variance of the mean by a factor of N. If the sample variances are not equal, then Eqn. (4.3.1) can be equated to Eqn. (4.3.2), taking σ^2 to represent the population variance:

$$\sigma^2 = N\sigma_\mu^2 = \frac{N}{\Sigma(1/\sigma_i^2)} \quad , \tag{4.3.3}$$

and the population standard deviation can be calculated by

$$\sigma = \frac{N^{1/2}}{[\Sigma(1/\sigma_i^2)]^{1/2}} \quad . \tag{4.3.4}$$

In both the normal distribution test and the chi-squared test, the population standard deviation was calculated in this way, using the uncertainties on all available data points in the cycle.

The normal distribution test now becomes very straightforward. α was set at 10%. The distance from the population mean to the upper or lower 5% of the normal curve is plus or minus 1.645 standard deviations. If our extreme data points fall within this distance from the mean, they belong to the distribution. The range problem has been solved by specifying a population standard deviation. The method proceeded as follows:

(1) The population standard deviation σ was calculated, using all data points. This value did not vary.

(2) The first weighted mean was calculated, using the two lowest temperatures. The two values were tested to see if they fell within $\pm$ 1.645σ of the mean. If the test failed at this point, the lowest temperature was kept as the mean.

(3) If the first test did not fail, the weighted mean of the first three

temperatures was calculated, and the lowest and highest temperatures were tested for membership in the distribution. The test continued until it failed to include either temperature. Then, the mean previous to the one that failed was retained as the population mean, with its calculated error of the mean.

(4) As with the *t* test, means represented by only one data point were kept for further evaluation.

The normal distribution test assumes not only that the population standard deviation is known, but that even a small sample is normally distributed. One might expect these assumptions to limit the selection of temperatures more than the *t* test, but, as will be discussed in the Results chapter, this test sometimes included more and sometimes fewer points than the *t* test.

4.4 The Chi-Squared Test

A common use of the chi-squared test is as a test of goodness of fit, that is, a means of deciding if a sample distribution is close enough to a theoretical population distribution to consider the distributions the same. As with the previous test, we assume the temperature distribution to be normal with a known population standard deviation. The population means are calculated as before, as cumulative weighted means. Then, all data points that went into the means are tested for total amount of deviation from the mean.

The chi-squared statistic is

$$\chi^2 = \frac{\Sigma(x_i-\mu)^2}{\sigma^2} \quad . \qquad (4.4.1)$$

The table for the chi-squared distribution requires the number of degrees of freedom. Since the sample values were used to estimate the population mean, that reduces the degrees of freedom to N-1. Normally, if the sample variances are used to estimate the population variance, degrees of freedom are reduced once more, to N-2. However, since our claim is that the population variance is actually independent of our sample (even though we calculate it from the sample), the test was made with N-1 degrees of freedom. The procedure, then, was:

(1) The population variance was calculated, using all data points.

(2) The first weighted mean and the chi-squared statistic were calculated. Degree of freedom here is 1. The value was checked against the chi-squared table. If the test failed, the lowest temperature was retained as the mean.

(3) The test was continued for the cumulative means until it failed. Then the next mean back was retained as the population mean, along with the calculated error of the mean.

The chi-squared test proved to be more lenient than the other two tests, that is, it often allowed more data points to be included in the distribution than the *t* test, and sometimes more than the normal distribution test. But, as with the normal test, it was sometimes more severe than the *t* test when examining the deviation of the first two temperatures.

4.5 The Range Test

The range test is a quick and dirty way of determining if sample values came from the same normal distribution based on the standardized distance between the two extreme values. If the population standard deviation is known, the range

statistic is $$W = \frac{x_n - x_1}{\sigma} \quad . \qquad (4.5.1)$$

The range test was run on two days of data, with α=10%, and working from the top down until the two extremes were within an acceptable range of each other. In general, this test included the most data points per cycle, equal to or greater than the chi-squared test. The leniency of the test is obviously based on the fact that the population mean is not used, only the probable spread of the points. The result, though, is a contradiction of the assumed distribution. If the weighted mean based on the points selected by the range test is used as the population mean, the points involved often no longer fall in a normal distribution about that mean. The range test was abandoned as not using enough of the known information.

CHAPTER V

RESULTS

5.1 Results for Individual Days

Ten days were used in the study - four from 1983, three from 1987, and three from 1988. 1986 was solar cycle minimum and 1990 solar cycle maximum. The day with the highest average F10.7 cm flux was September 9, 1983 (120.8), and the lowest occurred during January 27-29, 1987 (70.4). The highest previous day F10.7 cm flux occurred on October 8, 1983 (133.9), the lowest on January 28, 1987 (69.9). The Ap index ranged from 4 (March 19, 1988) to 28 (December 6, 1983). Results will be discussed for each day separately, then summarized for each statistical method. Since the data days go from one UT day to the next, magnetic activity and solar flux values will be listed for both days, to include the Ap index, the 81-day average F10.7 cm flux value (F10.7A), and the previous day's F10.7 cm flux value (F10.7P).

Daily plots initially discussed will depict three-point running weighted averages of the exospheric temperatures calculated from the radar data, one-hour weighted averages of the Fabry-Perot neutral temperatures, and MSIS86 model exospheric temperatures. Fabry-Perot temperatures are assumed to be from lower altitudes (225 km average) and are expected to be lower than the exospheric temperatures. Daily tables list the mean times for each observation cycle, the number of processed data records (available observations) per cycle (listed under 'N'), and the number of temperatures selected by each test as belonging to the same non-Joule-heated distribution.

5.1.1 September 9-10, 1983

Ap = 16/12 F10.7A = 120.8/120.2 F10.7P = 118.5/115.3

September 9-10 data included both fixed position scans (11 position) and elevation scans (15 position), giving two independent measures of temperatures during roughly the same time periods. Radar data were available from about 2300 UT on the 9th to about 2300 UT on the 10th. Averaged Fabry-Perot data covered the period of 0100-0600 UT on the 10th.

Tables 5.1 and 5.2 list the number of data records available for each cycle (N) and the number of temperatures selected by each statistical test. For the fixed position data, the *t* test often used more temperatures than the other two tests. For the elevation scan data, this pattern was reversed. The column listing the number of data records available shows a typical pattern that emerged in processing the data records. There were usually fewer data records accepted by the program during the midnight to morning times than during daylight or evening hours. One reason is probably the weaker signal (and therefore poorer data) obtained in the midnight sector because of low electron and ion densities. Another contributing factor is that there may be more Joule heating happening in this area, again related to the lower ion densities, leading to rejection of more records for violating the ion temperature criterion.

Figures 5.1 and 5.2 show the temperature results. The *t*-test temperatures for both scan types agreed fairly well with each other compared to the results of the other tests. I believe most of the discrepancies seen on this day are due to the nature of the statistical tests rather than significant physical processes, although the peak around 1500 UT on the 10th, enhanced in the elevation scan data, may be

Table 5.1. Number of Temperatures Used per Cycle
Sept. 9-10, 1983 (11 Pos)

Time	N	Stu t	Norm	Chi-Sq
23.00	11	4	1	1
23.48	11	4	1	1
23.94	11	3	3	3
24.39	10	4	5	5
24.83	10	2	2	2
25.28	11	5	5	5
25.73	10	2	2	2
26.20	8	5	1	1
26.69	5	2	1	1
27.08	2	1	1	1
27.54	2	2	2	2
28.02	1	1	1	1
28.41	3	3	3	3
28.82	2	2	2	2
29.35	5	3	2	1
29.77	2	1	1	1
30.25	4	2	2	2
30.69	3	2	2	1
31.12	3	2	2	2
31.57	2	1	1	1
32.06	8	2	1	1
32.53	6	4	4	5
32.93	5	2	2	2
33.41	10	4	3	4
33.86	10	3	3	5
34.30	11	4	4	4
35.83	10	3	3	3
36.26	11	4	6	6
36.71	11	4	4	6
37.20	11	4	2	1
37.66	10	5	3	5
38.09	11	3	4	4
38.55	11	3	1	1
38.99	11	3	3	3
39.44	11	2	2	1
39.89	11	2	1	1
40.34	11	4	2	4
40.78	11	2	2	2
41.24	11	4	3	5
41.68	11	3	3	3
42.13	11	4	3	4
42.58	11	3	3	4
43.03	11	6	6	9
43.48	11	2	1	1
43.93	11	5	7	8
44.39	10	6	9	9
44.83	11	5	7	8
45.27	11	4	3	4
45.73	11	4	4	5
46.17	11	3	1	1
46.62	11	3	2	3
46.99	4	2	1	1

Table 5.2. Number of Temperatures Used per Cycle Sept. 9-10, 1983 (El Scan)

Time	N	Stu t	Norm	Chi-Sq
23.18	15	3	1	1
23.66	15	4	8	13
24.12	15	4	3	4
24.56	15	6	7	14
25.02	15	6	7	10
25.46	14	6	7	10
25.91	11	4	7	7
26.39	11	3	3	9
26.83	5	4	4	5
27.27	1	1	1	1
28.20	4	4	4	4
28.65	1	1	1	1
29.10	4	4	4	4
29.55	4	3	1	1
29.99	9	3	5	9
30.44	9	5	5	7
30.89	6	3	3	4
31.35	7	4	4	4
31.80	6	3	4	5
32.25	7	5	4	5
32.69	12	3	2	6
33.13	13	4	4	4
33.58	14	3	3	4
34.03	15	4	7	9
34.48	15	4	3	4
36.00	15	6	11	13
36.44	15	5	5	12
36.90	15	10	15	15
37.38	15	8	14	15
37.83	15	5	6	10
38.27	15	3	2	2
38.73	15	2	1	1
39.17	15	8	10	14
39.62	15	3	3	3
40.07	15	6	8	11
40.52	15	3	2	2
40.97	15	4	5	6
41.42	15	7	14	15
41.86	15	2	1	1
42.31	15	4	4	7
42.76	15	4	7	7
43.21	15	6	9	15
43.66	15	3	1	1
44.11	15	5	4	14
44.56	15	4	4	7
45.01	14	5	7	14
45.46	15	3	2	2
45.91	15	4	3	4
46.35	15	4	2	3
46.80	15	5	8	8

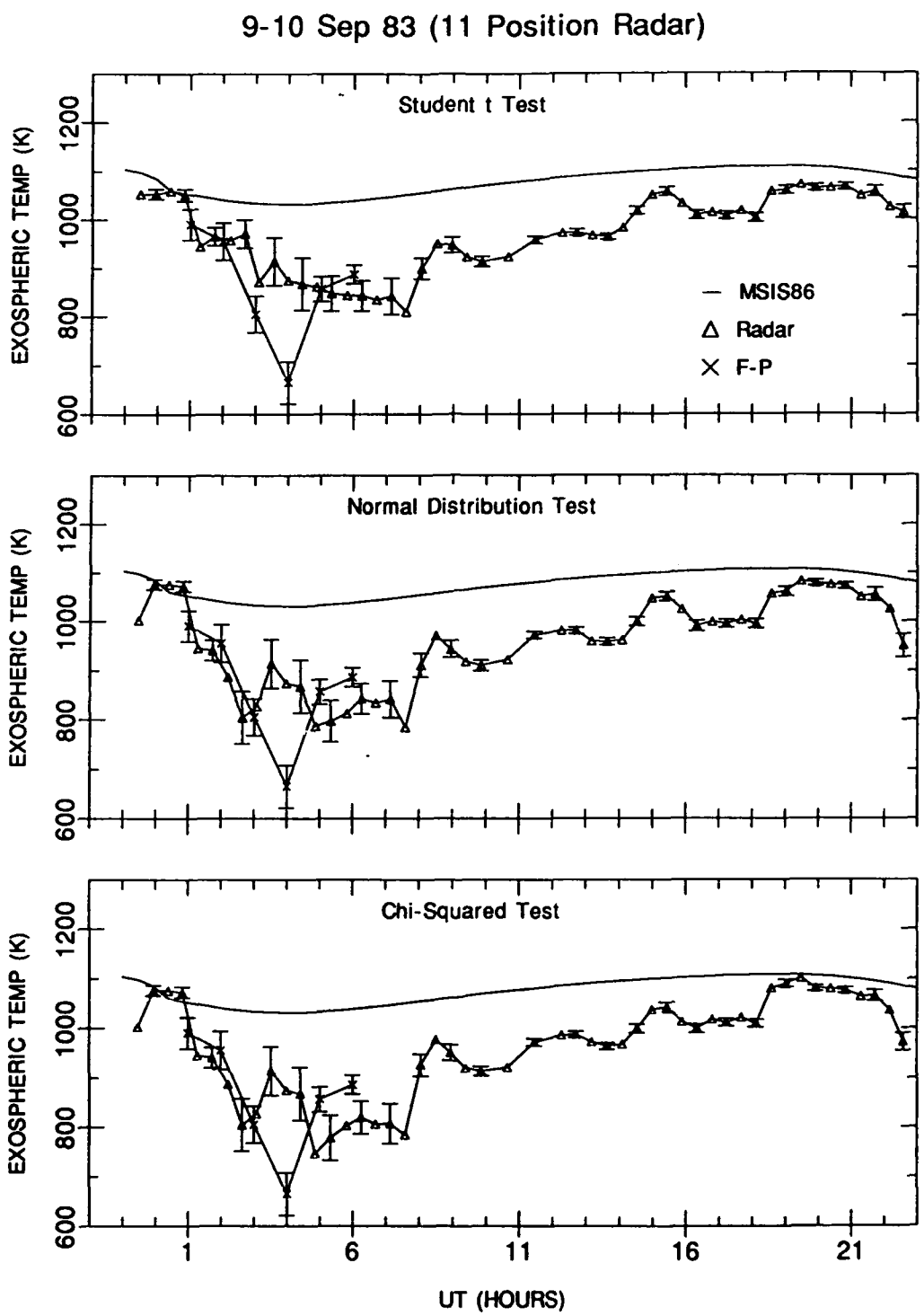

Fig. 5.1. Averaged exospheric temperatures and Fabry-Perot temperatures, September 9-10, 1983 (11 position).

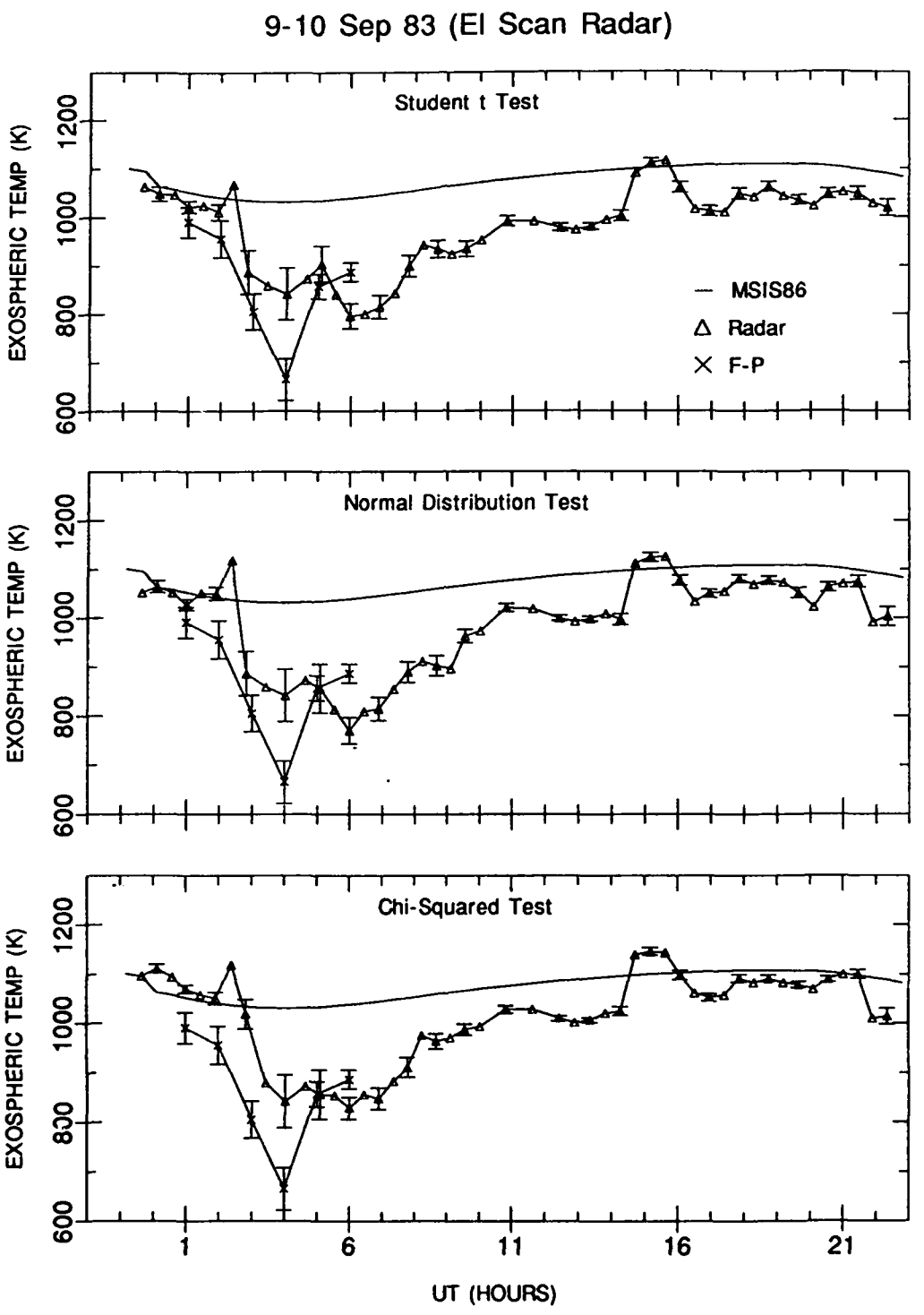

Fig. 5.2. Averaged exospheric temperatures and Fabry-Perot temperatures, September 9-10, 1983 (elevation scan).

indicative of a large-scale, low-intensity Joule heating area. An interesting feature is the sharp drop in the Fabry-Perot temperatures around 0400 UT, at least 150 degrees below the radar temperatures. This could have been caused by a particle precipitation event lowering the emission layer. The overall pattern of the radar temperatures shows a significant difference from MSIS predicted temperatures: about 250 degrees in the 0300-0700 UT period and 100 to 150 degrees much of the rest of the time. Fabry-Perot temperatures are usually below the radar temperatures, as they should be, except in the normal distribution and chi-squared plots for the fixed position scans.

5.1.2 September 13-14, 1983

Ap = 7/6 F10.7A = 118.1/117.5 F10.7P = 104.9/104.4

This day also included both fixed position scans and elevation scans. Radar data ran from 2300 UT on the 13th to 2300 UT on the 14th. Fabry-Perot temperatures covered the period of 0000-0600 UT on the 14th. Tables 5.3 and 5.4 list the selection data, and Figures 5.3 and 5.4 show the temperature data.

This day had fairly good agreement between the elevation scan and the fixed position scan temperatures, the best agreement being for the *t*-test results. The Fabry-Perot temperatures were generally below the radar temperatures. Similar to September 9-10, there is a drop in the Fabry-Perot temperature around 0400 UT, and there is a small peak in the radar temperatures around 1600 UT. Departures of radar temperatures from MSIS temperatures are not as great as in the previous example, but follow the same diurnal pattern, with a minimum around 0500-0600 UT, 100-150 degrees below MSIS.

Table 5.3. Number of Temperatures Used per Cycle
Sept. 13-14, 1983 (11 Pos)

Time	N	Stu t	Norm	Chi-Sq
22.89	11	4	2	2
23.33	11	2	1	1
23.78	11	3	2	1
24.23	11	2	2	1
25.99	10	3	3	3
26.45	10	4	1	1
26.88	9	5	5	5
27.33	9	4	7	9
27.79	10	4	6	6
28.24	11	4	2	2
28.66	8	4	4	4
29.12	6	4	6	6
29.54	6	4	1	1
30.03	5	4	1	1
30.44	5	5	3	5
30.94	5	5	5	5
31.43	6	6	6	6
31.86	6	4	2	2
32.31	6	3	3	3
32.75	8	4	5	4
33.17	7	6	6	6
33.59	8	4	4	4
34.07	11	4	6	6
34.52	11	5	3	7
34.97	11	3	2	1
35.52	11	5	6	6
36.28	11	3	4	2
36.72	10	6	9	9
37.18	11	4	4	2
37.67	11	4	2	2
38.15	11	6	6	7
38.61	10	5	3	3
39.10	11	2	2	1
39.51	10	2	2	2
39.99	11	2	2	2
40.44	11	3	2	2
40.89	11	4	5	5
41.34	11	3	2	2
41.86	11	4	4	5
42.32	9	4	4	4
42.80	11	4	5	7
43.24	10	2	1	1
43.69	11	2	2	2
44.14	11	4	3	4
44.59	11	3	3	3
45.05	11	5	5	6
45.54	11	3	3	2
45.99	11	3	3	3
46.44	11	3	2	2
46.80	8	3	2	2

Table 5.4. Number of Temperatures Used per Cycle Sept. 13-14, 1983 (El Scan)

Time	N	Stu t	Norm	Chi-Sq
23.07	15	2	1	2
23.51	15	6	13	1
23.96	14	6	12	1
26.19	15	5	9	1
26.63	13	4	6	3
27.09	11	8	9	1
27.53	12	6	9	5
27.98	14	6	10	9
28.43	13	6	8	6
28.88	13	5	5	2
29.33	12	7	6	4
29.78	5	4	4	6
30.23	12	5	5	1
30.67	7	5	6	1
31.12	11	4	4	5
31.56	13	5	8	5
32.01	11	5	3	6
32.46	14	5	7	2
32.91	15	6	9	3
33.36	15	7	12	4
33.80	15	6	6	6
34.25	14	5	6	4
34.70	15	4	10	6
35.15	15	6	12	7
35.93	10	7	2	1
36.38	15	6	10	6
36.82	15	4	4	2
37.27	15	5	1	9
37.76	15	5	9	2
38.21	15	4	2	2
38.66	15	3	2	7
39.16	15	4	4	3
39.60	15	5	5	1
40.06	15	4	5	2
40.49	15	5	6	2
40.95	15	5	5	2
41.39	15	5	9	5
41.96	15	5	5	2
42.41	14	4	1	5
42.86	15	6	6	4
43.30	14	5	1	7
43.76	15	5	8	1
44.20	15	6	7	2
44.65	15	5	5	4
45.14	15	9	12	3
45.60	15	7	7	6
46.04	15	5	1	2
46.49	15	5	4	3
46.94	15	6	1	2

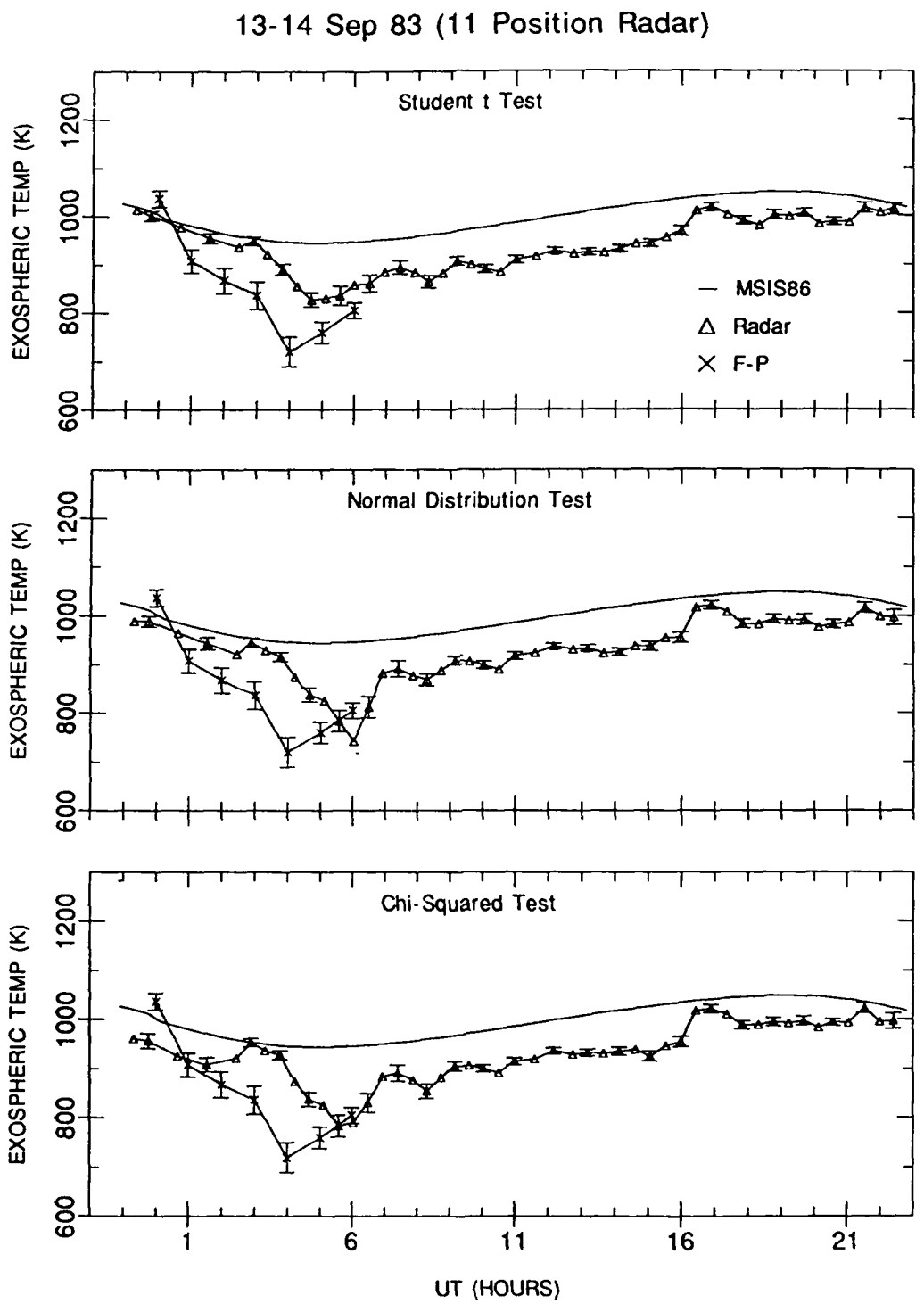

Fig. 5.3. Averaged exospheric temperatures and Fabry-Perot temperatures, September 13-14, 1983 (11 position).

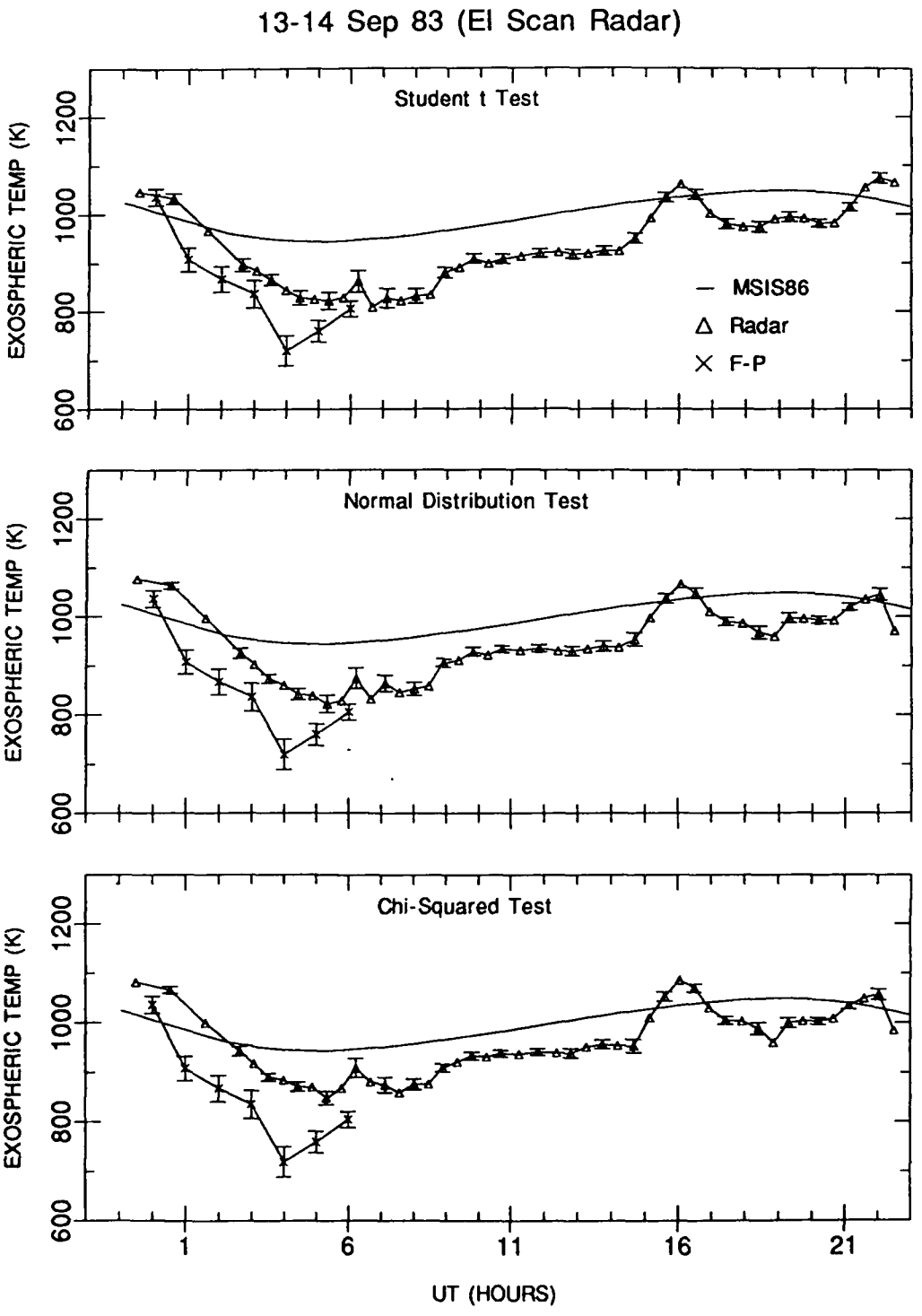

Fig. 5.4 Averaged exospheric temperatures and Fabry-Perot temperatures, September 13-14, 1983 (elevation scan).

5.1.3 October 8-9, 1983

Ap = 16/5 F10.7A = 107.9/107.6 F10.7P = 133.9/133.1

This is a difficult day to explain. There are large discrepancies between the Fabry-Perot temperatures and the radar temperatures (see Figure 5.5). The three-point peak in the radar temperatures, centered around 0400 UT, is most heavily influenced by one spike in the radar temperatures at that time and additionally by a fairly high temperature in the cycle after that, at times 28.04 (4.04 UT) and 28.55 (4.55 UT) in Table 5.5. These two cycles had eight and seven available observations, respectively, and a large number of the temperatures were selected by the statistical tests. Looking at Figure 5.5, it appears the radar temperatures are heading for their regular nightly minimum when interrupted by these peaks. I can only conclude that either the radar just did not catch the non-Joule-heated areas or there is in fact a significant large-scale Joule heating event in this region. The pre-0300 UT radar temperatures follow a pattern similar to the September, 1983 temperatures and are derived from complete observation scans, so they seem to be real. The 0100 UT low in the Fabry-Perot temperatures could be related to particle precipitation. Without further data, it's impossible to determine exactly what is going on.

Minimum derived radar temperatures fall about 175-200 degrees below MSIS values around 0300 UT and 0500 UT, similar to the differences in September, 1983.

5.1.4 December 5-6, 1983

Ap = 16/28 F10.7A = 91.1/91.2 F10.7P = 91.9/92.0

Although the original data extended slightly into December 6, the averaged

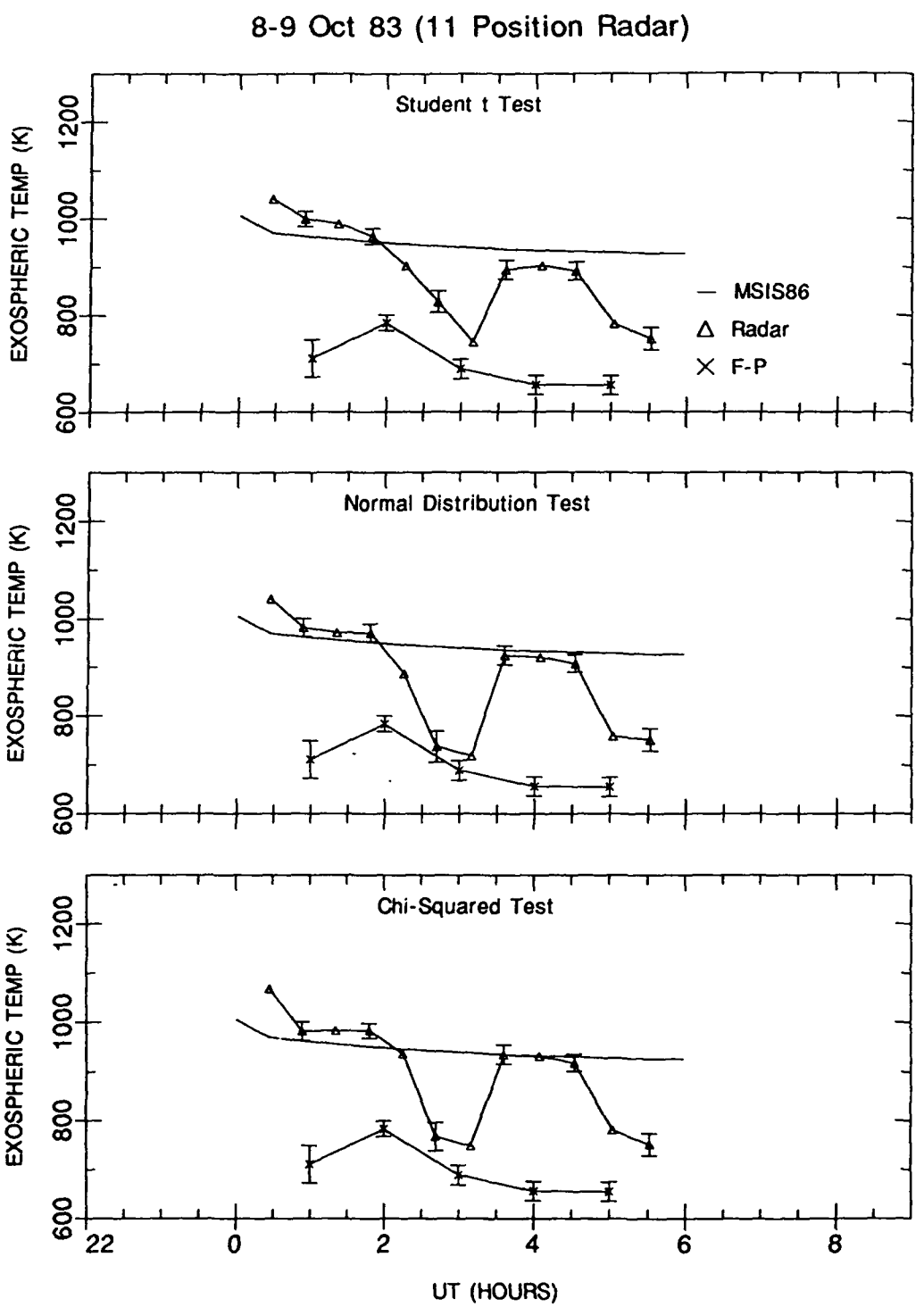

Fig. 5.5. Averaged exospheric temperatures and Fabry-Perot temperatures, October 8-9, 1983.

Table 5.5. Number of Temperatures Used per Cycle
Oct. 8-9, 1983

Time	N	Stu t	Norm	Chi-Sq
24.02	8	4	4	7
24.45	11	4	3	3
24.90	11	2	1	1
25.35	11	3	3	3
25.80	11	3	3	6
26.25	4	3	1	1
26.73	7	4	5	6
27.12	7	3	2	2
27.64	6	2	1	1
28.04	8	4	5	6
28.55	7	5	4	5
29.03	3	3	3	3
29.58	3	2	2	2
29.97	6	5	5	5

data for this day ended just before 2400 UT on the 5th. The radar-derived temperatures (Figure 5.6) follow the same pattern seen previously, starting above the MSIS curve (but this time 100 degrees above) and falling below MSIS at a progressively earlier time since September, 1983. Fabry-Perot temperatures are quite high on this day and almost always above the radar temperatures, for which I have no explanation. Number of data records per cycle and selection numbers are listed in Table 5.6.

Table 5.6. Number of Temperatures Used per Cycle
Dec. 5-6, 1983

Time	N	Stu t	Norm	Chi-Sq
20.48	6	3	1	1
20.91	8	2	2	1
21.36	9	6	7	8
21.81	11	3	5	7
22.27	7	4	4	4
22.65	2	2	1	1
23.17	7	2	2	1
23.58	4	2	2	2
24.08	5	3	3	3

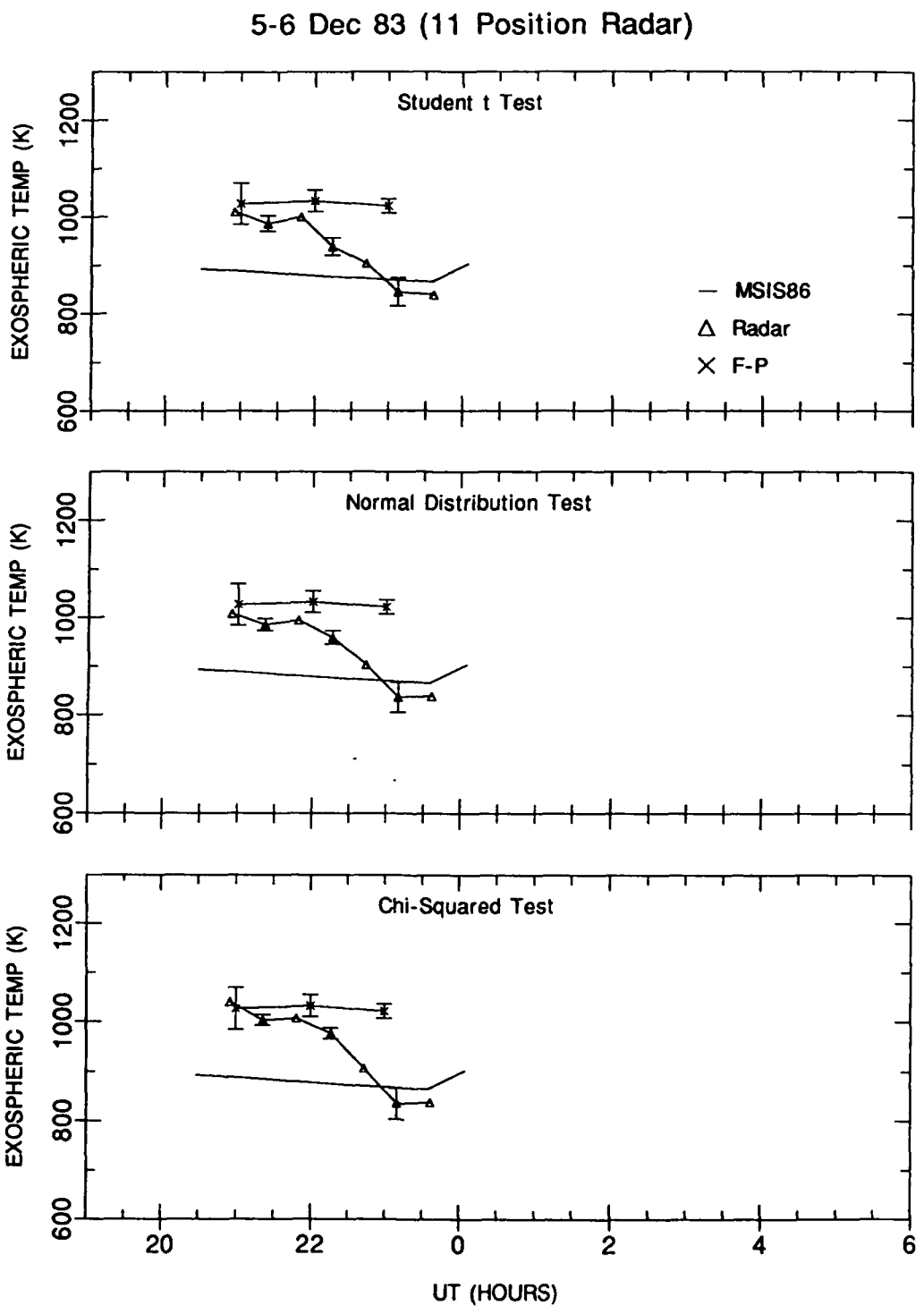

Fig. 5.6. Averaged exospheric temperatures and Fabry-Perot temperatures, December 5-6, 1983.

5.1.5 January 27-28, 1987

Ap = 7/11 F10.7A = 70.4/70.4 F10.7P = 72.6/69.9

January, 1987, after the solar cycle minimum in 1986, showed temperatures about 100 degrees cooler than the 1983 data. Radar data on January 27-28 were available from about 1100 UT on the 27th to 1000 UT on the 28th, but large data gaps in the processed data during 2100-0500 UT limited comparisons to only four Fabry-Perot temperatures (Figure 5.7). The radar temperatures tended to follow MSIS values to within about 50 degrees, although the post-midnight period cannot be analyzed for lack of data. The period of 0600-1000 UT reveals for the first time the risk involved in keeping the "ones and twos" as representative mean temperatures. Table 5.7 shows only one or two processed data records per cycle after 21.28 UT. The days previously discussed showed no trends or major problems with retaining this low number of available observations. And indeed, Figure 5.7 shows excellent agreement with Fabry-Perot temperatures from 0600-0800 UT. But the sharp peak in the radar temperatures after 0800 UT is so inconsistent with expected behavior that I believe the Fabry-Perot temperature to be accurate. In fact, since the Fabry-Perot temperatures are expected to be lower than the exospheric temperatures, this day may be a case of low number of observations first underestimating and then overestimating the actual neutral temperatures.

5.1.6 January 28-29, 1987

Ap = 11/10 F10.7A = 70.4/70.4 F10.7P = 69.9/70.8

This day also suffers from large data gaps between 0100 and 1000 UT on the 29th. Figure 5.8 shows all the Fabry-Perot temperatures for this day, but the

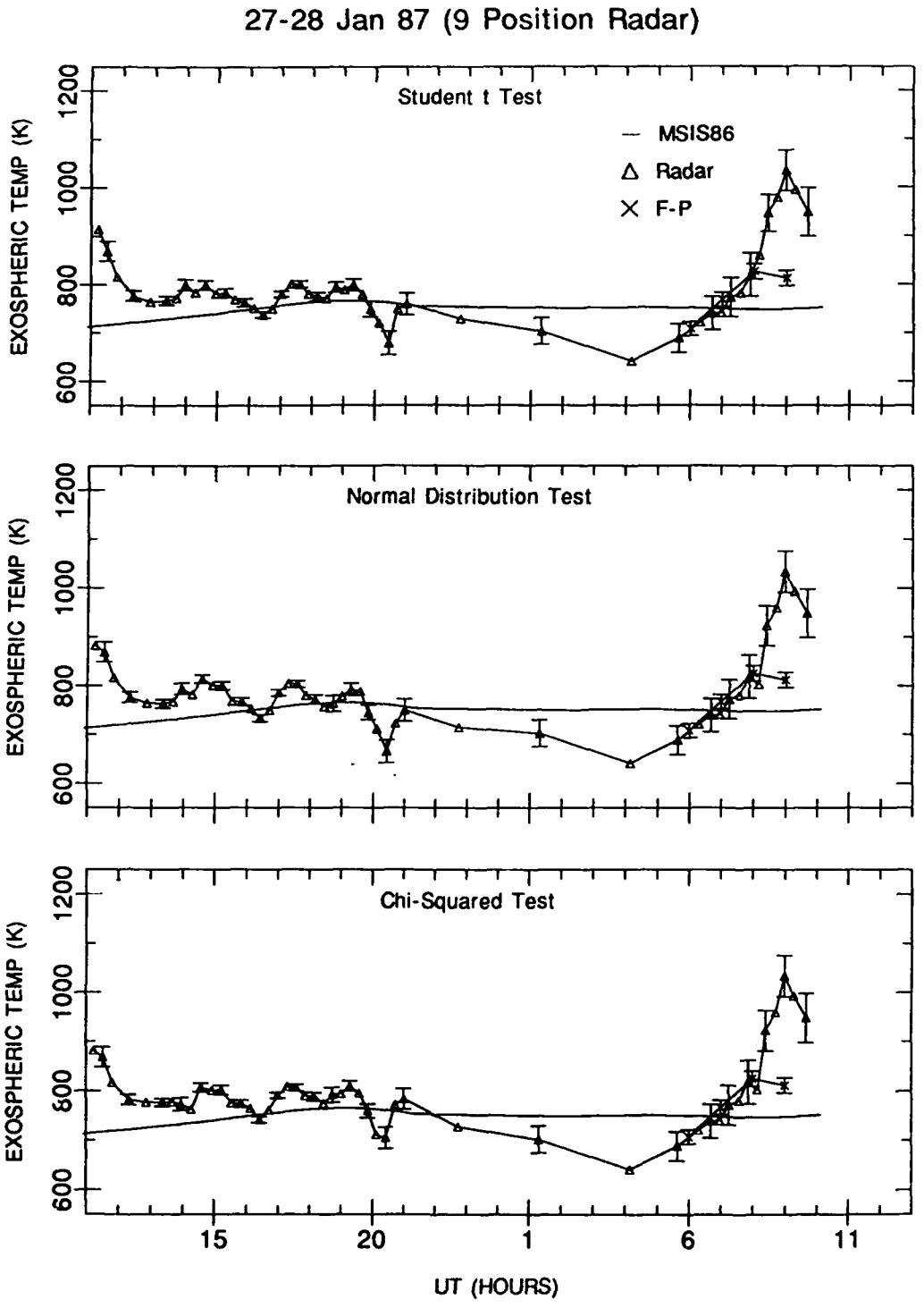

Fig. 5.7. Averaged exospheric temperatures and Fabry-Perot temperatures, January 27-28, 1987.

Table 5.7. Number of Temperatures Used per Cycle
Jan. 27-28, 1987

Time	N	Stu t	Norm	Chi-Sq
10.92	4	2	1	1
11.21	3	1	1	1
11.54	2	2	2	2
11.82	5	4	4	4
12.11	6	4	4	4
13.09	8	4	4	5
13.38	8	5	5	6
13.68	7	2	1	1
13.98	7	3	3	3
14.19	4	2	2	1
14.64	8	2	1	1
14.93	9	4	6	6
15.25	7	2	1	1
15.53	8	2	2	1
15.84	8	5	7	8
16.14	8	3	3	3
16.42	9	6	4	6
16.73	8	5	5	7
17.00	9	4	5	6
17.31	7	6	7	7
17.58	8	6	6	7
17.88	7	4	4	5
18.15	9	4	4	8
18.45	8	3	2	1
18.73	8	4	2	1
19.02	8	4	2	4
19.29	9	5	7	7
19.58	7	4	4	5
19.87	6	6	6	6
20.14	7	3	4	4
20.42	5	2	1	1
20.73	5	4	4	5
21.01	6	5	4	5
21.28	6	2	2	2
25.97	1	1	1	1
28.68	2	2	2	2
29.83	1	1	1	1
30.40	1	1	1	1
30.70	1	1	1	1
30.97	2	1	1	1
31.22	1	1	1	1
31.55	1	1	1	1
31.92	1	1	1	1
32.10	1	1	1	1
32.43	2	2	1	1
32.72	2	2	2	2
32.98	1	1	1	1
33.27	1	1	1	1
33.60	1	1	1	1
34.13	1	1	1	1

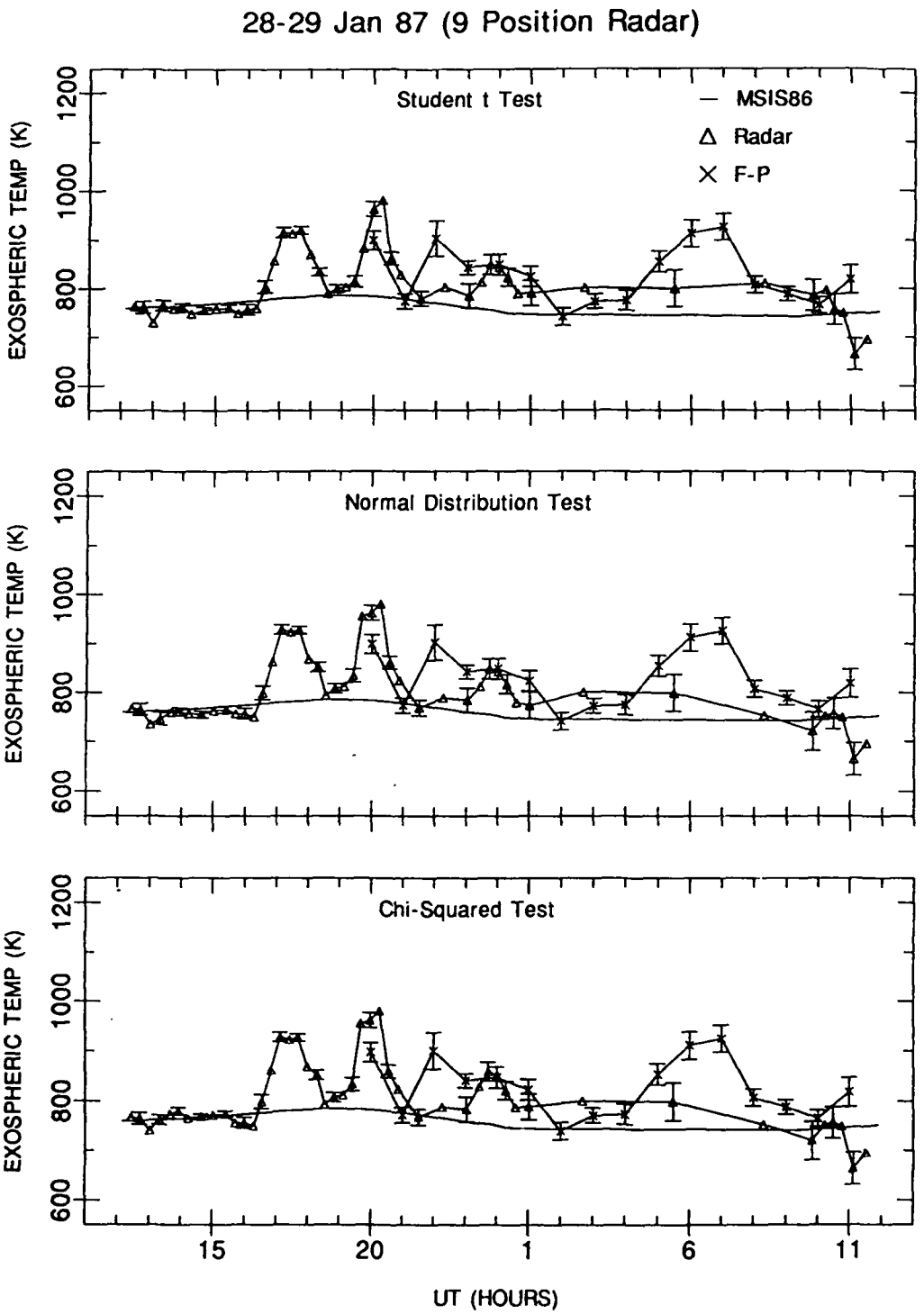

Fig. 5.8. Averaged exospheric temperatures and Fabry-Perot temperatures, January 28-29, 1987.

data from 0200-0900 UT were not used for comparison because of the radar data gaps. The temperature profiles for this day show several areas of significant Joule heating which have apparently affected the neutral temperature in a real way, not as an artifact of the program. The peak around 1730 UT is based on full sets of observations (see Table 5.8), and the one around 2000 UT is at least half matched by Fabry-Perot observations. The Fabry-Perot peak at 2200 UT is partially followed by the radar temperatures, but there is an hour and a half gap in the radar data which may be masking this fluctuation. The Fabry-Perot peak at 0700 UT again seems to be real, indicating a very active and interesting night for large-scale Joule heating.

Outside of the peaks, the radar-derived temperatures follow MSIS values quite closely, while the Fabry-Perot temperatures fall both above and below the radar temperatures.

5.1.7 January 29-30, 1987

Ap = 10/4 F10.7A = 70.4/70.5 F10.7P = 70.8/70.6

Because of large radar data gaps on this day, only three Fabry-Perot temperatures could be used for comparison, as shown in Figure 5.9. All three statistical tests produced very similar results (Table 5.9). The radar-derived temperatures are within 50 degrees of MSIS values and show no significant fluctuations.

5.1.8 March 16-17, 1988

Ap = 14/9 F10.7A = 114.5/114.5 F10.7P = 112.6/114.1

The March, 1988 radar scans included two extra observations looking up the

Table 5.8. Number of Temperatures Used per Cycle
Jan. 28-29, 1987

Time	N	Stu t	Norm	Chi-Sq
12.15	6	4	4	4
12.43	6	6	6	6
12.72	7	2	3	3
12.94	4	2	2	2
13.39	7	4	3	7
13.67	7	3	2	3
13.94	9	3	4	5
14.22	9	5	5	6
14.51	9	5	5	5
15.13	9	4	4	7
15.41	9	3	4	4
15.70	9	3	3	3
15.99	9	3	3	3
16.27	9	2	2	2
16.57	8	2	1	1
16.84	9	2	2	2
17.13	9	3	3	3
17.42	9	3	5	5
17.70	9	3	3	3
17.99	9	5	4	5
18.28	9	3	3	3
18.56	9	3	1	1
18.82	7	4	4	4
19.13	6	3	3	3
19.41	8	3	1	1
19.69	7	2	2	2
19.97	7	3	3	3
20.27	6	2	2	2
20.58	4	2	2	2
20.86	5	2	2	2
21.18	5	2	1	1
22.49	2	2	2	2
23.15	3	3	3	3
23.45	3	3	3	3
23.72	4	2	2	3
23.99	2	2	2	2
24.28	3	3	3	3
24.59	3	3	2	3
24.90	1	1	1	1
25.53	1	1	1	1
29.62	1	1	1	1
33.33	1	1	1	1
33.93	2	2	1	1
34.22	1	1	1	1
34.47	1	1	1	1
34.75	1	1	1	1
35.03	1	1	1	1
35.61	2	2	2	2
35.90	3	3	3	3

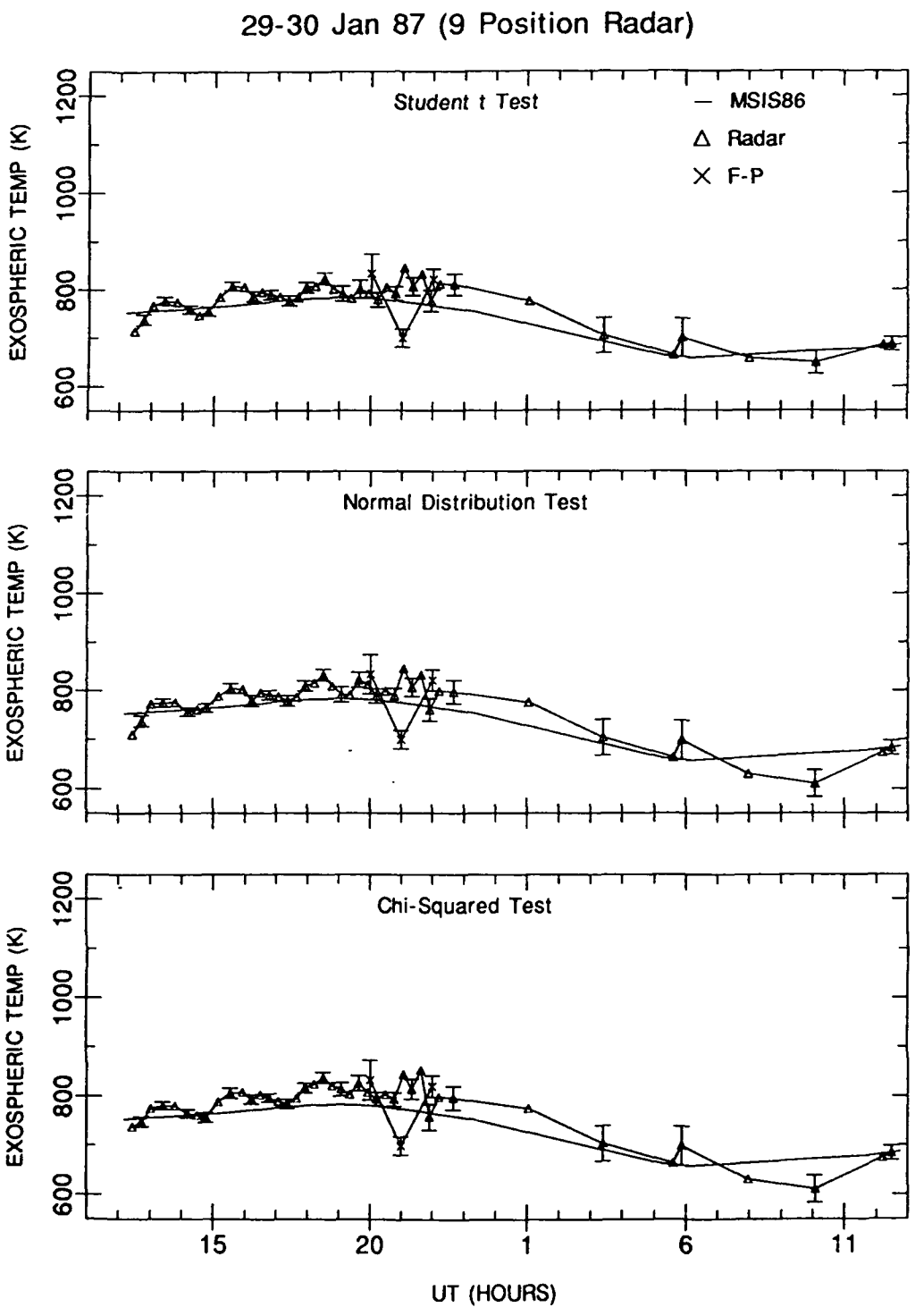

Fig. 5.9. Averaged exospheric temperatures and Fabry-Perot temperatures, January 29-30, 1987.

Table 5.9. Number of Temperatures Used per Cycle
January 29 30, 1987

Time	N	Stu t	Norm	Chi-Sq
12.18	3	3	3	3
12.45	6	3	2	2
12.72	7	4	4	6
13.02	6	6	6	6
13.31	8	5	6	6
13.90	8	5	4	5
14.20	9	5	7	7
14.48	9	3	2	2
14.77	9	5	7	7
15.06	9	3	3	1
15.63	9	7	7	8
15.92	9	3	2	1
16.20	9	4	4	5
16.50	8	4	4	5
16.77	8	5	5	5
17.06	9	4	3	6
17.35	9	4	5	5
17.64	9	4	4	4
17.92	9	5	6	7
18.21	8	4	5	5
18.49	9	5	6	7
18.78	8	3	3	5
19.06	8	3	3	4
19.36	7	6	6	7
19.64	7	3	4	3
19.90	6	3	6	6
20.21	5	4	2	3
20.49	6	4	3	5
20.77	5	4	4	4
21.06	4	3	3	3
21.35	5	4	4	4
21.62	5	2	2	1
21.91	4	3	3	3
22.21	4	4	3	3
22.49	2	2	2	2
23.30	2	2	2	2
29.32	1	1	1	1
29.60	1	1	1	1
29.88	1	1	1	1
30.17	1	1	1	1
35.93	2	2	1	1
36.20	2	2	1	1
36.49	4	4	4	4
36.77	3	3	3	3

magnetic field line, one at the beginning and one at the end of the normal 11 position cycle, for a total of 13 fixed positions per cycle. Most of the data records were accepted by the program, even during the early morning hours, so the derived temperatures should be fairly reliable. March 16-17 radar data was available from about 1300 UT on the 16th to 1200 UT on the 17th. Fabry-Perot average temperatures ran from 2300-0800 UT.

The March 16-17 temperatures (Figure 5.10) stay about 50 to 100 degrees above MSIS values throughout the time period. The temperature drop around 0400 UT and the rise after that are based on several observations, so appear to be real. The corresponding peak in the Fabry-Perot temperatures around 0500 UT, although not quite matched by the radar temperatures, also appears to be real and could indicate a Joule heating area in the midnight sector. The fact that the radar temperatures do not fully follow this peak might be an effect of the built-in conservatism of the statistical methods. The temperature drops in the normal distribution test data and the chi-squared data around 0800 UT are probably not real, but result from the rejection by those tests of all but the lowest temperature in several cycles around that period (see Table 5.10).

5.1.9 March 17-18, 1988

Ap = 9.7 F10.7A = 114.5/114.5 F10.7P = 114.1/117.4

The March 17-18 radar temperatures follow MSIS values closely from 1300 to 2400 UT, then stay fairly constant while MSIS values drop to about 50 degrees below them (Figure 5.11). In other words, the radar temperatures show no clear diurnal variation during this period but do oscillate considerably after 2400 UT.

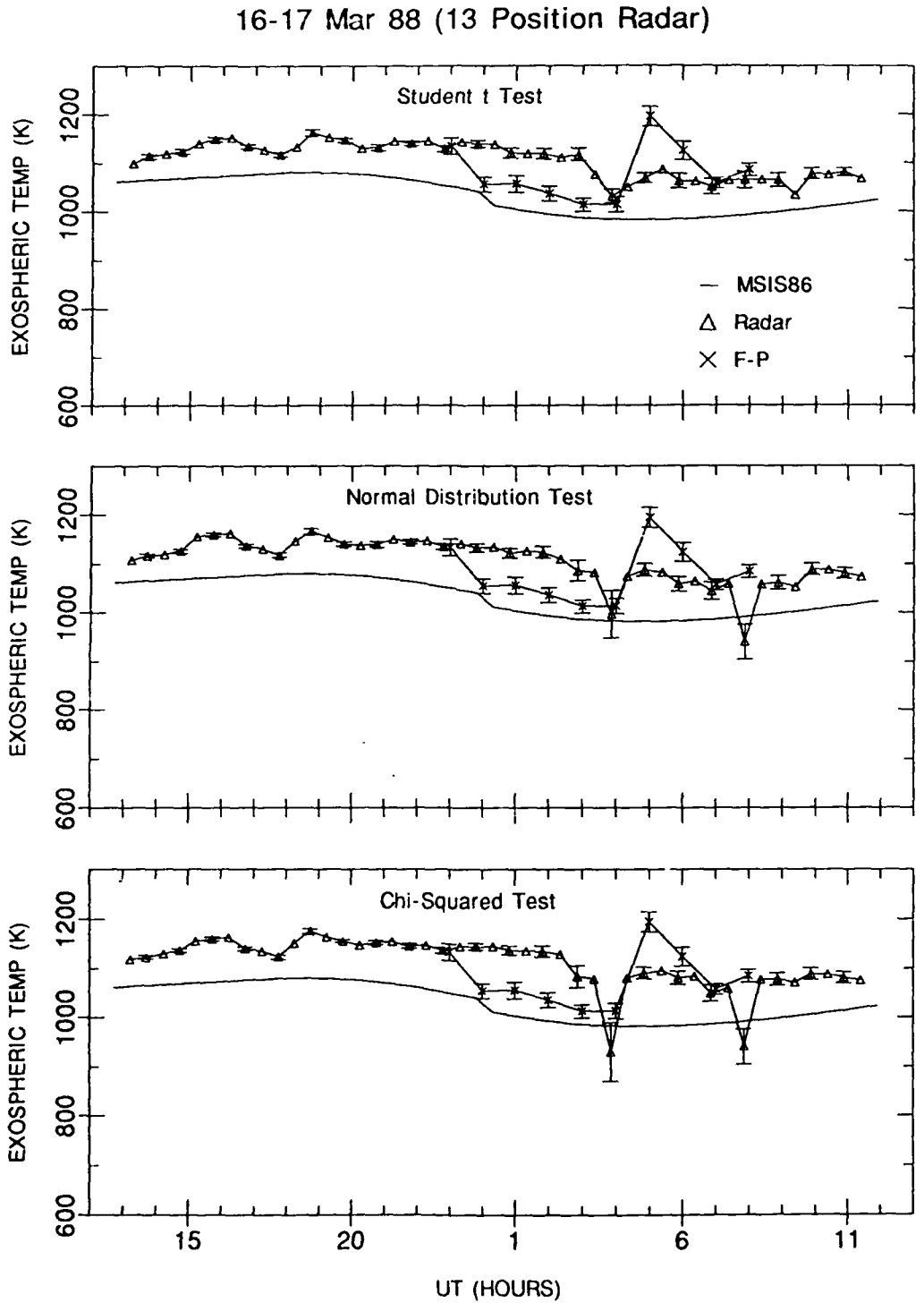

Fig. 5.10. Averaged exospheric temperatures and Fabry-Perot temperatures, March 16-17, 1988.

Table 5.10. Number of Temperatures Used per Cycle
March 16-17, 1988

Time	N	Stu t	Norm	Chi-Sq
12.74	11	4	6	7
13.22	13	4	7	8
13.72	13	4	4	11
14.23	12	6	6	7
14.73	13	3	3	9
15.23	13	5	6	8
15.73	13	5	7	7
16.24	13	4	4	5
16.74	13	6	7	9
17.24	13	5	5	5
17.75	13	5	6	8
18.25	13	2	2	2
18.75	13	4	6	7
19.25	13	5	4	6
19.75	13	5	6	6
20.26	13	5	6	9
20.76	13	3	4	7
21.26	13	4	1	1
21.77	13	5	6	6
22.31	13	4	6	6
22.81	13	3	4	4
23.32	13	4	2	4
23.82	13	8	7	8
24.33	12	6	6	8
24.85	7	3	3	2
25.31	10	5	8	9
25.84	10	4	5	7
26.35	10	3	1	1
26.86	9	3	3	3
27.37	9	4	2	1
27.85	12	4	1	1
28.36	10	3	1	1
28.84	8	6	4	6
29.36	9	3	3	3
29.90	6	2	2	3
30.34	11	7	4	7
30.86	9	5	6	6
31.37	11	3	1	1
31.85	11	2	1	1
32.36	12	3	1	1
32.89	12	4	5	7
[illegible].39	12	3	3	3
33.89	13	3	1	1
34.40	10	5	5	5
34.89	12	5	1	1
35.39	13	2	2	1
35.90	13	5	6	7

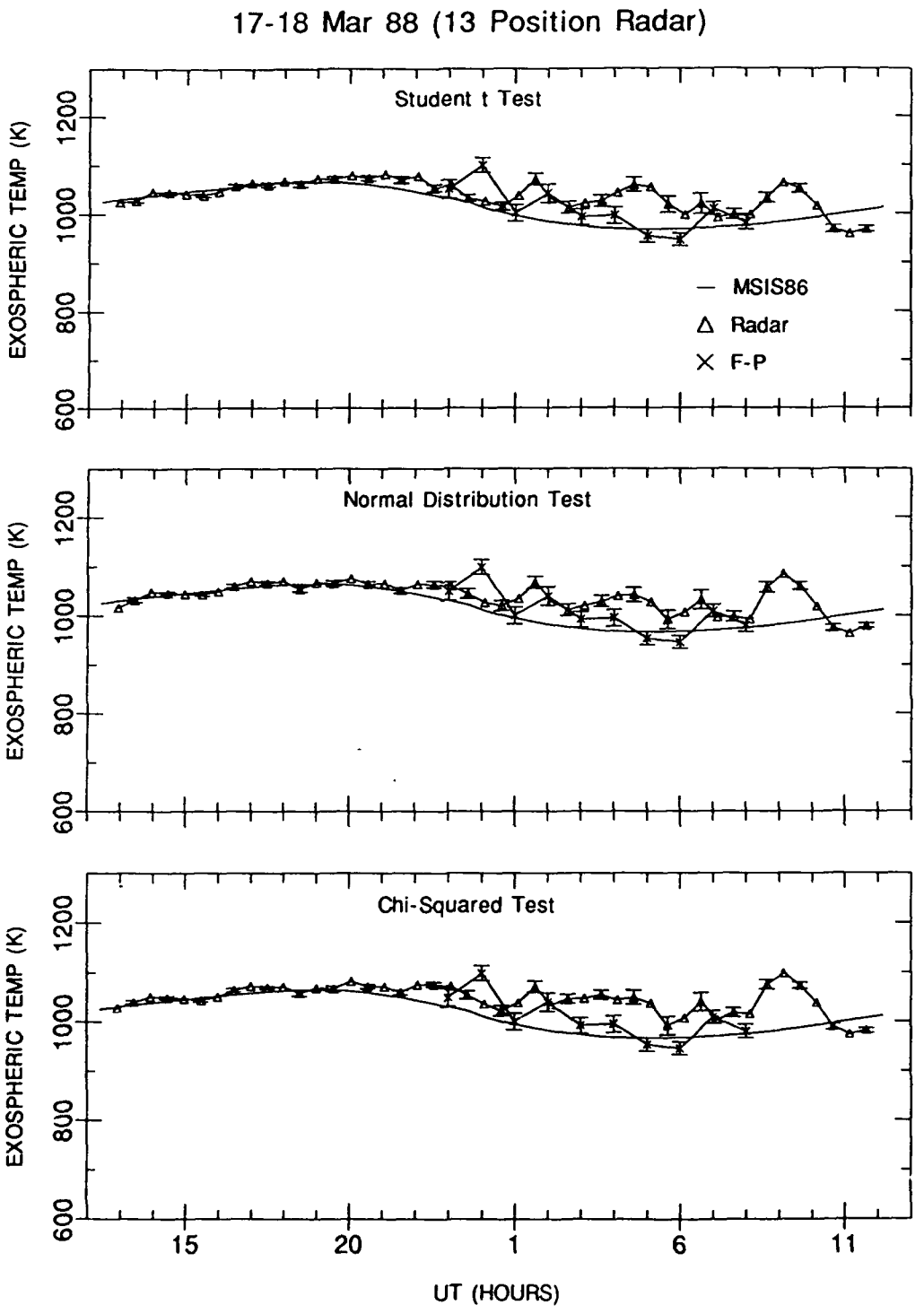

Fig. 5.11. Averaged exospheric temperatures and Fabry-Perot temperatures, March 17-18, 1988.

The pattern shows similarities to the previous day and probably indicates that enough Joule heating is going on in the midnight sector to keep neutral temperatures elevated. The spatial structure in the Joule heating would be reflected by the temporal oscillations in the temperatures. The Fabry-Perot temperatures follow the radar temperatures well and usually stay below them. Table 5.11 shows that many good data were available for this day, also supporting the credibility of the temperature pattern.

5.1.10 March 18-19, 1988

Ap = 7/4 F10.7A = 114.5/114.5 F10.7P = 117.4/116.1

The radar temperatures on this day are about 50 degrees below MSIS from 1300 to 1600 UT, roughly follow MSIS from 1600 to 2400 UT, then stay elevated about 50 to 100 degrees above MSIS until 1000 UT (Figure 5.12), repeating the early morning pattern of the last two days. There is an apparently real heating peak around 0700-0800 UT. Table 5.12 shows no problems with lack of data. The Fabry-Perot temperatures are mostly above the radar temperatures but follow the pattern quite closely. The apparent phase lag in the Fabry-Perot peak, compared to the 0700 UT radar peak, is probably an artifact of the averaging process for Fabry-Perot temperatures. If the temperatures were averaged on the half-hour instead of on the hour, the Fabry-Perot temperatures would peak at the same time as the radar peak, although about 100 degrees below it.

Table 5.11. Number of Temperatures Used per Cycle
March 17-18, 1988

Time	N	Stu t	Norm	Chi-Sq
12.40	13	3	1	1
12.92	12	5	1	1
13.43	12	4	4	5
13.92	13	5	6	10
14.44	13	7	9	10
14.97	13	5	5	6
15.48	13	5	7	8
15.98	13	7	8	8
16.48	13	3	3	3
16.99	13	5	5	8
17.49	13	6	8	8
17.99	13	3	3	4
18.49	13	3	2	2
19.00	13	3	3	4
19.53	15	3	3	3
20.06	13	2	1	1
20.57	13	5	5	7
21.07	13	3	4	6
21.57	13	4	1	1
22.07	13	3	4	6
22.57	13	5	6	8
23.08	13	3	1	1
23.58	13	6	5	7
24.09	13	4	1	1
24.59	11	4	4	4
25.10	12	5	4	5
25.60	9	3	3	4
26.12	9	3	3	4
26.61	11	4	4	5
27.11	11	3	3	5
27.62	11	3	3	3
28.09	8	3	4	4
28.62	9	5	4	5
29.12	12	4	1	1
29.62	13	2	2	2
30.14	10	3	3	3
30.63	9	3	4	4
31.13	12	3	3	6
31.63	11	6	6	9
32.12	10	5	5	6
32.63	13	5	1	1
33.15	12	5	8	9
33.64	13	5	7	10
34.14	13	3	4	5
34.65	12	4	5	6
35.15	13	6	7	8
35.65	13	3	3	3
36.15	13	7	11	12

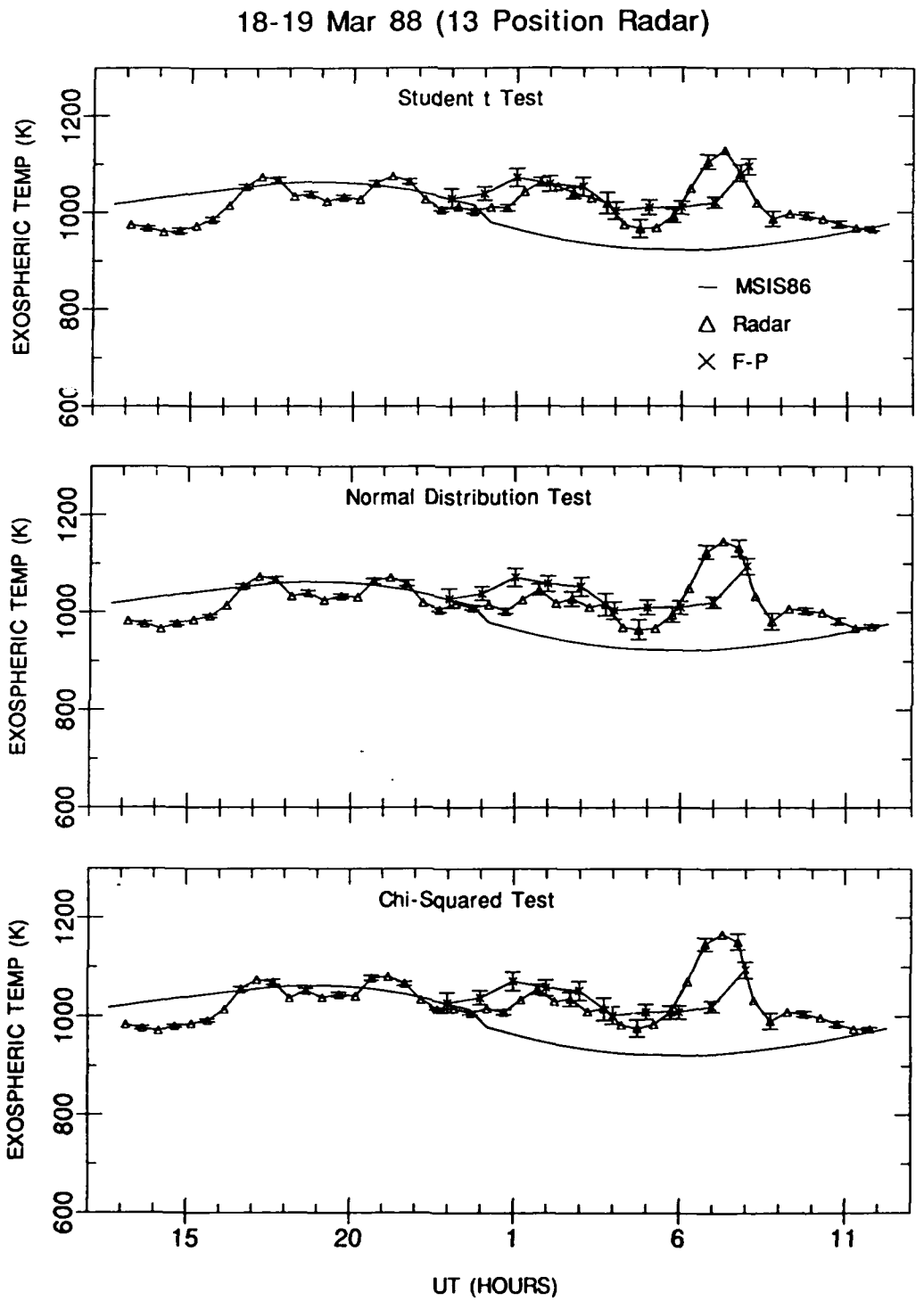

Fig. 5.12. Averaged exospheric temperatures and Fabry-Perot temperatures, March 18-19, 1988.

Table 5.12. Number of Temperatures Used per Cycle
March 18-19, 1988

Time	N	Stu t	Norm	Chi-Sq
12.65	13	5	8	9
13.16	13	5	9	9
13.66	13	6	8	8
14.16	13	3	3	3
14.66	13	2	3	7
15.15	12	4	8	8
15.67	13	4	5	5
16.17	13	3	3	3
16.67	13	4	4	4
17.17	13	2	2	3
17.68	13	3	3	3
18.18	13	2	2	2
18.68	13	3	3	2
19.18	13	4	5	6
19.69	13	5	5	6
20.19	13	4	3	1
20.69	13	4	5	6
21.19	13	3	3	4
21.70	13	4	3	5
22.20	13	2	2	6
22.70	13	9	8	10
23.20	13	3	2	5
23.70	13	7	9	9
24.21	13	3	4	8
24.71	13	3	5	6
25.22	10	5	4	5
25.73	10	3	1	1
26.24	10	5	3	5
26.74	8	3	2	2
27.19	7	3	3	3
27.79	8	3	2	2
28.24	6	3	3	3
28.74	10	3	3	4
29.25	12	6	3	6
29.74	11	3	3	4
30.26	11	5	5	6
30.78	7	6	6	7
31.26	9	5	7	8
31.77	9	2	3	3
32.26	12	3	1	1
32.76	12	3	2	2
33.26	13	5	6	7
33.78	11	5	6	6
34.27	12	4	7	8
34.77	13	4	2	4
35.27	13	3	4	6
35.77	13	7	7	8
36.27	13	4	9	9

5.2 Extrapolated Temperature Comparisons

The height of the emissions observed by the Fabry-Perot instrument is not known with precision. As discussed in Chapter II, 225 km is an acceptable average emission height, and this height was used to make general comparisons between the radar temperatures and the Fabry-Perot temperatures. Figures 5.13 through 5.18 show plots of Fabry-Perot temperatures and derived exospheric temperatures extrapolated down to 225 km. The radar exospheric temperatures were first linearly interpolated to the Fabry-Perot times, then extrapolated to 225 km using the Bates profile (Eqn. (3.1.4)). Error bars were also linearly interpolated. The 120 km neutral temperatures and the s parameters needed for the calculations were taken from the original MSIS output for the appropriate dates and times. The error bars on the interpolated temperatures were retained on the 225 km temperatures. Except for specific problem areas discussed for each day, the overall agreement is fairly good. The *t*-test results show less fluctuation than results of the other tests, but all tests appear to be producing reasonable temperatures.

5.3 Scatterplot Analysis

To get an overall picture of radar temperatures vs Fabry-Perot temperatures, bivariate data sets were constructed of all 79 data points used in the study. Radar temperatures and error bars were linearly interpolated to Fabry-Perot times. Figure 5.19 shows plots of the data sets for all three tests. The regression lines and correlation coefficients were calculated using the weighted correlation method described in Bevington [1969]. "SD of A" and "SD of B" are the standard

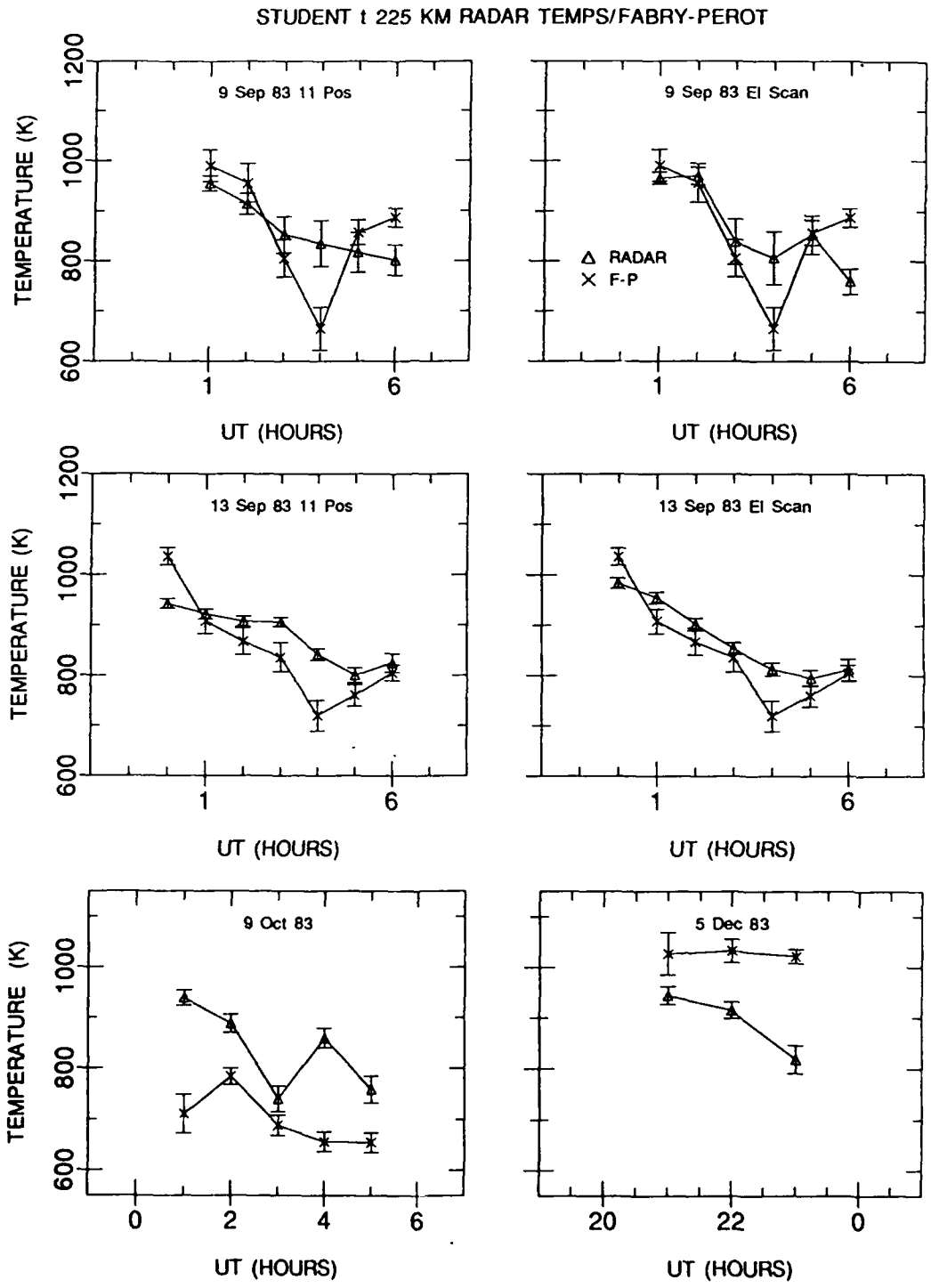

Fig. 5.13. Extrapolated radar temperatures vs Fabry-Perot temperatures, Student *t* test.

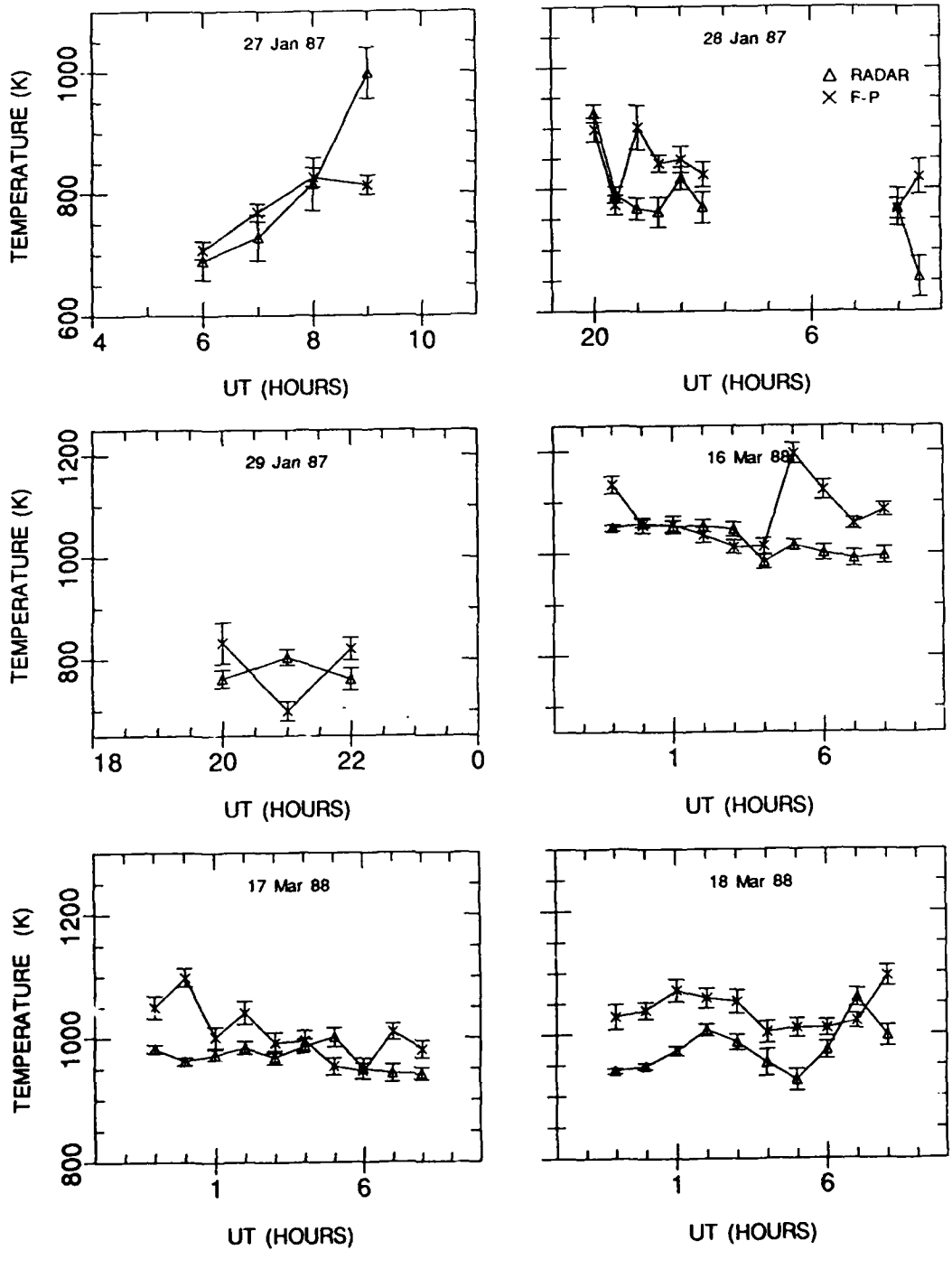

Fig. 5.14. Extrapolated temperatures vs Fabry-Perot temperatures, Student *t* test.

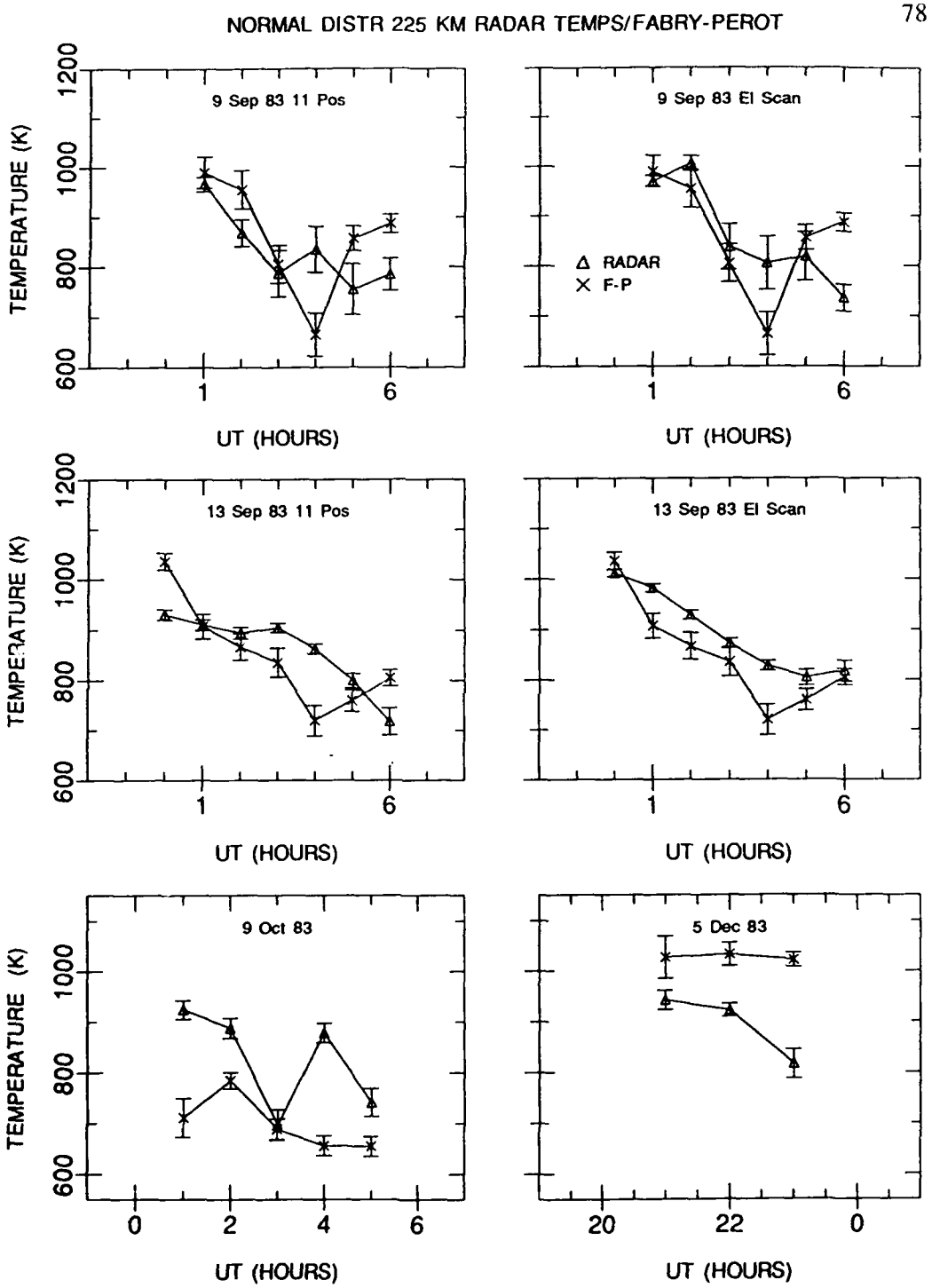

Fig. 5.15. Extrapolated temperatures vs Fabry-Perot temperatures, normal distribution test.

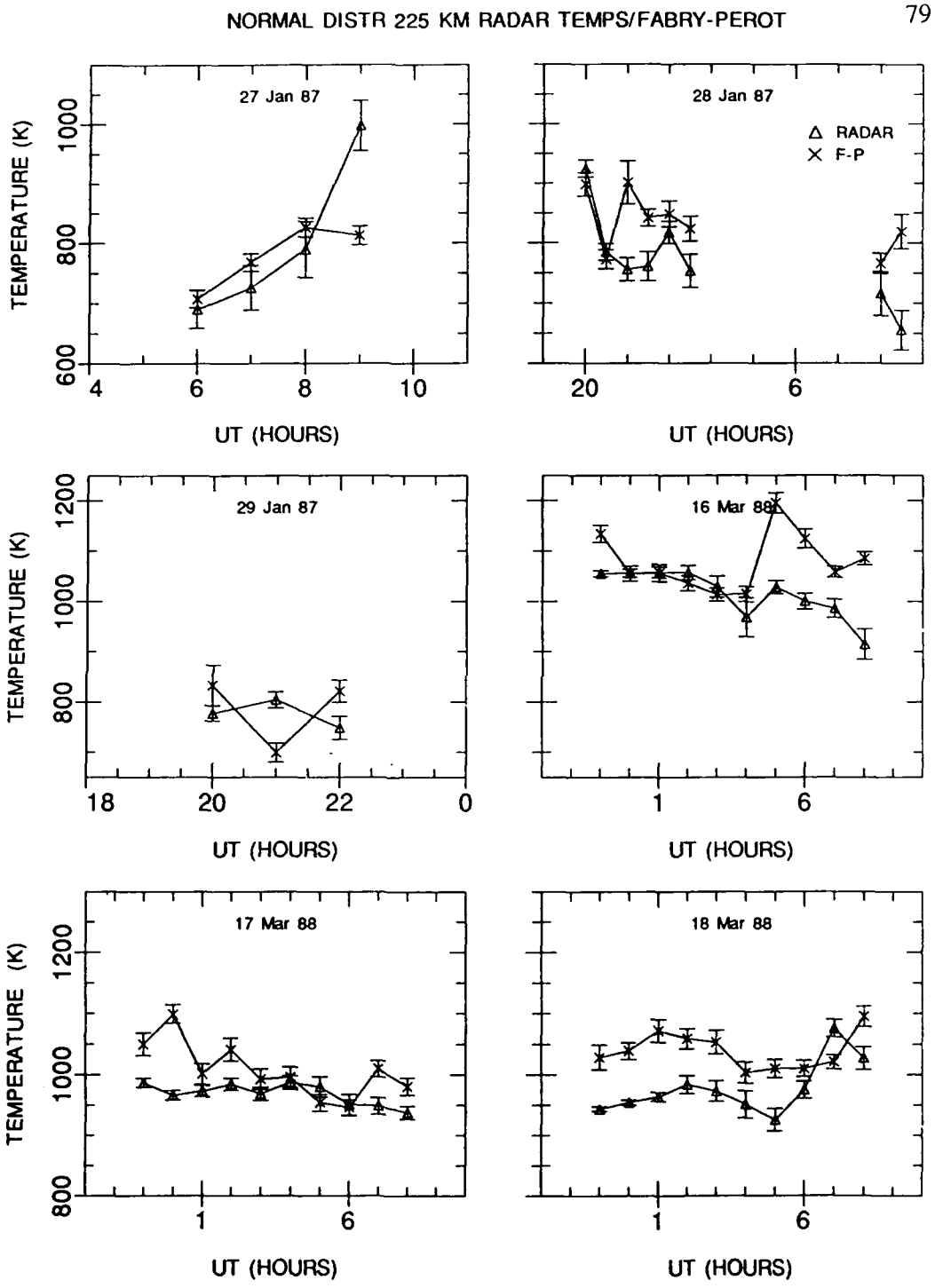

Fig. 5.16. Extrapolated temperatures vs Fabry-Perot temperatures, normal distribution test.

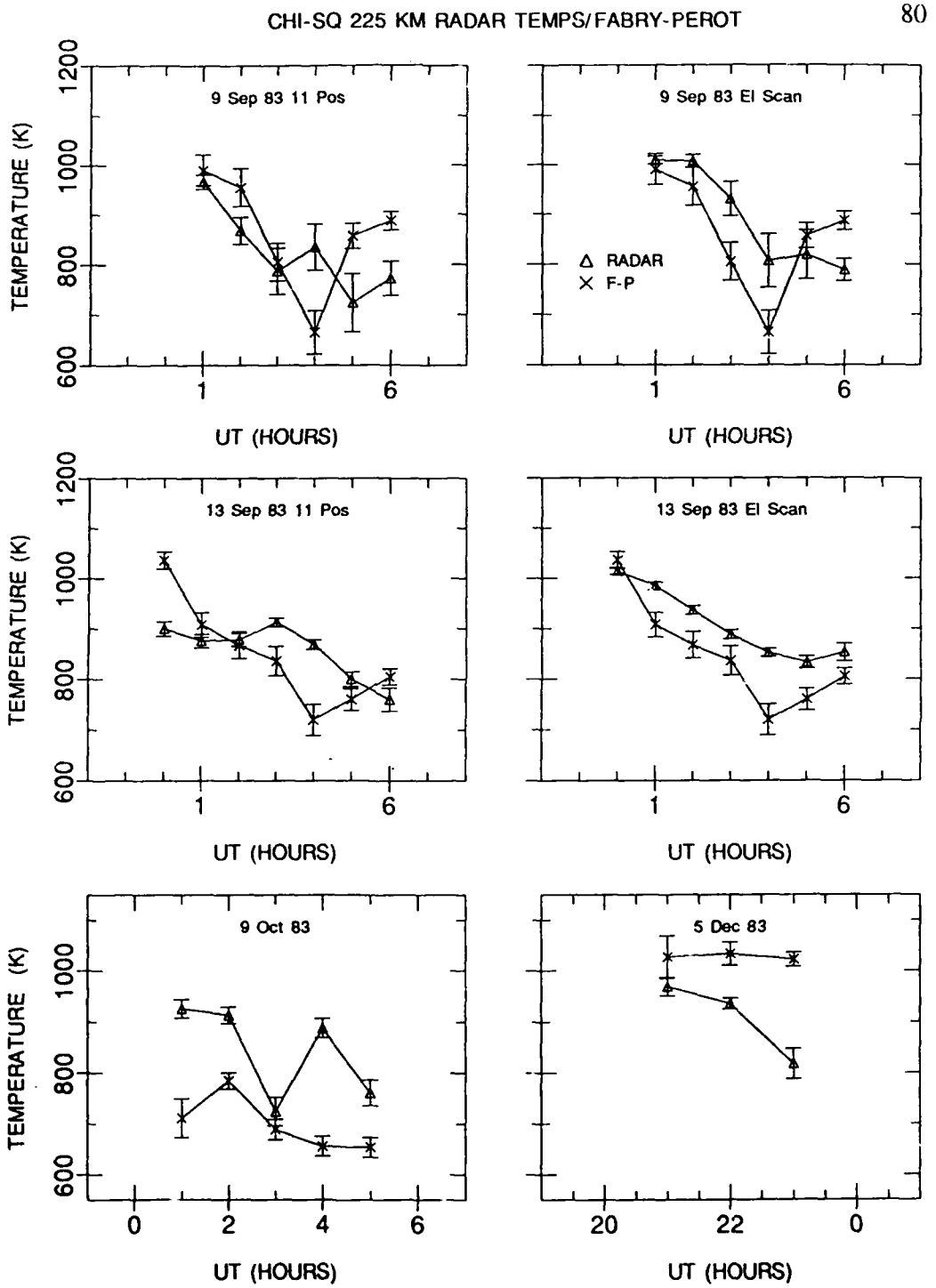

Fig. 5.17. Extrapolated temperatures vs Fabry-Perot temperatures, chi-squared test.

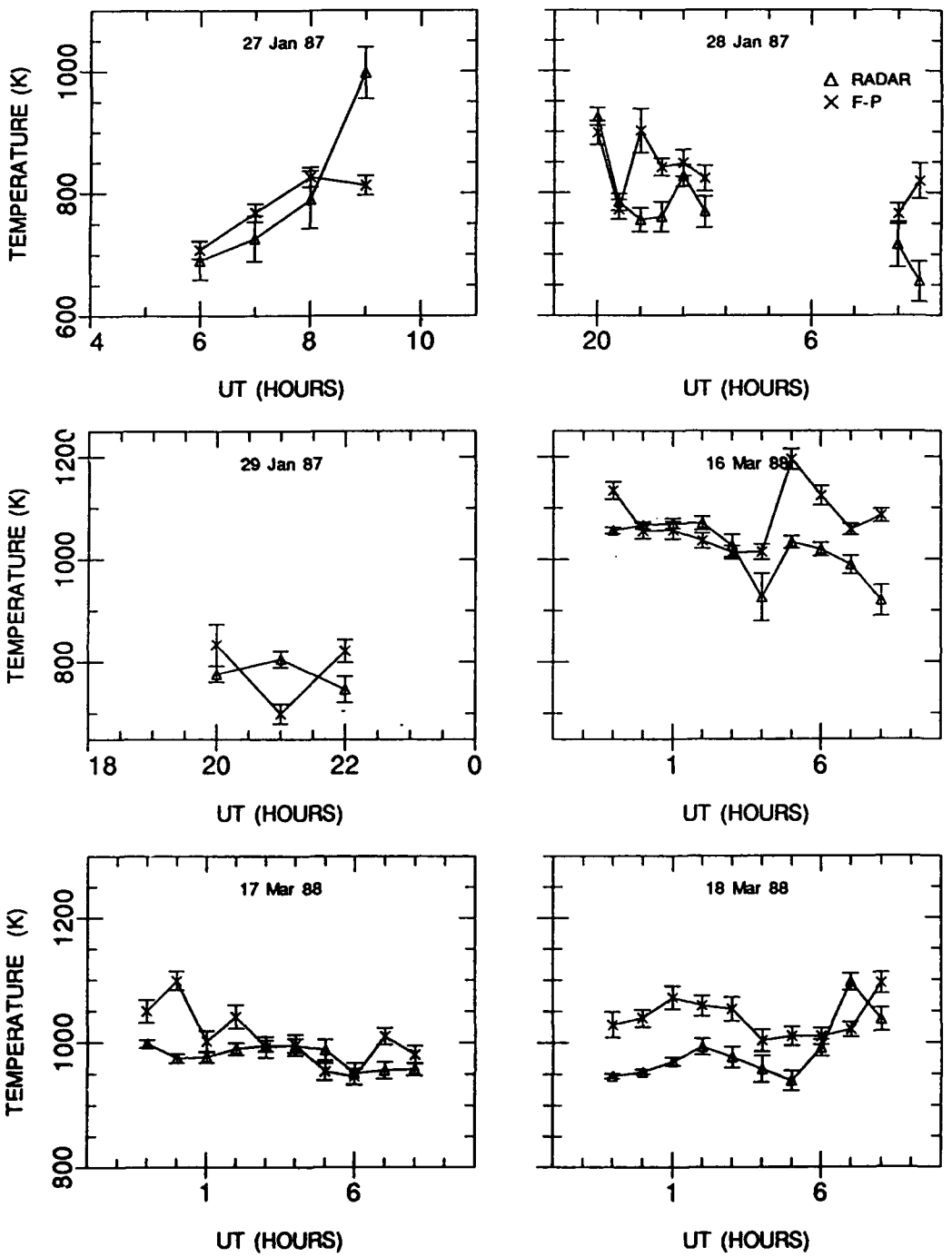

Fig. 5.18. Extrapolated temperatures vs Fabry-Perot temperatures, chi-squared test.

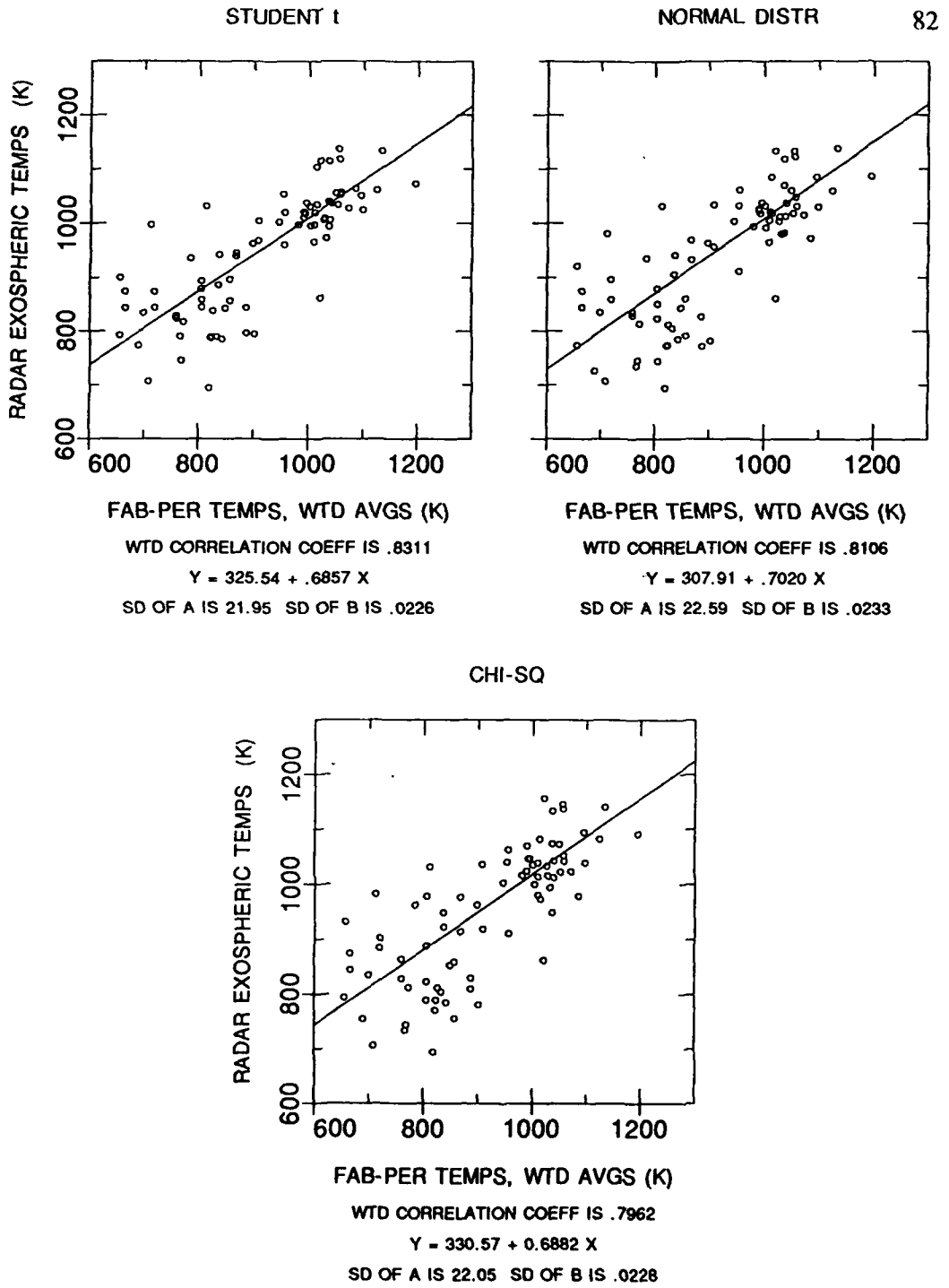

Fig. 5.19. Scatterplots, exospheric temperature vs Fabry-Perot temperatures, with regression lines.

deviations of the coefficients in the regression line equation Y = A + BX.

All bivariate data sets are highly correlated. The *t*-test group shows the highest correlation and the least scatter about the regression line, and the chi-squared group shows the most scatter. This result was not unexpected, since the chi-squared test often chose either more or fewer temperatures than the *t* test.

Figure 5.20 is the same set of plots, except that unit lines have been substituted for regression lines. The expected result is for all radar temperatures to be higher than their corresponding Fabry-Perot temperatures and therefore all points on the scatterplot to be above the unit lines. This is true most of the time. However, the high temperatures are clustered about the unit lines (representing mainly the March, 1988 data). Speculation on this trend leads to several possibilities:

(1) Perhaps, for some reason, the optical emission layer is higher than normal in the March, 1988 data, yielding temperatures closer to actual exospheric temperatures.

(2) Perhaps the March, 1988 optical data are examples of the non-thermal broadening described by Yee [1988]. A few percent deviation from the thermalized emission profile could result in a 50° K difference in temperature, which is about the difference between many of the 225 km radar temperatures and the Fabry-Perot temperatures for these days.

(3) Perhaps the statistical tests are more conservative with higher temperature data sets. Actually, this doesn't seem likely, but when I examined the March, 1988 data, I did notice a tendency towards lower than normal standard deviations on the temperatures produced by TOSS4. So, although the temperature

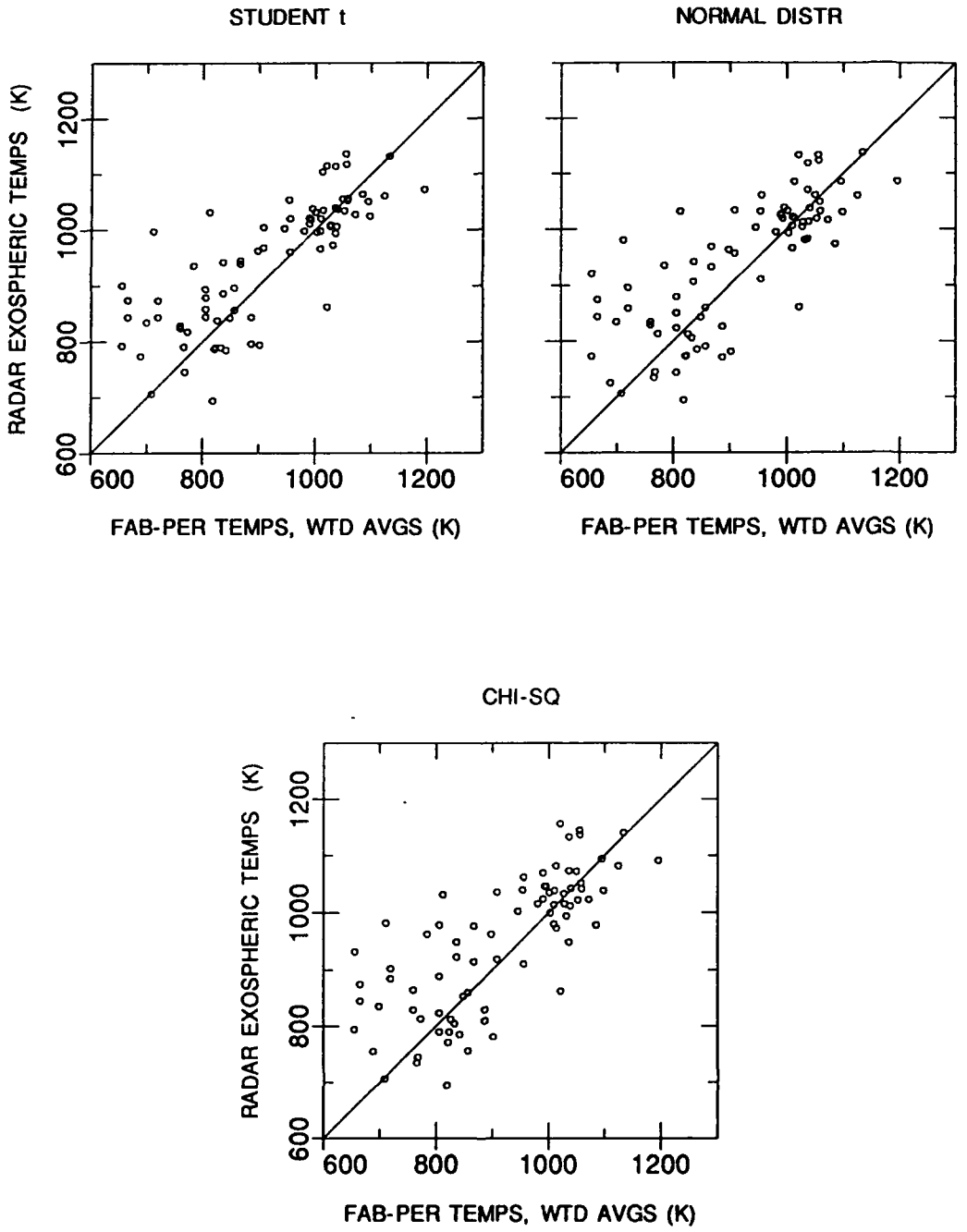

Fig. 5.20. Scatterplots, exospheric temperatures vs Fabry-Perot temperatures, with unit lines.

range over an entire cycle may only be 150 degrees, the tests still rejected several of the temperatures, based on very small population standard deviations.

(4) Perhaps the distribution of the neutral temperatures is not exactly normal above 1000° K. A spread in the distribution would cause the tests to underestimate the true mean (in effect making them more conservative). Of course, this hypothesis assumes that (1) is not true and might be tested by looking at low-latitude data.

Figure 5.21 shows the same plots as Figure 5.20, but includes the error bars. In general, the error bars of both data types are similar in magnitude.

Figures 5.22 and 5.23 are plots of the Fabry-Perot and 225 km radar temperature sets. The approximate one-to-one correspondence below 1000° K and the small variance in the *t*-test data are both very evident. The variance in the chi-squared data set is rather troublesome. In fact, below 1000° K there appears to be little correlation at all. Figure 5.24 shows what the data sets look like without the March, 1988 data, and the overall agreement is quite good.

Weighted mean differences between the radar temperatures and the Fabry-Perot temperatures were computed for the exospheric and 225 km sets, with and without March, 1988 data, using Eqn. (3.4.1). The results are shown in Table 5.13. For a Bates profile, one would expect a 25 to 50 degree difference between the exospheric temperature and the temperature at 225 km. The mean differences for the exospheric sets fall within or close to this range, both with and without March, 1988. However, the mean differences for the 225 km sets reveal the significant effect of the March, 1988 data, and the "best" differences (i.e., approaching zero) are clearly without that data. If the March, 1988 data are not considered, and

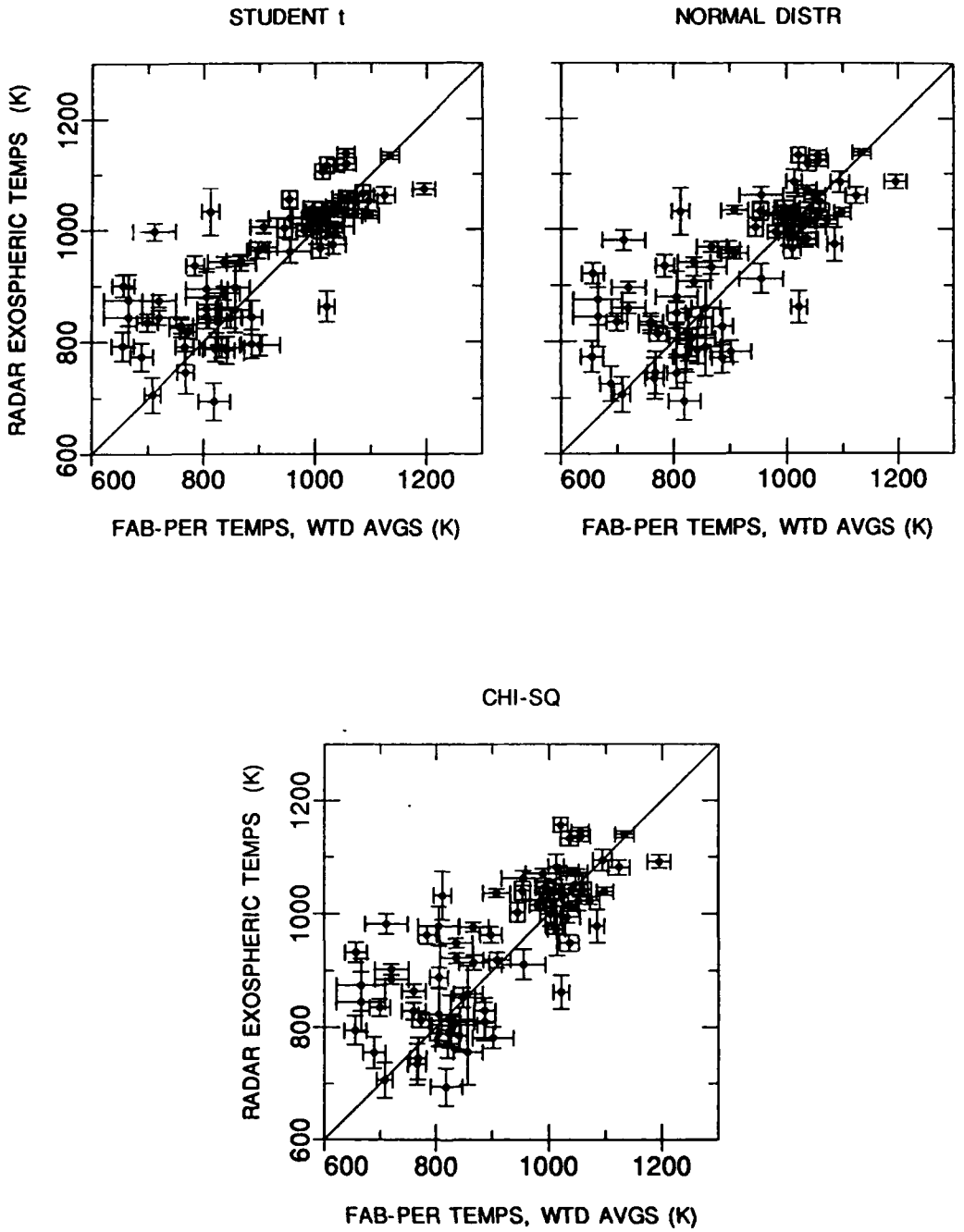

Fig. 5.21. Scatterplots, exospheric temperatures vs Fabry-Perot temperatures, with error bars.

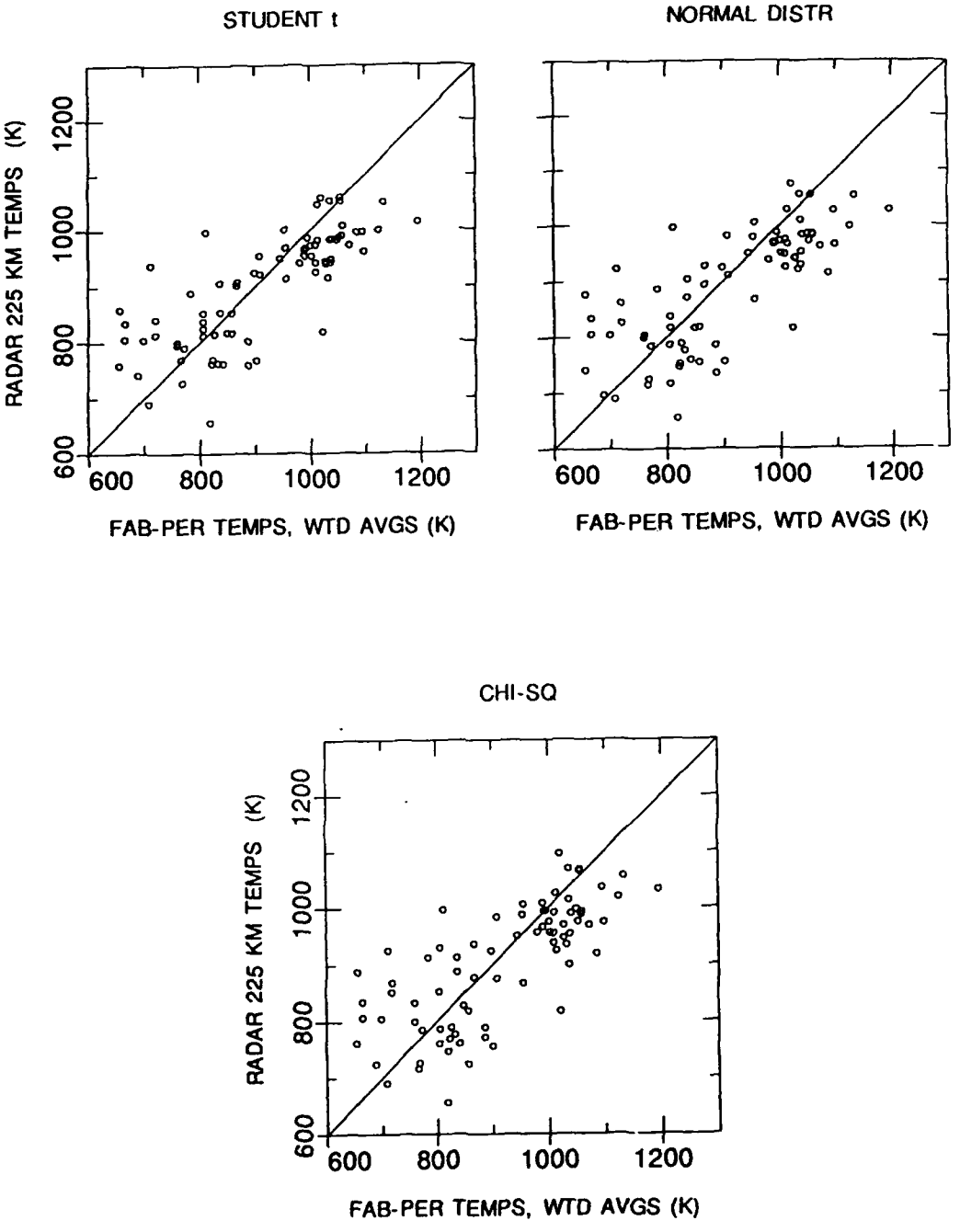

Fig. 5.22. Scatterplots, extrapolated temperatures vs Fabry-Perot temperatures, with unit lines.

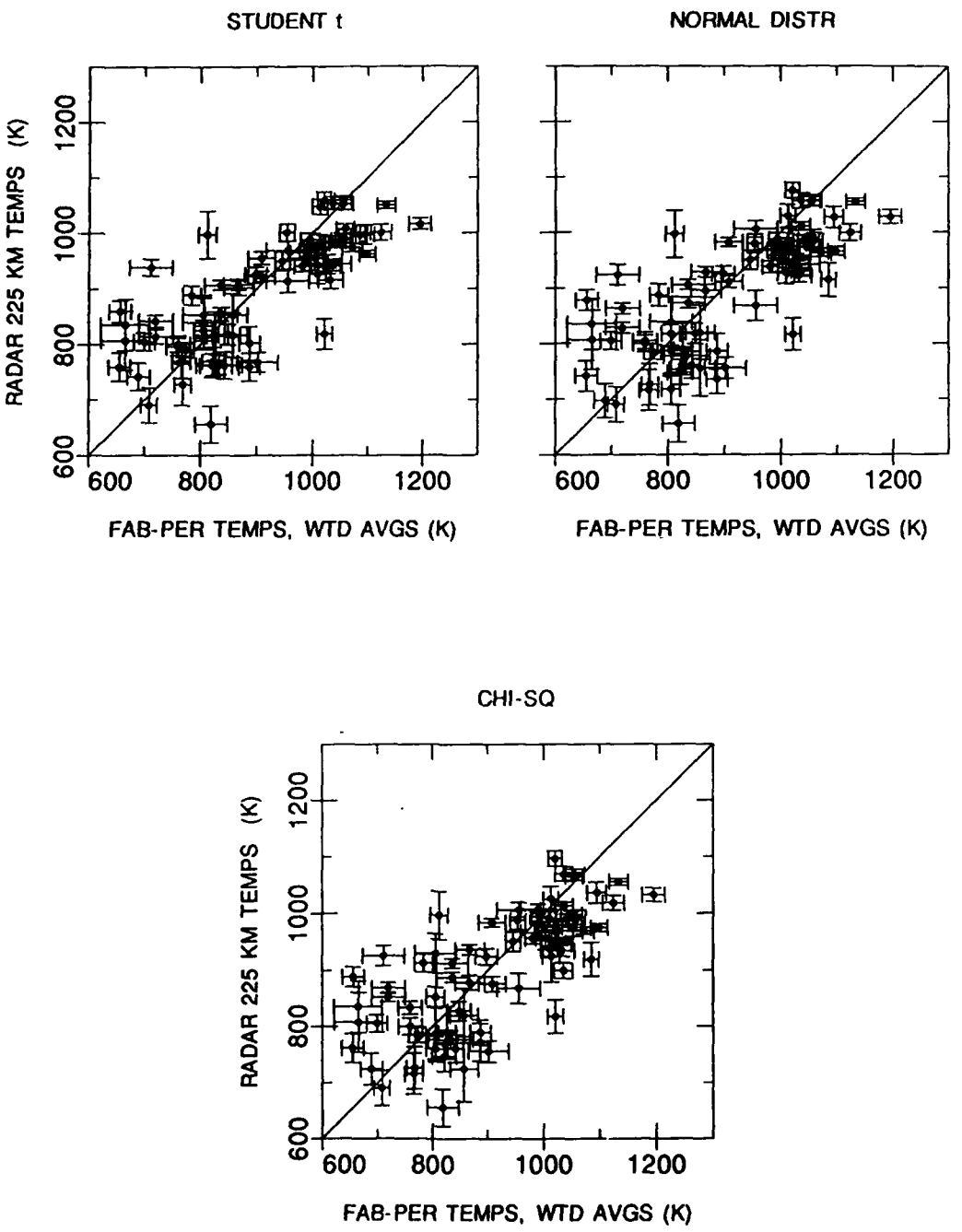

Fig. 5.23. Scatterplots, extrapolated temperatures vs Fabry-Perot temperatures, with error bars.

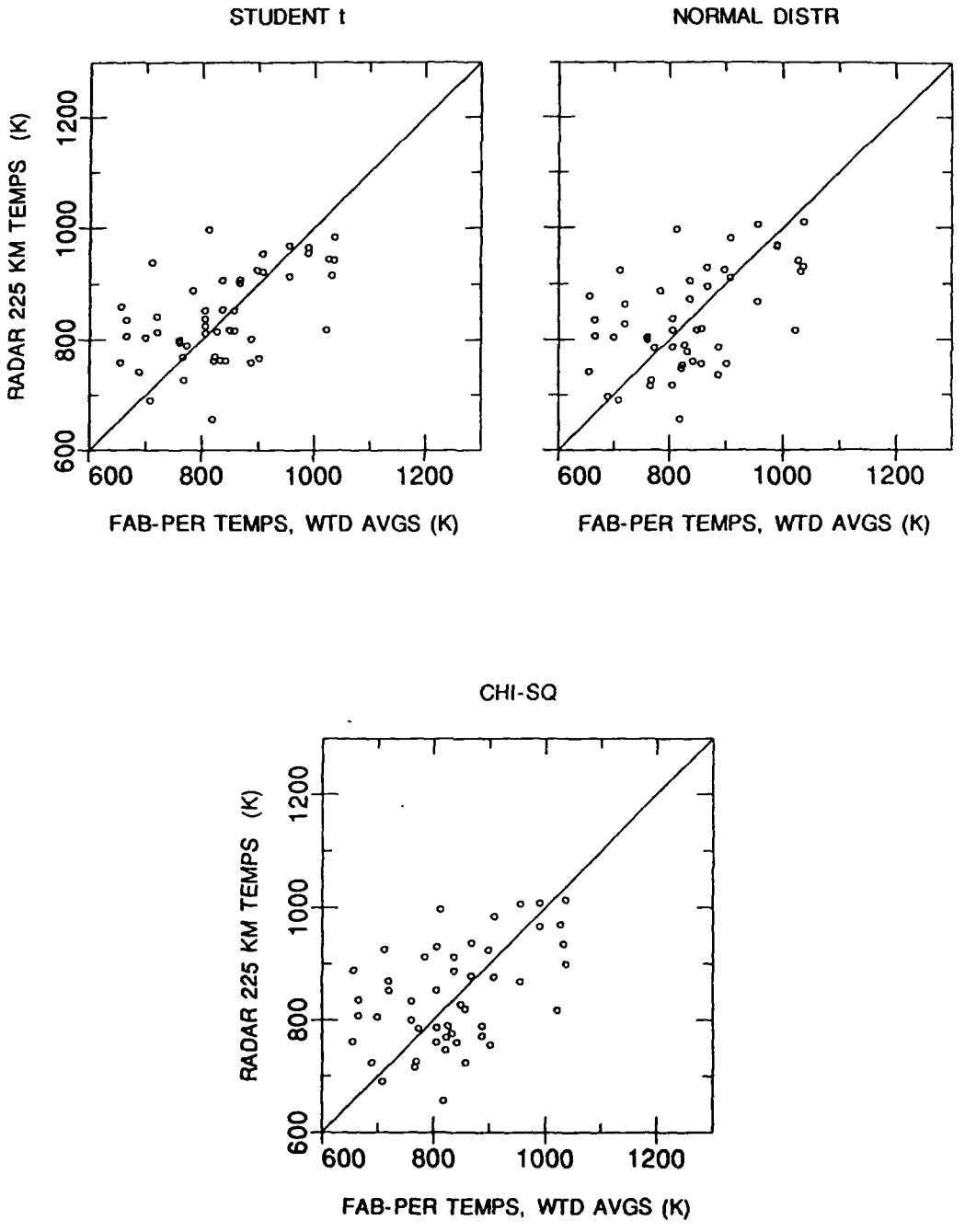

Fig. 5.24. Scatterplots, extrapolated temperatures vs Fabry-Perot temperatures, without March, 1988.

despite masking of the scatter in the data, the mean difference analysis strongly supports the validity of exospheric temperatures derived by statistical methods.

Table 5.13. Weighted Mean Differences Between Radar Temperatures and Fabry-Perot Temperatures

	Exo vs F-P	225 km vs F-P
All data:		
t Test	22.64	-28.24
Norm Dist	21.48	-29.24
Chi-Sq	31.06	-20.25
Without Mar 88:		
t Test	43.02	4.74
Norm Dist	40.59	2.16
Chi-Sq	50.82	11.91

CHAPTER VI

CONCLUSIONS

6.1 Summary and Conclusions

Sondrestrom incoherent-scatter radar observations of the high-latitude F-region were used to derive exospheric temperatures through the ion energy balance equation. Exospheric temperatures in each observation cycle were selectively assigned to two populations, a non-Joule-heated group and a (probably) Joule-heated group, by using statistical tests. The weighted mean of the non-Joule-heated population was used as the mean exospheric temperature. The tests used to separate the groups were the Student *t* test, the normal distribution test, and the chi-squared test.

The basic premise of the study was that some of the temperatures in Sondrestrom's field of view were not affected by Joule heating. This assumption rested on cited evidence of the spatial scale of Joule heating being less than the scale of a radar observation scan.

The Student *t* test was based on the following assumptions:

(1) The distribution of sample means was a *t* distribution.

(2) The weighted mean of the two lowest temperatures was a valid member of the distribution of means.

(3) The weighted error of the population mean calculated from the uncertainties of the values used in the mean was a valid standard deviation of the *t* distribution.

The normal distribution test and the chi-squared test were based on the

following assumptions:

(1) The non-Joule-heated exospheric temperatures were normally distributed.

(2) The population standard deviation was known and could be represented by an average of the uncertainties of all temperatures in the observation cycle.

The mean exospheric temperatures were used to calculate three-point running averages, which were compared to one-hour weighted averages of Fabry-Perot neutral temperatures. The exospheric temperatures were also extrapolated to 225 km, the assumed average emission height for the Fabry-Perot observations, and compared again to the optically derived temperatures. General comparisons to MSIS model temperatures were also made.

All comparisons showed high correlations between radar-derived temperatures and Fabry-Perot temperatures. Exospheric temperatures often showed 100-200° K deviations from MSIS model temperatures and occasionally showed evidence of significant neutral heating in specific time periods.

Of the tests used, the *t* test produced the most consistent (least variable) results and the chi-squared test the most. The normal distribution test results fell somewhere in between.

I have one main conclusion: the statistical technique used in this study appears to produce reasonable and realistic exospheric temperatures despite contamination of the original radar data by Joule heating effects. Testing the technique on other data sets should bring to light any consistent problems, e.g., always underestimating or overestimating the temperature under certain conditions, etc. Once the fine-tuning is done (if any is needed), the technique would be the first one to produce unbiased estimates of exospheric temperatures at high latitudes

from radar data.

6.2 Recommendations for Further Research

Several questions arose during the study. The first involves verification of the technique. Verification might consist of:

(1) using the technique to examine low-latitude or quiet mid-latitude radar data. Results of the technique should be the same as computing the means of all derived exospheric temperatures per scan using the ion energy equation.

(2) *looking at more comparisons* from Sondrestom for March, 1988 and later, when the data become available.

Once the technique is verified, areas of research might be:

(1) trying the technique on Sondrestrom up-B observation scans when Fabry-Perot data are also available. This would involve establishing a time scale in lieu of a spatial scale over which the statistical tests could be used.

(2) using the technique on Chatanika data, which is mostly up-B, once the previous test is done. Comparisons could be made to Atmospheric Explorer C data, if available.

(3) looking for solar cycle variations in the Sondrestrom data, and continuing the derivations of exospheric temperatures through solar cycle maximum.

(4) extending use of the technique to EISCAT radar data.

It would also be useful to examine in more detail all the data during the time periods of the radar observations, that is, the ion convection patterns, the ion temperature patterns, etc., to check consistency with the derived exospheric temperature patterns.

REFERENCES

Alcaydé, D., P. Bauer, C. Jaeck, and J. L. Falin, Latitudinal diurnal variation of some atmospheric parameters determined by a simultaneous analysis of incoherent-scatter and satellite-drag data, J. Geophys. Res., 77, 2368-2376, 1972.

Alcaydé, D., J. Fontanari, P. Bauer, and O. de la Beaujardiere, Some properties of the auroral thermosphere inferred from initial EISCAT observations, Radio Sci., 18, 881-886, 1983.

Alcaydé, D., P. Bauer, and J. Fontanari, Dynamical coupling of the auroral F-region ionosphere and thermosphere: case studies, J. Atmos. Terr. Phys., 46, 625-633, 1984.

Banks, P. M., Collision frequencies and energy transfer-electrons, Planet. Space Sci., 14, 1085-1103, 1966a.

Banks, P. M., Collision frequencies and energy transfer-ions, Planet. Space Sci., 14, 1105-1122, 1966b.

Banks, P. M., Observations of joule and particle heating in the auroral zone, J. Atmos. Terr. Phys., 39, 179-193, 1977.

Banks, P. M. and G. Kockarts, Aeronomy, 785 pp., Academic Press, New York, 1973.

Banks, P. M., J. C. Foster, and J. R. Doupnik, Chatanika radar observations relating to the latitudinal and local time variations of Joule heating, J. Geophys. Res., 86, 6869-6878, 1981.

Baron, M. J., and R. H. Wand, F region ion temperature enhancements resulting from Joule heating, J. Geophys. Res., 88, 4114-4118, 1983.

Bates, D. R., Some problems concerning the terrestrial atmosphere above the 100 km level, Proc. Roy. Soc. London, Ser. A, 253, 451-462, 1959.

Bauer, P., P. Waldteufel, and D. Alcaydé, Diurnal Variations of the Atomic Oxygen Density and Temperature Determined from Incoherent Scatter Measurements in the Ionospheric F Region, J. Geophys. Res., 75, 4825-4832, 1970.

Bevington, P. R., Data Reduction and Error Analysis for the Physical Sciences, 336 pp., McGraw-Hill, New York, 1969.

Burnside, R. G., C. A. Tepley, and V. B. Wickwar, The O^+-O collision cross-section: Can it be inferred from aeronomical measurements?, Annls. Géophys., 5A(6), 434-350, 1987.

Burnside, R. G., M. P. Sulzer, and J. C. G. Walker, Determination of thermospheric temperatures and neutral densities at Arecibo from the ion energy balance, J. Geophys. Res., 93, 8642-8650, 1988.

Cogger, L. L., J. C. G. Walker, J. W. Meriwether, Jr., and R. G. Burnside, F region airglow: are ground-based observations consistent with recent satellite results?, J. Geophys. Res., 85, 3013-3020, 1980.

Evans, J. V., Theory and practice of ionosphere study by Thomson scatter radar, Proc. IEEE, 57, 496-530, 1969.

Evans, J. V., W. L. Oliver, and J. E. Salah, Thermospheric properties as deduced from incoherent scatter measurements, J. Atmos. Terr. Phys., 41, 259-278, 1979.

Foster, J. C., J.-P. St.-Maurice, and V. J. Abreu, Joule heating at high latitudes, J. Geophys. Res., 88, 4885-4896, 1983.

Hernandez, G., Measurement of thermospheric temperatures and winds by remote Fabry-Perot spectrometry, Opt. Eng., 19, 518-532, 1980.

Kelley, M. C., The Earth's Ionosphere: Plasma Physics and Electrodynamics, 487 pp., Academic Press, San Diego, 1989.

Kelly, J. D., and V. B. Wickwar, Radar measurements of high-latitude ion composition between 140 and 300 km altitude, J. Geophys. Res., 86, 7617-7626, 1981.

Killeen, T. L., Energetics and dynamics of the Earth's thermosphere, Rev. Geophys., 25, 433-454, 1987.

Killeen, T. L., P. B. Hays, G. R. Carignan, R. A. Heelis, W. B. Hanson, N. W. Spencer, and L. H. Brace, Ion-neutral coupling in the high-latitude *F* region: Evaluation of ion heating terms from Dynamics Explorer 2, J. Geophys. Res., 89, 7495-7508, 1984.

Meier, R. R., D. J. Strickland, J. H. Hecht, and A. B. Christensen, Deducing composition and incident electron spectra from ground-based auroral optical measurements: a study of auroral red line processes, J. Geophys. Res., 94, 13,541-13,552, 1989.

Oliver, W. L., Millstone Hill incoherent scatter observations of exospheric temperature over 25 to 60 degrees north latitude, Geophys. Res. Lett., 1, 915-918, 1984.

Rees, M. H., and R. G. Roble, Excitation of O(^{1}D) atoms in aurorae and emission of the [OI] 6300-Å line, Can. J. Phys., 64, 1608-1613, 1986.

Roble, R. G., The calculated and observed diurnal variation of the ionosphere over Millstone Hill on 23-24 March 1970, Planet. Space Sci., 23, 1017-1033, 1975.

Roble, R. G., R. E. Dickinson, and E. C. Ridley, Global circulation and temperature structure of thermosphere with high-latitude plasma convection, J. Geophys. Res., 87, 1599-1614, 1982.

Schunk, R. W., and A. F. Nagy, Electron temperatures in the F region of the ionosphere: theory and observations, Rev. Geophys. Space Phys., 16, 355-399, 1978.

Schunk, R. W., and J. C. G. Walker, The theory of charged particle temperatures in the upper atmosphere, in Progress in High Temperature Physics and Chemistry V, edited by C. A. Rouse, pp. 1-62, Pergamon Press, New York, 1973.

St.-Maurice, J. P., and W. B. Hanson, Ion frictional heating at high latitudes and its possible use for an in situ determination of neutral thermospheric winds and temperatures, J. Geophys. Res., 87, 7580-7602, 1982.

Straus, J. M., and M. Schulz, Magnetospheric convection and upper atmospheric dynamics, J. Geophys. Res., 81, 5822-5832, 1976.

Waldteufel, P., and L. Cogger, Measurements of the neutral temperature at Arecibo, J. Geophys. Res., 76, 5322-5336, 1971.

Watkins, B. J., and P. M. Banks, A preliminary study of high-latitude thermospheric temperatures from incoherent scatter radar observations, J. Geophys. Res., 79, 5307-5310, 1974.

Wickwar, V. B., Chatanika radar measurements, in Atmospheres of Earth and the Planets, edited by B. M. McCormac, pp. 111-124, D. Reidel, Dordrecht, Holland, 1975.

Wickwar, V. B., L. L. Cogger, and H. C. Carlson, The 6300 Å $O(^1D)$ airglow and dissociative recombination, Planet. Space Sci., 22, 709-724, 1974.

Wickwar, V. B., J. D. Kelly, O. de la Beaujardiere, C. A. Leger, F. Steenstrup, and C. H. Dawson, Sondrestrom overview, Geophys. Res. Lett., 1, 883-886, 1984.

Yee, J. H., Non-thermal distribution of $O(^1D)$ atoms in the night-time thermosphere, Planet. Space Sci., 36, 89-97, 1988.

APPENDIX

BIBLIOGRAPHY

Banks, P. M., The temperature coupling of ions in the ionosphere, Planet. Space Sci., 15, 77-93, 1967.

Banks, P. M., Energy sources of the high latitude upper atmosphere, in Exploration of the Polar Upper Atmosphere, edited by C. S. Deehr and J. A. Holtet, pp. 113-128, D. Reidel, Dordrecht, Holland, 1981.

Burington, R. S., and D. C. May, Jr., Handbook of Probability and Statistics with Tables, 462 pp., McGraw-Hill, New York, 1970.

Burnside, R. G., J. W. Meriwether, Jr., and M. R. Torr, Contamination of ground-based measurements of OI (6300 Å) and NI (5200 Å) airglow by OH emissions, Planet. Space Sci., 25, 985-988, 1977.

Cole, K. D., Electrodynamic heating and movement of the thermosphere, Planet. Space Sci., 19, 59-75, 1971.

Hamburg, M., Statistical Analysis for Decision Making, 829 pp., Harcourt Brace Jovanovich, New York, 1983.

Hedin, A. E., MSIS-86 thermospheric model, J. Geophys. Res., 92, 4649-4662, 1987.

Hernandez, G., Fabry-Perot Interferometers, 343 pp., Cambridge University Press, Cambridge, 1986.

Hernandez, G., and R. G. Roble, Direct measurements of nighttime thermospheric winds and temperatures, 1, Seasonal variations during geomagnetic quiet periods, J. Geophys. Res., 81, 2065-2074, 1976a.

Hernandez, G., and R. G. Roble, Direct measurements of nighttime thermospheric winds and temperatures, 2, Geomagnetic storms, J. Geophys. Res., 81, 5173-5181, 1976b.

Hernandez, G., and R. G. Roble, Direct measurements of nighttime thermospheric winds and temperatures, 3, Monthly variations during solar minimum, J. Geophys. Res., 82, 5505-5511, 1977.

Hernandez, G., T. E. VanZandt, V. L. Peterson, and J. P. Turtle, Comparison of optical and incoherent scatter measurements of nighttime exospheric temperature at the magnetic equator, J. Geophys. Res., 80, 3271-3274, 1975.

McCormac, F. G., T. L. Killeen, and B. Nardi, How close are ground-based Fabry-Perot thermospheric wind and temperature measurements to exospheric values? A simulation study, Planet. Space Sci., 35, 1255-1265, 1987.

Meriwether, J. W., Jr., Observations of thermospheric dynamics at high latitudes from ground and space, Radio Sci., 18, 1035-1052, 1983.

Nisbet, J. S., Neutral atmospheric temperatures from incoherent scatter observations, J. Atmos. Sci., 24, 586-593, 1967.

Oliver, W. L., J. C. Foster, J. M. Holt, G. B. Loriot, V. B. Wickwar, J. D. Kelly, O. de la Beaujardiere, P. F. Bythrow, C. I. Meng, F. J. Rich, and R. E. Huffman, Initial Millstone Hill, Sondrestrom, and HILAT observations of thermospheric temperatures and frictional heating, Geophys. Res. Lett., 1, 911-914, 1984.

Pearson, E. S., and H. O. Hartley (Eds.), Biometrika Tables for Statisticians, Vol I, 270 pp., Biometrika Trust, London, 1976.

Rasmussen, C. E., J. J. Sojka, R. W. Schunk, V. B. Wickwar, O. de la Beaujardiere, J. Foster, and J. Holt, Comparison of simultaneous Chatanika and Millstone Hill temperature measurements with ionospheric model predictions, J. Geophys. Res., 93, 1922-1932, 1988.

Reber, C. A., and A. E. Hedin, Heating of the high-latitude thermosphere during magnetically quiet periods, J. Geophys. Res., 79, 2457-2461, 1974.

Rees, M. H., Physics and Chemistry of the Upper Atmosphere, 289 pp., Cambridge University Press, Cambridge, 1989.

Schunk, R. W., The terrestrial ionosphere, in Solar-Terrestrial Physics, edited by R. L. Carovillano and J. M. Forbes, pp. 609-676, D. Reidel, Hingham, MA, 1983.

Schunk, R. W., and A. F. Nagy, Ionospheres of terrestrial planets, Rev. Geophys. Space Phys., 18, 813-852, 1980.

Sica, R. J., M. H. Rees, G. J. Romick, G. Hernandez, and R. G. Roble, Auroral zone thermospheric dynamics, 1, Averages, J. Geophys. Res., 91, 3231-3244, 1986a.

Sica, R. J., G. Hernandez, G. J. Romick, M. H. Rees, and R. G. Roble, Auroral zone thermospheric dynamics, 2, Individual nights, J. Geophys. Res., 91, 13,593-13,611, 1986b.

Sica, R. J., M. H. Rees, R. G. Roble, G. Hernandez, and G. J. Romick, The altitude region sampled by ground-based doppler temperature measurements of the OI 15867 emission line in aurorae, Planet. Space Sci., 34, 483-488, 1986c.

St.-Maurice, J.-P., and W. B. Hanson, A statistical study of F region ion temperatures at high latitudes based on Atmosphere Explorer C data, J. Geophys. Res., 89, 987-996, 1984.

Stolarski, R. S., P. B. Hays, and R. G. Roble, Atmospheric heating by solar EUV radiation, J. Geophys. Res., 80, 2266-2276, 1975.

Volland, H., Magnetospheric electric fields and currents and their influence on large scale thermospheric circulation and composition, J. Atmos. Terr. Phys., 41, 853-866, 1979.

Wickwar, V. B., Global thermospheric studies of neutral dynamics using incoherent-scatter radars, Adv. Space Res., 9, (5)87-(5)102, 1989.

Wickwar, V. B., M. J. Baron, and R. D. Sears, Auroral energy input from energetic electrons and Joule heating at Chatanika, J. Geophys. Res., 80, 4364-4367, 1975.

Yagi, T., and P. L. Dyson, Measurements of thermospheric temperatures at a mid-latitude station, Planet. Space Sci., 33, 203-206, 1985.